Résumé-Abstract

Les études théoriques de $PbTiO_3$ et $SrTiO_3$ sous contraintes mécaniques uniaxiale combinant les calculs de premier principe et la théorie phénoménologique de Landau

Résumé de la thèse

Dans cette thèse, nous présentons des études théoriques de matériaux pérovskites sous contrainte mécanique uniaxiale en combinant les calculs de premier principe DFT ainsi que la théorie phénoménologique de type Landau. Les pérovskites ABO_3 forment une classe très importante de matériaux fonctionnels, qui peuvent présenter un large éventail de propriétés (e.g., supraconductivité, magnétisme, ferroélectricité, multiferroïcité, transitions métal-isolant...) grâce aux petites distorsions d' une même structure prototype cubique. Bien que ces composés aient été largement étudiés expérimentalement et théoriquement, il reste encore des questions importantes et non résolues concernant les effets de contraintes uniaxiales. Au cours de ces dernières années, l' ingénierie de contrainte a été décrite comme une approche originale pour ajuster les propriétés ferroélectriques pérovskites ABO_3. Alors que les effets de tension épitaxié-biaxiale et pression la hydrostatique, sont plutôt bien compris dans cette classe de matériaux, très peu est connu en ce qui concerne l' effet des contraintes mécaniques uniaxiales. Notre étude est motivée par ce manque de compréhension actuelle de l' effet de tension et compression uniaxiale, qui a été jusqu'à présent presque totalement négligé. Deux composés prototypes sont étudiés dans le détail: $PbTiO_3$ et $SrTiO_3$. Après une introduction générale sur les composés ABO_3 et les calculs techniques (ab initio et modèle phénoménologique de Landau), nous avons étudié l' effet de contraintes

mécaniques sur ces matériaux dans notre thèse.

$PbTiO_3$ est un composé ferroélectrique prototypique et également l' un des composants mère de la solution solide $Pb(Zr,Ti)O_3$ (PZT), qui est le piézoélectrique le plus largement utilisé dans des applications. Pour $PbTiO_3$, nous avons montré que indépendamment de la contrainte mécanique uniaxiale appliquée, le système conserve un état fondamental purement ferroélectrique avec la polarisation alignée, soit le long de la direction de la contrainte (en phase FE_z) ou bien le long d' un des axes pseudo-cubique, qui lui est perpendiculaire (phase de FE_x). Cela contraste avec les cas de contraintes mécaniques isotropes ou bi-axial, pour qui de nouvelles phases combinant des modes ferroélectriques et antiferrodistortives ont déjà été décrites. Sous contrainte uniaxiale, $PbTiO_3$ passe d'un état fondamental FE_x sous compression à un état fondamental FE_z en tension au-delà d' une tension critique $\eta_{zz}^c \approx +1\%$. Sous contrainte uniaxiale, $PbTiO_3$ présente soit un état fondamental FE_x sous compression ($\sigma_{zz} < 0$) ou un état fondamental de FE_z sous tension ($\sigma_{zz} > 0$). Cependant, ici, un brusque saut des paramètres structuraux est prévu sous des contraintes de compression et de traction à des valeurs critiques $\sigma_{zz} \approx +2$ GPa et -8 GPa. Ce comportement semble similaire à celui pré-prédit sous pression isotrope négative et pourrait se révéler utile en pratique pour améliorer la réponse piézoélectrique dans les nano-composants.

Le deuxième composé intéressant est $SrTiO_3$. Il a été largement étudié au cours des dernières décennies, en raison de ses propriétés exceptionnelles à basse température. Dans ce travail, nous avons élargi nos précédentes études de $PbTiO_3$, en explorant théoriquement les effets de pression sur la perovskite $SrTiO_3$, combinant les premiers principes de calculs et un modèle phénoménologique de type Landau. Nous avons discuté de l'évolution des fréquences des phonons de $SrTiO_3$ des trois cas de contraintes isotrope, uniaxial et tensions biaxiaux en utilisant les calculs de premier principe. Nous confirmons des travaux expérimentaux précédents sur $SrTiO_3$ que ça soit en contrainte épitaxiée ou sous pression hydrostatique. Enfin, nous avons calculé de diagramme de phase de $SrTiO_3$ sous contrainte uniaxiale, obtenue à partir de la théorie de Landau que nous avons comparé aux calculs de premier principe.

Mots-clés

Oxydes pérovskites, théorie de la fonctionnelle de la Densité, ferroélectricité, contrainte mécanique, théorie de Landau, transitions de phase structurales, mode ferroélectrique, mode antiferrodistortif.

Theoretical studies of $PbTiO_3$ and $SrTiO_3$ under uniaxial mechanical constraints combining first-principles calculations and phenomenological Landau theory

Thesis abstract

In the present thesis we present theoretical studies of perovskite compounds under uniaxial mechanical constraints combining first-principles DFT calculations approach and phenomenological Landau theory. ABO_3 perovskites form a very important class of functional materials that can exhibit a broad range of properties (e.g., superconductivity, magnetism, ferroelectricity, multiferroism, metal-insulator transitions...) within small distortions of the same simple prototype cubic structure. Though these compounds have been extensively studied both experimentally and computationally, there are still unresolved issues regarding the effect of pressure. In recent years, strain engineering has reported to be an original approach to tune the ferroelectric properties of perovskite ABO_3 compounds. While the effect of epitaxial biaxial strain and hydrostatic strain is rather well understood in this class of materials, very little is yet known regarding the effect of uniaxial mechanical constraints. Our study is motivated by the little existing understanding of the effect of uniaxial strain and stress, that has been up to now almost totally neglected. Two prototype compounds are studied in detail: $PbTiO_3$ and $SrTiO_3$. After a general introduction on ABO_3 compounds and calculations techniques (ab initio and phenomenological Landau model), we studied the effect of mechanical constraints in these compounds in our thesis.

$PbTiO_3$ is a prototypical ferroelectric compound and also one of the parent components of the $Pb(Zr,Ti)O_3$ solid solution (PZT), which is the most widely used piezoelectrics. For $PbTiO_3$, we have shown that irrespectively of the uniaxial mechanical constraint applied, the system keeps a purely ferroelectric ground-state, with the polarization aligned either along the constraint direction (FE_z phase) or along one of the pseudocubic axis perpendicular to it (FE_x phase). This contrasts with the case of isotropic or biaxial mechanical constraints for which novel phases combining ferroelectric and antiferrodistortive motions have been previously reported. Under uniaxial strain, $PbTiO_3$ switches from a FE_x ground state under compressive strain to FE_z ground-state under tensile strain, beyond a critical

strain $\eta^c_{zz} \approx +1\%$. Under uniaxial stress, $PbTiO_3$ exhibits either a FE_x ground state under compression ($\sigma_{zz} < 0$) or a FE_z ground state under tension ($\sigma_{zz} > 0$). Here, however, an abrupt jump of the structural parameters is also predicted under both compressive and tensile stresses at critical values $\sigma_{zz} \approx +2$ GPa and -8 GPa. This behavior appears similar to that predicted under negative isotropic pressure and might reveal practically useful to enhance the piezoelectric response in nanodevices.

The second compound of interest is $SrTiO_3$. It has been widely studied in the past decades due to its unusual properties at low temperature. In this work, we have extended our previous investigations on $PbTiO_3$ by exploring theoretically the pressure effects on perovskite $SrTiO_3$ combining the first-principles calculations and a phenomenological Landau model. We have discussed the evolution of phonon frequencies of $SrTiO_3$ with the three isotropic, uniaxial and biaxial strains using first-principles calculations. We also reproduce the previous work done in $SrTiO_3$ with epitaxial strain and hydrostatic strain. Finally, we have calculated the phase diagram of $SrTiO_3$ under uniaxial strain, as obtained from Landau theory and discussed how it compares with the first-principles calculations.

Keywords

Perovskite oxides, Density functional theory, ferroelectricity, strain, stress, Landau theory, structural phase transitions, ferroelectric mode, antiferrodistortive mode.

To my Mommy and Papa for their immense support, care and love

Acknowledgements

My PhD journey was full of colorful and enjoyable experiences. I enjoyed my PhD years. It was the best time I ever had. Looking back on the graduate years in Europe, a lot of wonderful people have made my PhD career a rewarding and unforgettable journey. I want to take this opportunity to thank all the people who have helped me during my PhD thesis.

My supervisors, Prof. Jens Kreisel and Prof. Philippe Ghosez, have been the most influential persons in my academic life. I would like to thank you whole heartedly for accepting me as your PhD student. I am indebted to you for introducing me to research in general and to the field of ferroelectricity in particular. I thank you for your scientific guidance and encouragement. I thank you all for the comprehensive explanations that you gave me and your availability to discuss my results anytime. I would like to thank you for encouraging and funding my travels to different conferences and graduate schools, where I learnt not only science but also had lifetime experiences. You both are excellent supervisors and excellent human beings.

I would also like to thank Dr. Mael Guennou for clearing my doubts during the initial phase of my PhD work. Thanks to Dr. Pierre Bouvier for helping me preparing and performing the diamond anvil cells for the high pressure measurements. Thanks to all the members of LMGP for giving a peaceful and friendly environment during my working period in France.

My first steps in the theoretical field were taken under the guidance of Prof. Ghosez, I would also like to thank you for teaching me all about DFT and allowing me to discuss the calculations openly. A big thanks to Dr. Eric Bousquet, Dr. Safari Amisi and Dr. Momar Diakhate for teaching me the ABINIT software from scratch. Without your help, I could not have made such progress on my thesis. I would also like to thank Dr. Patrick

Hermet and Dr. Daniel Bilc for clearing my doubts on some of my calculations via emails and personal visits. Thank you for your ever-spontaneous replies.

Biggest thanks to Prof. Matthieu Verstraete and Dr. Zeila Zanolli. You were the first ones to make me feel homely during my initial days in Belgium. Thank you also for clearing my doubts on my work and helping me in dealing with various issues other than work. Your support and encouragement were tremendous. I have enjoyed every bit of group dinners together with you all. Thank you for introducing me to Véronique. It was great fun and a lovely experience to be with her, to play, to enjoy and to forget science for some time. I would like to thank Profs. Jean-Yves Raty, John Martin and Stéphane Dorbolo for helping me when I needed. To all the SEGI members especially Dr. David Colignon for helping me to resolve my technical problems while computing. I would also like to thank Dr. Jorge Cors, for supporting my internship in PHASIS, Switzerland. It was a great experience to work in your group.

Thanks Denis for the fruitful collaboration. Thanks to rest of my colleagues: Jinzhu, Hania, Begüm, Alina, Hanen, Naihua, Bin, Nicholas, Julien, Misha, Wilfredo, Baris, Srijan, Theodoros, Marco, Camilo, Gabriel, Can, Sebastian, Alain, Antoine and Brahim. I have enjoyed your pleasant company, discussing science and life.

I would like to thank IDS-Funmat for funding my PhD programme. Thanks to my IDS-Funmat family for making my PhD journey more special. I also thank Dr. Marriane Delmas and all the coordinators for taking care of my work reports each year. My IDS friends, with whom I have enjoyed so much.

Last but not least, to the people I owe the most: Mommy and Papa for your unconditional love and affection. To my grandparents for your blessings. To my sisters Pooja, Deepa and brother Shubham for your support and love. To my brother-in-law Ananta Pandey for showing me the right career path and motivating me to do hard work like you. To my lovely three aunts Sunita, Sushma, Mira for the love you gave to we siblings. To my Manju aunty and Srijana Di for the love and support. Thanks to all my lovely cousins for loving me. I also thank the rest of the members of my family, friends and relatives. To my school teachers, university Professors for your teachings. Many thanks to all my BHU friends for your lasting friendship.

Contents

List of Figures

List of Figures

List of Tables

Abbreviations and symbols

FE	Ferroelectric
PE	Paraelectric
AFD	Antiferrodistortive
AFM	Antiferromagnetic
KDP	Potassium dihydrogen phosphate
FP	First-principles
LGD	Landau-Ginzburg-Devonshire
DFT	Density Functional Theory
DFPT	Density Functional Perturbation Theory
FM	Ferromagnetic
f.u.	Formula unit
LDA	Local Density Approximation
GGA	Generalized Gradient Approximation
GGA-PBE	Generalized Gradient Approximation of Perdew, Burk, and Ernzerhof
WC	Wu Cohen
HF-DFT	Hartree-Fock Density Functional Theory
HK	Hohenberg Kohn
KS	Kohn Sham
PW-PP	Plane-wave pseudopotentials
PTO	Lead titanate
STO	Strontium titanate
CTO	Calcium titanate
BTO	Barium titanate

General Introduction

The central focus of this thesis is exploring the effect of mechanical constraints ferroelectricity in perovskite. A material is said to be ferroelectric when it has a switchable spontaneous electric polarization and the material must have a non-centrosymmetric arrangement of the ions. The discovery of ferroelectricity in the 1920's, led to a surge in development in the modern science and technology. Perovskite functional oxides exhibit a wide variety of physical properties ranging from insulating to superconducting, paraelectric to ferroelectric, multiferroism and non-magnetic to ferromagnetic. This makes perovskite oxide materials an appealing area for scientific research investigation. Applications of ferroelectrics include nonvolatile memory device and piezoelectric applications but also in space, medical science, smart phones applications which find their place in or other modern technology.

The properties of perovskites can be tuned by applying mechanical constraints. Density functional theory (DFT) based electronic structure calculations have been widely used to study and to describe various properties of many condensed matter systems. In this thesis, we apply DFT based ab initio first-principles calculations to study in depth the effect of mechanical constraints in two perovskites: $PbTiO_3$ and $SrTiO_3$. Its numerical implementation is performed by using the ABINIT package [1].

This thesis is divided into five chapters.

Chapter 1 gives a brief introduction to the structure of perovskites and physics of ferroelectricity, its history, discoveries and applications. Different types of structural instabilities are introduced. The literature survey on all the three hydrostatic, biaxial and uniaxial deformations is also discussed.

Chapter 2 gives an overview of Computational details applied in the current thesis and

an brief introduction to Density Functional Theory, The Born-Oppenheimer approximation, ways to solve the Kohn-Sham equations, various approximations to the exchange-correlation functional such as the local density approximation (LDA) and the generalized gradient approximation (GGA) are discussed. The second half of this chapter is devoted to the Landau-Ginzburg-Devonshire theory. We discuss the general introduction of the phenomenological Landau theory, its theoretical basis and technicalities.

In Chapter 3, we focus on the investigation of the ferroelectric $PbTiO_3$. We first discuss the effect of mechanical constraints on $PbTiO_3$ with uniaxial mechanical strains and stresses. Then we present results based on a Landau-Ginzburg-Devonshire (LGD) model which has been developed to study the uniaxial mechanical constraint effect on $PbTiO_3$.

In Chapter 4, we study the mechanical constraint effect on $SrTiO_3$. This material has been of considerable interest due to its low temperature properties. In the first section, we study the effect of uniaxial strain on the FE and AFD instabilities of $SrTiO_3$, which is compared to the case of isotropic and biaxial strains. The phase diagram in terms of uniaxial, biaxial and isotropic amplitude and temperature has been studied by LGD phenomenological theory and compared with the first-principles calculations.

Finally in Chapter 5, we summarize our results and present some future perspectives.

Chapter 1

Introduction

In this chapter, we provide an overview of the main family of compounds (perovskites) which we have studied during this thesis. We also discuss the physical properties that such perovskites exhibits.

1.1 A brief history on ferroelectrics

Ferroelectric materials are at the heart of this PhD thesis. A ferroelectric is an insulating system with two or more discrete stable or metastable states of different nonzero electric polarization in zero applied electric field, referred to as spontaneous polarization. For a system to be considered ferroelectric, it must be possible to switch between these states with an applied electric field, which changes the relative energy of the states through the coupling of the field to the polarization $-E.P$ [2]. Experimentally this was first observed by J. Valasek in Rochelle salt (potassium sodium tartrate) in 1920 [3]. While first was discovered in hydrogen-bonded materials, Rochelle salt and subsequently KDP, but the discovery of ferroelectricity in the much simpler, nonhydrogen-containing perovskite oxide $BaTiO_3$ [4, 5] in 1949 which dramatically changed the physical understanding of this phenomenon. $BaTiO_3$ is the prototypical example of the now extensively studied perovskite oxide family, which includes not only pure perovskite compounds, but also ordered and disordered solid solutions [2]. The relative simplicity of the perovskite structure led to a deeper understanding of the origin of ferroelectricity. Beyond ferroelectricity, perovskite have also shown the

capacity to exhibit a wide range of other properties such as piezoelectricity, pyroelectricity, magnetism, multiferroic, superconductivity etc.

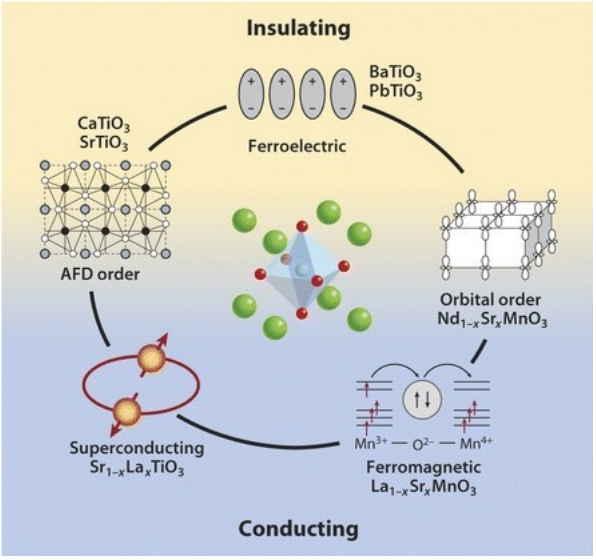

Figure 1.1: Diverse properties of perovskite compounds [6].

Applications include ultra-high density nonvolatile memory devices, capable of retaining data during power loss, and with very short boot-up times. Ferroelectric thin films also play an increasingly important role in other aspects of modern technology. In particular, their piezoelectric, dielectric and pyroelectric properties have been exploited in diverse applications, from accelerometers (airbags), ferroelectric random access memories (FeRAMs), electro-optical devices (thermal imaging), high frequency devices for medical imaging (ultrasonic-based imaging) and surface acoustic wave (SAW) devices (high frequency telecommunication filtering) and many more.

1.2 Perovskite Oxides

The most studied family of ferroelectric oxides are so called perovskite oxides (from the mineral perovskite $CaTiO_3$ named after the Russian mineralogist, L. A. Perovski) which have the general chemical formula ABO_3 [7]. 'A' and 'B' are two cations of very different size, O is an anion that bonds to both 'A' and 'B'. The 'A' cations are usually larger than the 'B' cations. The ideal cubic-symmetry structure has the B cation in a 6-fold BO_6 octahedra coordination and the A cation in a 12-fold AO_{12} cuboctahedral coordination.

The ideal perovskite structure is cubic (space group $Pm\bar{3}m$ (No. 221)), which is the high-symmetry reference structure and is the structure of the high-temperature paraelectric phase. In the idealized cubic unit cell with a basis of 5 atoms, 'A' cations sit at cube corner positions (0, 0, 0), 'B' cation sit at the body centre position (0.5, 0.5, 0.5) and oxygen sit at face centered positions (0.5, 0.5, 0); (0.5, 0, 0.5); (0, 0.5, 0.5) as illustrated in Fig. 1.2.

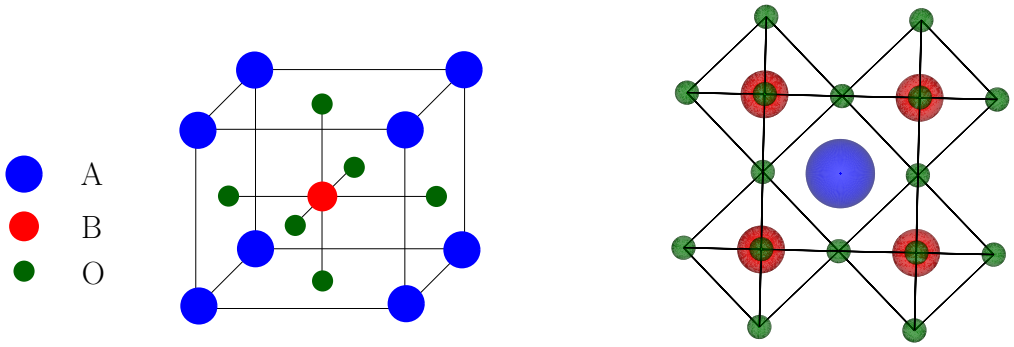

Figure 1.2: Structure of ABO_3. 'A' cations are depicted in dark blue circles, 'B' cation by the red circle in the center of the cell and the 'O' anions by green circles (Left). Ideal cubic perovskite structure, each 'B' cation is bonded to six oxygen atoms, forming an octahedral structure (Right).

An empirical criterion for the stability and distortions of the perfect perovskite-type structure was put forward by Goldschmidt in 1926, which describes the tendency of ABO_3 perovskites to be either ferroelectric or antiferrodistortive [8]

$$\text{Goldschmidt tolerance factor (t)} = \frac{R_A + R_O}{\sqrt{2}(R_B + R_O)}, \tag{1.2.1}$$

where R_A, R_O and R_B are the ionic radii of A, O and B atoms in the ABO_3 perovskite compound. If the tolerance factor t = 1, the A and B site cations are ideally coordinated, and the cubic structure is predicted to be stable; if t > 1 then the compound has tendency to be ferroelectric; if t < 1 then the compound has tendency to be antidistortive which leads to a phase with tilts of the oxygen octahedra. In $BaTiO_3$, for instance, the Ti^{4+} ions are too small for the oxygen octahedra (t > 1) and prefer to move off-center, generating

dipoles that align cooperatively between neighboring unit cells and give rise to ferroelectric order. Replacing Ba with a smaller cation can lead to antiferrodistortive (AFD) ordering, whereby neighboring oxygen octahedra rotate in opposite directions, as is the case for $CaTiO_3$ ($t < 1$) [6].

These two types of distortions are usually but not necessarily exclusive and some perovskite compounds can combine both of them, like $BiFeO_3$ [9].

1.3 Types of Instabilities

Perovskite compounds can exhibit different kinds of structural instabilities (see Fig. 1.3). Most common are Ferroelectric (FE) and Antiferrodistortive (AFD) type of instabilities.

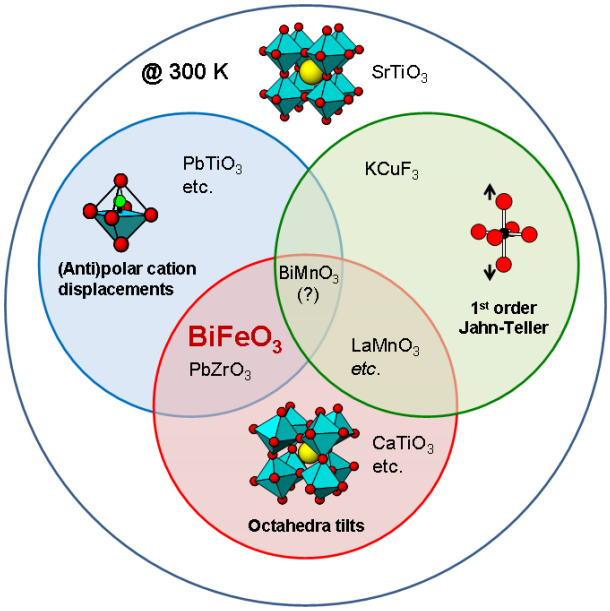

Figure 1.3: Schematic illustration of distortions and their combination in ABO_3 perovskites. (Adapted from Ref. ([10]).

1.3.1 Ferroelectric Instability (FE)

FE instability occurs at the zone center, Γ (0, 0, 0) of the Brillouin zone. Compounds like $BaTiO_3$ and $PbTiO_3$ possess such a FE instability. As an example Fig. 1.4, shows the

pattern of displacements related to the ferroelectric unstable mode in $BaTiO_3$. Phonon calculations show a strong triple degenerated instability at the Γ (0, 0, 0) and which is characterized by vibrations of Ti against the O atoms. This corresponds to the polar unstable mode in this and similar compounds.

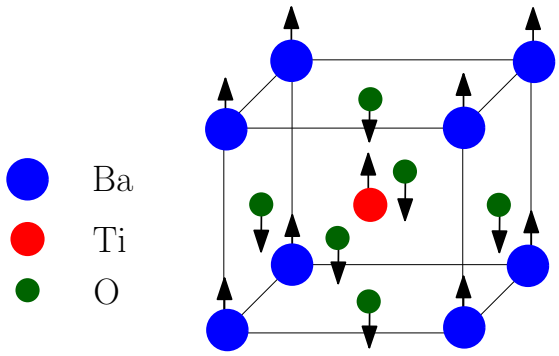

Figure 1.4: Schematic representation of the pattern of displacements related to the ferroelectric $BaTiO_3$.

Contrary to $BaTiO_3$, the FE eigenvector of $PbTiO_3$ is not dominated by the displacement of the Ti against the oxygen along the Ti-O chains, but rather by the Pb moving against the O atoms in the Pb-O planes. As for $BaTiO_3$, unstable Ti-dominated modes are present at X and M points but Pb now plays a dominant role in the character of the unstable modes.

1.3.2 Anti-ferrodistortive Instability (AFD)

AFD instabilities can occur at the zone boundaries, X (0.5, 0, 0), M (0.5, 0.5, 0) and R (0.5, 0.5, 0.5) of the Brillouin zone. Perovskites like $SrTiO_3$, $CaTiO_3$ and $SrZrO_3$ exhibit antiferrodistortive instabilities leading to a rotation/tilting of the BO_6. Fig. 1.5 shows the representation of the oxygen pattern of displacements at low temperature for tetragonal bulk $SrTiO_3$. Octahedra tilting in perovskite structures were classified according to their possible combinations [11, 12] and is the most commonly observed distortion of the cubic $Pm\bar{3}m$ structure. Glazer has proposed the first notation to classify the different octahedral

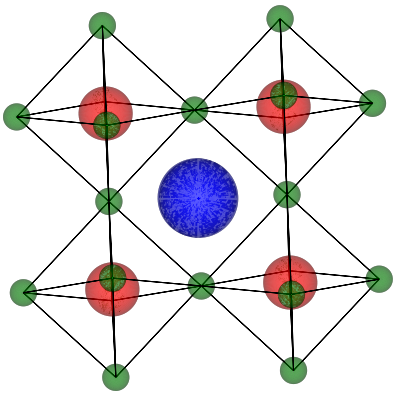

Figure 1.5: Schematic representation of the oxygen pattern of displacements in the low temperature tetragonal bulk $SrTiO_3$, corresponding to the $a^0a^0c^-$ AFD distortions.

tilting patterns [11], which describes the octahedra tilting around each axis as follows: if successive oxygen octahedra rotate in the same direction (in-phase) along one axis, a sign "+" is associated while if successive oxygen octahedra rotate in opposite direction (out-of-phase), the sign "-" is reported. If no rotation takes place, then the sign "0" is reported. For the three directions in space, a letter is associated, "a", "b" or "c", depending on the relative amplitude of rotation about respectively the x, y or z directions. So, if we suppose in-phase tilts of successive oxygen octahedra around the z-axis, the following Glazer notation applies: $a^0a^0c^+$. If successive oxygen octahedra rotate in phase opposition, we then have $a^0a^0c^-$. The M point AFD instabilities correspond to $a^0a^0c^+$ while the R point AFD instabilities correspond for instance to $a^0a^0c^-$. With these notations, the low temperature structure of bulk $SrTiO_3$ corresponds to $a^0a^0c^-$ [13]. There are 23 different rotation patterns or tilt patterns which lead to 15 space groups as shown in Fig. 1.6.

There is a strong competition between FE and AFD instabilities in their bulk cubic structure and they are generally exclusive, notable exceptions include $BiFeO_3$ [9]. The freezing of the related eigendisplacements allows to decrease the energy and brings the system in to its ground-state. The calculation of the unstable modes in the harmonic approximation allows to determine the curvature of the energy at the origin for a given pattern of displacement. However, to determine the exact ground-state, atomic relaxations should be performed by freezing-in the eigendisplacements of the unstable modes in order to properly

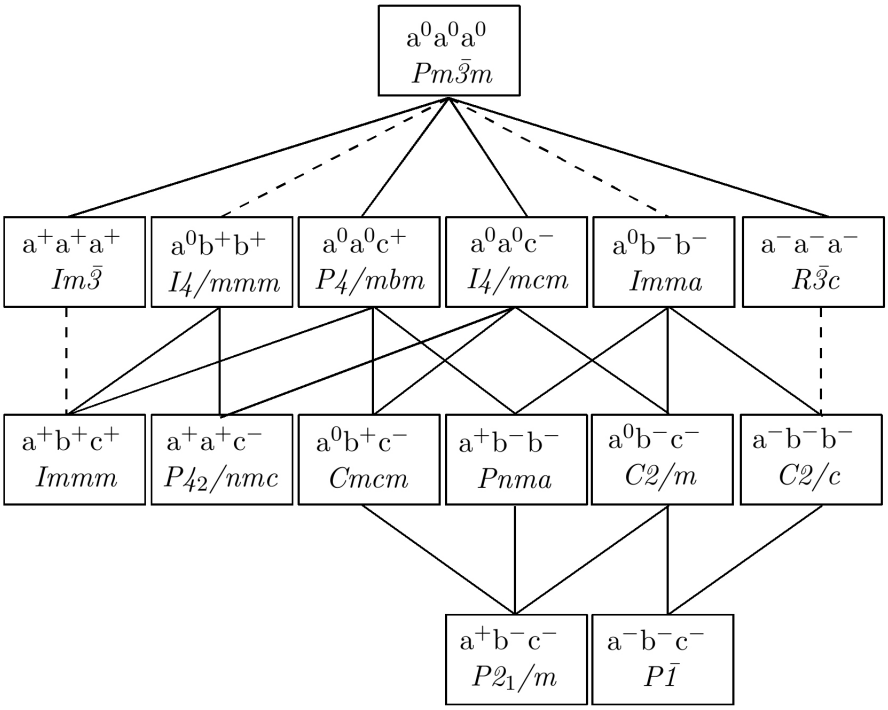

Figure 1.6: Schematic diagram indicating the group-subgroup relationship between the 15 possible configurations of AFD tilts. A dashed line indicates that the corresponding phase transition requires by Landau theory to be first order [14].

include anharmonic effects.

1.3.3 Ferroelectricity: A key concept

Ferroelectricity is a property of certain materials which possess a spontaneous electric polarization that can be reversed by the application of an external electric field [15, 16]. Ferroelectricity is allowed only in materials which are non-centrosymmetric. For ferroelectric materials the spontaneous polarization usually occurs only in a certain temperature range and in most of the case ferroelectric crystals undergo a phase transition at high temperature towards a cubic structure, loosing their spontaneous polarization at a Transition temperature (T_c) or the Curie point. Compounds are ferroelectric when $T < T_c$ and become paraelectric when $T > T_c$. A main signature of this ferroelectric materials is a temperature dependent maximum in the dielectric constant [17], as shown in Fig. 1.7.

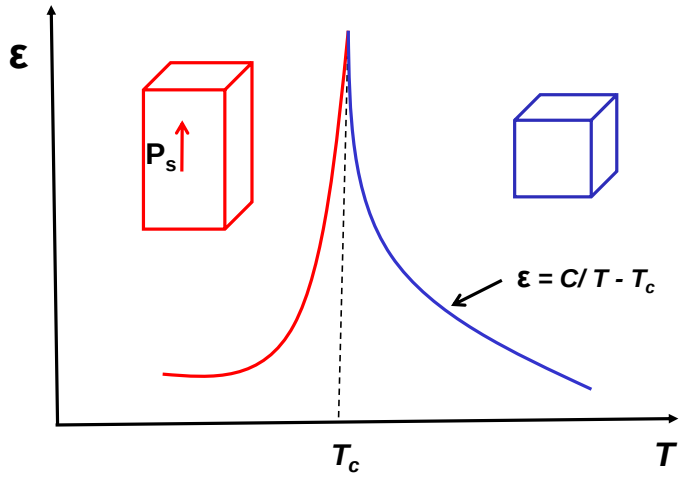

Figure 1.7: Structural phase transition from a paraelectric phase (blue) to a ferroelectric phase (red). ε is the dielectric constant, T_c is the critical temperature, T is the temperature of the material and C is the Curie constant.

Another characteristics of ferroelectric substance is the occurrence of a domain structure and the related hysteresis. In each domain of such a substance, the molecular dipoles have the same orientation, but this orientation is different for different domains and can

be influenced by an external electrical field. A ferroelectric domain is defined as a region within which the direction of the spontaneous polarization is constant and the region which separates the two domains is called the domain wall. In ferroelectric materials, the polarization P does not vary linearly with electric field E but shows a so-called hysteresis curve. A typical hysteresis curve is shown in Fig. 1.8, where the influence of an external electrical field causes the rearrangement of domains in a ferroelectric material.

- When an electric field is applied to an unpoled sample, the domains having a polarization parallel to the external field increase on the account of those domains having a different polarization, thus the polarization increase and the dependence $P = P(E)$ is shown by the green dotted lines in the Fig. 1.8.

- When all the domains become oriented parallel to the external electric field, then the polarization reaches a saturation level P_s, as we have reached a single domain state. The value of the spontaneous polarization is obtained by the extrapolation of the linear part as denoted by red dotted lines. The value of P_s that was obtained is similar to the polarization that existed in each domain in the initial state corresponding to the origin denoted by blue solid circle.

- When the intensity of the electrical field decreases the polarization also decreases. If the field intensity becomes zero, there is still a remanent polarization (P_r) in the crystal which is represented by yellow and red dots. In order to destroy this remanant polarization, the crystal must be polarized in the opposite direction by applying an opposite electric field. This electric field, which is needed to counteract the polarization, is called the coercive field (-E_c) and it is represented by pink dot.

- Afterwards, the polarization of the substance sample changes its sense according to the orientation of the domains corresponding to the new direction of the electrical field; it eventually reaches its maximum value -P_s, represented by the green dot in Fig. 1.8. Again, the subsequent variation of the electrical field towards positive values generate a dependence $P = P(E)$ similar to that already described previously following the green-yellow-purple-black dots.

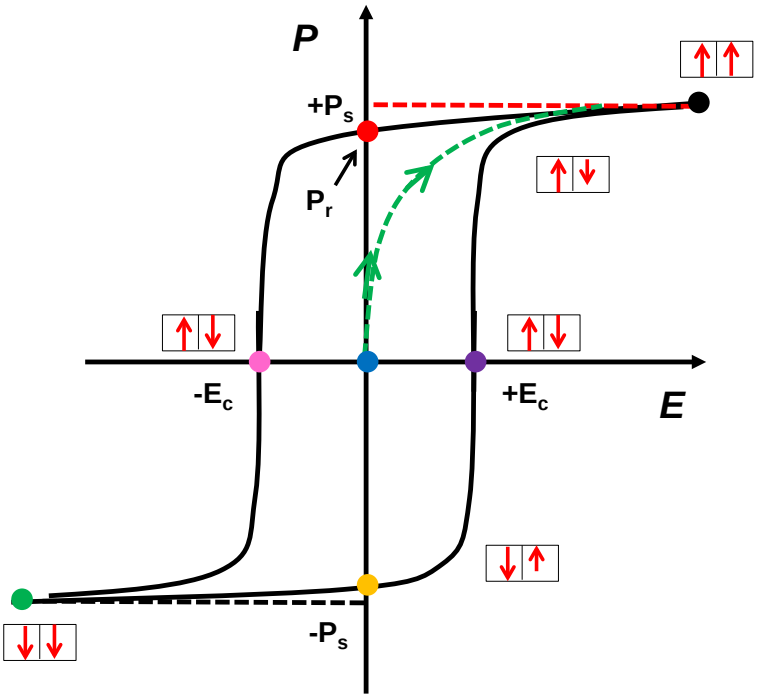

Figure 1.8: Schematic representation of ferroelectric hysteresis loop. Domains are indicated in red arrows.

1.3.4 Electric Polarization

The Electric Polarization can be measured experimentally as well as from calculations. Experimentally the polarization is determined measuring the electric current going through a ferroelectric capacitor when the polarization is switched. The magnitude of spontaneous polarization can also be estimated theoretically by using the expression as,

$$P = \frac{e}{\Omega} \sum Z^* \xi, \tag{1.3.1}$$

where Ω is the cell volume, 'e' is the absolute value of the electron charge, Z^* is the Born effective charges, ξ is the distortion from a reference centrosymmetric structure to the ferroelectric phase and the summation is over the number of atoms. We take the Born effective charges (Z^*) for each atom to have their values in the cubic structure. In ferroelectrics, the absolute polarizations of ferroelectric structures are generally determined from the change in polarization, relative to the related centrosymmetric reference structure, e.g., an ideal centrosymmetric perovskite structure with polarization equal to zero [18]. The polarization can also be more accurately determined using the Berry phase formalism

[19, 20]. The Born effective charges (Z^*) which induced the polarization by the atomic displacements, plays a vital role in understanding the polar ground state and the lattice dynamics. The Born effective charges are tensors, defined as the first derivative of the polarization with the atomic displacement under the condition of zero macroscopic electric field. High values of these dynamical charges would lead to large spontaneous polarization, even for small distortions.

1.3.5 Phonons and Lattice Instabilities

One of the most important early advances in the understanding of ferroelectricity was the development of the soft-mode theory of ferroelectrics, which identified an intimate link of the lattice dynamics [21, 22] and the microscopic origin of ferroelectricity. It has been proposed that the paraelectric to ferroelectric phase transition is due to a softening polar transverse optical (TO) mode that freezes-in below the transition temperature (T_c), giving rise to a dipolar moment in each unit cell. The signature of this behavior in a ground-state first-principles calculation is an unstable polar phonon in the high-symmetry reference structure [23, 24].

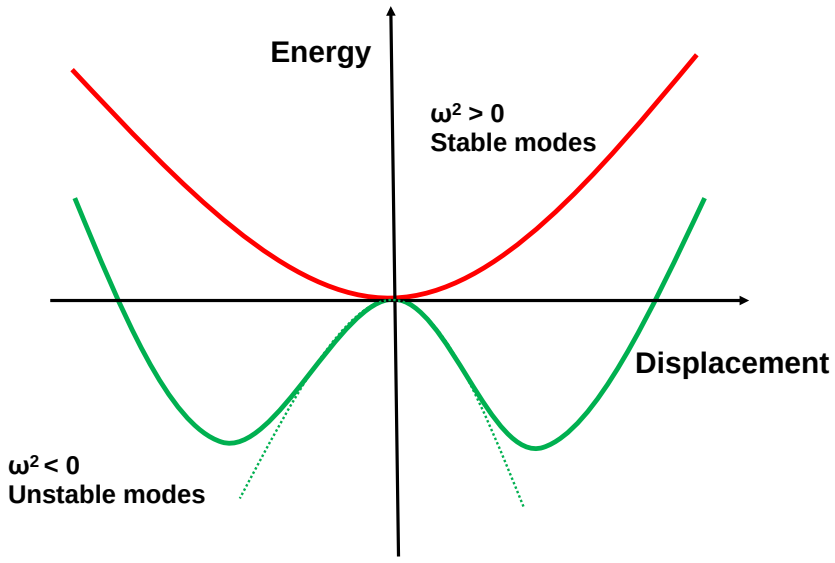

Figure 1.9: Schematic illustration of phonon instabilities.

When the atomic displacement pattern of the unstable mode is frozen, a double-well struc-

ture is obtained in the energy as the function of the displacement as shown in Fig. 1.9. The unstable phonons modes are present in the cubic paraelectric structure as shown by the green curve and when this modes are frozen below the transition temperature (T_c), it gives rise to a stable phonon modes as shown by the red curve. When the structure is stable, all atomic positions are, such as the energy, at the minimum and the displacements are positive. This gives rise to positive phonon modes or real frequencies with $\omega^2 > 0$. This is referred as the ground state structure. When the structure is unstable, atomic distortions allow to decrease the energy. The energy curvature at the origin becomes negative with $\omega^2 < 0$, and gives rise to the negative phonon modes or imaginary frequency. This structure is different from the ground state structure. Therefore, the computation of phonons in the paraelectric high symmetry phase and the onset of imaginary frequency is a way to identify the crystal structural instabilities. Cohen [23], also demonstrated for model $ATiO_3$ ferroelectrics that a hybridization between oxygen $2p$ states and the surrounding cations stabilizes FE. For instance, in $BaTiO_3$ the hybridization between the $3d$ orbitals and the O $2p$ orbitals lead to ferroelectricity, while in $PbTiO_3$ a hybridization between O $2p$ and Pb 6 p-levels are important.

1.4 Effect of deformations on perovskites

Strain engineering refers to a general strategy employed in any materials to enhance its performance with a wide variety of properties. New and unexpected properties have been observed for material subjected to mechanical constraints. Due to the polarization-strain coupling in ferroelectric materials, ferroelectricity is highly sensitive to mechanical constraints as strains and stresses, that can be used in practice to tune phase transition temperatures and multifunctional properties [16]. The effect of high pressure on ferroelectrics and Strain-engineering in ferroelectric oxide thin films have attracted a lot of interest in solid state physics but the underlying mechanism are still not fully understood. Past studies have shown that theoretical findings can provide a guide in what type of materials we can expect larger polarizations and larger coupling effects to discover novel materials for technological applications.

1.4.1 Hydrostatic pressure

Although the parameter high-pressure is a fundamental parameter for the understanding of matter, its effects have been much less studied in comparison with the parameter temperature. This is essentially due to the initial experimental difficulties in applying high-pressure. Historically, the parameter high-pressure has a large importance in the field of mineralogy, petrology or in the planetary physics where the pressure is directly related to the depth of the planets. In fact, most of the high-pressure studies on oxides have been conducted by researchers coming from the latter fields. However, over the past years, the interest of high-pressure for the understanding of functional materials has been increasingly recognized and has led to a large number of investigations, namely on functional perovskites.

G. A. Samara has described pressure as a "clean parameter" by stating that pressure mainly acts on interatomic distances. This is indeed a considerable advantage with respect to the parameter temperature which results in thermal vibrations, a fact that often complicates a straightforward analysis of experimental results. Furthermore an isothermal compression (when compared to the effect of temperature) leads to large changes in cell volume since it acts directly on interatomic distances. To illustrate this point, let us compare the effect of thermal expansion to compression for the perovskite $KNbO_3$:

$$\frac{\Delta V(5 \rightarrow 700K)}{V(5K)} = 1\%, \quad \text{while} \quad \frac{\Delta V(1bar \rightarrow 100GPa)}{V(1bar)} = 24\%.$$

It thus becomes clear that high-pressure leads to important relative changes in volume, allowing testing structural instabilities and leading for most solids to profound changes in its physical parameters. General rules for predicting phase transitions in perovskites have been of long-standing interest. As a fruit of past studies it is now generally accepted that increasing temperature reduces both tilt instabilities (the tilt angle decreases with increasing temperature) and polar instabilities (decrease of the polar cation displacement) [25–28].

The effect of high pressure on perovskites is more complex. Previously it was suggested by Samara *et.al*, [29] that the phase transition temperature, T_c of zone-boundary transitions in perovskites increase with pressure, i.e., the antiferrodistortive tilt angle increases with increasing pressure. However, later on it was shown by the experiments on $LaAlO_3$ [30]

and on some other perovskites revealed that some of these perovskites decrease their tilt angle and undergo phase transitions to higher-symmetry phases on increasing pressure [31–34]. Later on Angel *et al.* [32], provided a new general rule which predicts the behavior of octahedra tilts by taking into account the compressibilities of the different polyhedra. Concerning polar instabilities Samara *et al.* [29], described in his pioneer work that pressure reduces ferroelectricity in ABO_3 perovskites and even annihilates it for a critical pressure P_c at which the crystal structure becomes cubic. Early experimental investigations on $BaTiO_3$ [35, 36], $KNbO_3$ [37, 38], $PbTiO_3$ [39, 40] confirmed this view and let to the widely accepted conclusion that polar perovskites adopt for $P > P_c$ a cubic $Pm\bar{3}m$ crystal structure. Unexpectedly, a re-investigation of $PbTiO_3$ (PTO) by Kornev *et al.* has shown that this perovskite recovers ferroelectricity as pressure increases above a critical value [41]; similar predictions have been made for $BaTiO_3$ [42]. Another interesting result concerns the pressure-induced anomalous phase transitions, tetragonal-to-monoclinic-to-rhombohedral-to-cubic and its role in a potential colossal enhancement of piezoelectricity in $PbTiO_3$ [43].

1.4.2 Biaxial strain

Ferroelectric thin films can show tremendously different behavior than bulk and has proved a powerful way for tuning physical properties in ferroelectrics. Strains can be imparted into thin films through differences in lattice parameters and thermal expansion behavior between the film and the underlying substrate or they can arise from defects formed during film deposition [44–47]. Strain engineering in ferroelectrics has allowed the discovery of a significant enhancement of the polarization and the transition temperature [48] and the discovery of room-temperature ferroelectricity in strained $SrTiO_3$ [49]. Biaxial strain engineering have also been studied theoretically using Landau theory and first-principles derived results on $SrTiO_3$ [50, 51] and $CaTiO_3$ [52, 53]. The discovery of novel materials by artificially grown layered ferroelectric superlattices is also an exciting area of research and takes the potential of strain engineering to next level. For instance the work on BTO/STO superlattice [54], PTO/STO superlattice [55] and the development of polar interfaces between two perovskite band insulators, $LaAlO_3$ and $SrTiO_3$ shows the progress in this area of strain engineering [56].

1.4.3 Uniaxial pressure

Compared to the effect of hydrostatic and biaxial deformations, the case of uniaxial pressures has been much less explored, namely due to experimental difficulties [57–59]. Uniaxial stress on ferroelectricity in $PbTiO_3$ and $BaTiO_3$ films was also studied theoretically [60]. Recently, there have been work done under uniaxial stress on $PbTiO_3$ [61]. Despite this, more work is needed for profound understanding of the effect of uniaxial pressure on perovkites.

Chapter 1: Introduction

Chapter 2

Theoretical Approach: Methods and Models

The aim of this chapter is to provide a brief description of the theoretical framework which we have used to perform the calculations and analyze the results of the current thesis. In the first section, we describe the main concepts of the first-principles calculations based on the Density functional theory (DFT) and in the subsequent section, we describe the Phenomenological Model based on the Landau theory. We have used these techniques to study the properties of mechanically constrained perovskite compounds in our thesis. In this context we describe the general problem, Density functional theory, Born-Oppenheimer approximation and LGD theory without going into much mathematical details.

2.1 First-principles calculations

2.1.1 Introduction

Density functional theory (DFT) has been very popular for calculations in solid-state physics since the 1970's. Density functional theory (DFT) is a quantum mechanical modelling method used in physics and chemistry to investigate the electronic structure (principally the ground state) of many-body systems, in particular atoms, molecules, and the condensed phases. Density Functional Theory (DFT) is one of the most widely used meth-

ods for "ab initio" calculations of the structure of atoms, molecules, crystals, surfaces, and their interactions [62]. Our calculations are performed in the framework of first-principles calculations based on the Density functional theory so, in this section we give the general framework, equations and the main approximations we used in our calculations.

2.1.2 General Many-body problem

A solid can be considered as a system of nuclei and electrons interacting with each other. In solid state physics, the starting point is the Hamiltonian for a system of interacting electrons and nuclei:

$$H(\boldsymbol{R},\boldsymbol{r}) = T_N(\boldsymbol{R}) + T_e(\boldsymbol{r}) + V_{NN}(\boldsymbol{R}) + V_{ee}(\boldsymbol{r}) + V_{eN}(\boldsymbol{R},\boldsymbol{r}), \tag{2.1.1}$$

where

Kinetic energy of the nuclei:

$$T_N = -\frac{\hbar^2}{2}\sum_I \frac{1}{M_I}\frac{\partial^2}{\partial \boldsymbol{R}_I^2} \tag{2.1.2}$$

Kinetic energy of the electrons:

$$T_e = -\frac{\hbar^2}{2m}\sum_i \frac{\partial^2}{\partial \boldsymbol{r}_i^2} \tag{2.1.3}$$

Interaction between the nuclei:

$$V_{NN} = \frac{e^2}{2}\sum_{I\neq J} \frac{Z_I Z_{II}}{\|\boldsymbol{R}_I - \boldsymbol{R}_J\|} \tag{2.1.4}$$

Interaction between the electrons:

$$V_{ee} = \frac{e^2}{2}\sum_{i\neq j} \frac{1}{\|\boldsymbol{r}_i - \boldsymbol{r}_j\|} \tag{2.1.5}$$

Interaction between the electrons and nuclei:

$$V_{eN} = -e^2\sum_{iI} \frac{Z_I}{\|\boldsymbol{r}_i - \boldsymbol{R}_J\|}, \tag{2.1.6}$$

where Z_I is the charge of the ion I with mass M_I, m and $-$e is the mass and elementary charge of the electron, R$\equiv R_I$ and r $\equiv r_i$ is the set of all nuclei R_I and electronic r_i coordinates.

In the time-independent quantum mechanics, the physics of a system of interacting particles is described by the following Schrödinger equation:

$$H\Psi = E\Psi, \tag{2.1.7}$$

where H is the Hamiltonian of the system, Ψ is the wave function for all the particles ("many-body" wave functions) and E is the energy. Since it is not possible to solve the Schrödinger equation for a many-body problem exactly, we have to use some approximations.

The Born-Oppenheimer approximation is based on the observations that $M_I >> m$. So, the kinetic energy of the nuclei T_N can be neglected in Eq. (2.1.1). If $T_N \simeq 0$, there is no any differential operator acting on the positions of the nuclei, so that it becomes a parameter of the Hamiltonian. Since the mass of the nuclei is much larger than the mass of the electrons, they are much slower and the electrons adiabatically adopt to nuclei positions. The Hamiltonian in Eq. (2.1.1) simplifies to,

$$H_e(\boldsymbol{R}, \boldsymbol{r}) = T_e(\boldsymbol{r}) + V_{NN}(\boldsymbol{R}) + V_{ee}(\boldsymbol{r}) + V_{eN}(\boldsymbol{R}, \boldsymbol{r}). \tag{2.1.8}$$

Thus the electronic Hamiltonian includes the kinetic energy operator of the electrons T_e, plus the interaction energy operator V_{ee} and the potential energy operator due to the interaction of the nuclei on the electrons V_{eN}. The term V_{NN}, is the classical interaction of nuclei that can be trivially obtained. By using the Born-Oppenheimer approximation, the description of the interacting electrons of N ions in a macroscopic solid reduces to

$$H_e\Psi_e = E_e\Psi_e. \tag{2.1.9}$$

Still there are about 10^{23} electrons in the material so that it remains, in practice, impossible to solve the Schrödinger equations and further simplifications are required, in order to solve the problem.

2.2 Density functional theory

Density Functional Theory (DFT) is a theory of correlated many-body systems, built in the 60's by Hohenberg and Kohn [64] and Kohn and Sham [65] who provided a method

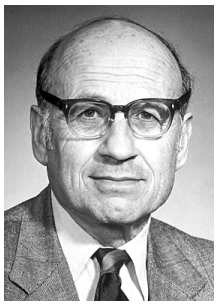

Figure 2.1: Walter Kohn was awarded a Nobel prize in 1988 for his development of the Density functional theory (Adapted from Ref. [63]).

for estimating the many-body electron-electron interactions. So, DFT is based on two core advances reported by Hohenberg and Kohn and then by Kohn and Sham. The main idea of DFT is to describe a many-body interacting system with its particle density and not with many-body wavefunction. The remarkable success of the approximate local density (LDA) and generalized gradient approximation (GGA) functionals within the Kohn-Sham approach have led to widespread interest in the density functional theory as the most promising approach for accurate, practical methods in the theory of materials [66].

2.2.1 Hohenberg and Kohn formalism

The ground state particle density $n(\boldsymbol{r})$ of a system of interacting particles in an external potential V_{ext} uniquely determines the external potential $V_{ext}(\boldsymbol{r})$, except for a constant to any system of interacting particles. This is the first Hohenberg and Kohn formalism. In other words it states that, the ground state properties of a many-electron system are uniquely determined by an electron density that depends on only 3 spatial coordinates. It lays the base for reducing the many-body problem of N electrons with $3N$ spatial coordinates to 3 spatial coordinates, through the use of functionals of the electron density.

The second Hohenberg and Kohn formalism defines an energy functional for the system and proves that the correct ground state electron density minimizes this energy functional so the properties of the system are determined by their ground state density, $n(\boldsymbol{r})$. In this theory the energy of the system, $E[n(\boldsymbol{r})]$, is expressed as a unique functional of this electron density, $n(\boldsymbol{r})$,

$$E[n(\boldsymbol{r})] = \int V_{ext}\ (\boldsymbol{r}) n(\boldsymbol{r}) d^3\boldsymbol{r} + F[n(\boldsymbol{r})], \tag{2.2.1}$$

where V_{ext} is an external electrostatic potential due to the nuclei and $F[n(\boldsymbol{r})]$ is a unique functional of the electron density $n(\boldsymbol{r})$. The visualization of Hohenberg-Kohn formalism is shown in Fig. 2.2. Although Hohenberg and Kohn formalism consider particle density $n(\boldsymbol{r})$ as the basic variable, it is still impossible to calculate any property of a system because the universal functional $F[n(\boldsymbol{r})]$ is unknown. This difficulty was overcome by Kohn and Sham in 1965, who proposed the Kohn-Sham ansatz [65].

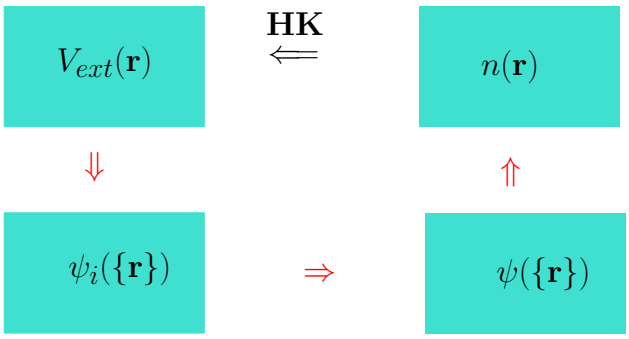

Figure 2.2: Visualization of Hohenberg-Kohn formalism. The red arrows denote the usual solution of Schrödinger equation where the $V_{ext}(\boldsymbol{r})$ determines all the $\psi_i(\{\mathbf{r}\})$, $\psi(\{\mathbf{r}\})$ and $n(\boldsymbol{r})$. The black arrow (HK) denotes Hohenberg and Kohn formalism (Adapted from Ref. [66]).

2.2.2 The Kohn-Sham (KS) Ansatz

Kohn and Sham proposed a convenient technique to reformulate HK formalism, therefore DFT became the most popular tool for electronic structure calculations. KS approach has proven to be one of the most efficient and reliable first-principles methods. The KS ansatz was so successful that Kohn was honored the Nobel prize in chemistry. The Kohn-Sham ansatz assumes that the ground state density of the original interacting system is equal to that of some chosen non-interacting system. Kohn and Sham subsequently approximated the unknown form, $F[n(\boldsymbol{r})]$ in Eq. 2.2.1 as follows:

$$F[n(\boldsymbol{r})] = T_0[n(\boldsymbol{r})] + E_H[n(\boldsymbol{r})] + E_{xc}[n(\boldsymbol{r})], \tag{2.2.2}$$

where $T_0[n(\boldsymbol{r})]$, is the kinetic energy of a system of non-interacting particles with density $n(\boldsymbol{r})$, $E_H[n(\boldsymbol{r})$ is the classic electrostatic (Hartree) energy of the electrons, and $E_{xc}[n(\boldsymbol{r})]$ is

the exchange-correlation energy which not only includes exchange and correlation energies but also the difference between $T_0[n(\boldsymbol{r})]$ and the true kinetic energy of the interacting system, however its exact form is still not known so in addition Kohn and Sham expressed the electron density as,

$$n(\mathbf{r}) = \sum_{i=1}^{N} |\psi_i(\mathbf{r})|^2. \tag{2.2.3}$$

The Eq. 2.2.3 denotes the electron density as a sum over N single particle. The terms in Eq. 2.2.2 is expressed as,

$$T_0\left[n(\mathbf{r})\right] = -\sum_{i=1}^{N} \frac{\hbar^2}{2m} \int \psi_i^*(\boldsymbol{r}) \nabla^2 \psi_i(\boldsymbol{r}) d^3\boldsymbol{r} \tag{2.2.4}$$

$$E_H[n(\boldsymbol{r})] = \frac{e^2}{2} \int \frac{n(\boldsymbol{r}) n(\boldsymbol{r'})}{|\boldsymbol{r} - \boldsymbol{r'}|} d^3\boldsymbol{r} d^3\boldsymbol{r'} \tag{2.2.5}$$

$$E_{xc}^{DFT}[n(\boldsymbol{r})] = \int \epsilon_{xc}(\boldsymbol{r}) n(\boldsymbol{r}) d\boldsymbol{r} \tag{2.2.6}$$

In Eq. 2.2.6, $E_{xc}^{DFT}[n(\boldsymbol{r})]$ is the exchange correlation energy also described in [65] and ϵ_{xc} is the exchange-correlation energy of a homogeneous electron gas. This can be approximated in DFT by using the two approaches local density approximation (LDA) and generalized gradient approximation (GGA). The details have been described in the following section.

The Kohn-Sham wave equation, obtained from a variational minimization of Eq. 2.2.1, subject to the constraint of particle number conservation, is expressed as,

$$\left[-\frac{\hbar^2}{2m} \bigtriangledown^2 + V_{eff}(\boldsymbol{r})\right] \psi_i(\boldsymbol{r}) = \varepsilon_i \psi_i(\boldsymbol{r}), \tag{2.2.7}$$

where ε_i are the single particle eigenvalues, and V_{eff} is the effective potential which can be expressed as

$$V_{eff}(\mathbf{r}) = V_H(\mathbf{r}) + V_{\text{ext}}(\mathbf{r}) + V_{xc} \tag{2.2.8}$$

$$V_H = \frac{\delta E_H}{\delta n(\boldsymbol{r})} \tag{2.2.9}$$

$$V_{xc} = \frac{\delta E_{xc}}{\delta n(\boldsymbol{r})} \tag{2.2.10}$$

where $V_{ext}(\boldsymbol{r})$ is the external potential due to the nuclei, $V_H(\mathbf{r})$ and V_{xc} are the Hartree and exchange correlation potentials in Eq. 2.2.9 and 2.2.10. The result of the Kohn-Sham approach is to transform the problem of N interacting electrons to solving N independent Schrödinger equations for non-interacting electrons moving in an effective potential (with all the sum of the Hartree, external and exchange correlation potentials). Eq. 2.2.7, is the Kohn-Sham equation which is a nonlinear differential equation and it must be solved self-consistently. From the above one calculates a new density and starts again. The resulting new electron density $n(\boldsymbol{r'})$ is compared with the previous density $n(\boldsymbol{r})$ and if differences exists between them, then the Kohn-Sham equations are again solved by starting with a new density which is a mix of $n(\boldsymbol{r})$ and $n(\boldsymbol{r'})$ densities. This procedure is then repeated until convergence is reached [i.e., $n(\boldsymbol{r}) = n(\boldsymbol{r'})$]. Hence, Kohn and Sham have shown that the many-body interactions and single-body interaction can have the same electronic ground state applying the condition that the particles of the non-interacting system move in an effective potential $V_{eff}(\boldsymbol{r})$. This is also known as Kohn-Sham potential V_{KS}. The visualization of Kohn-Sham ansatz is shown in Fig. 2.3.

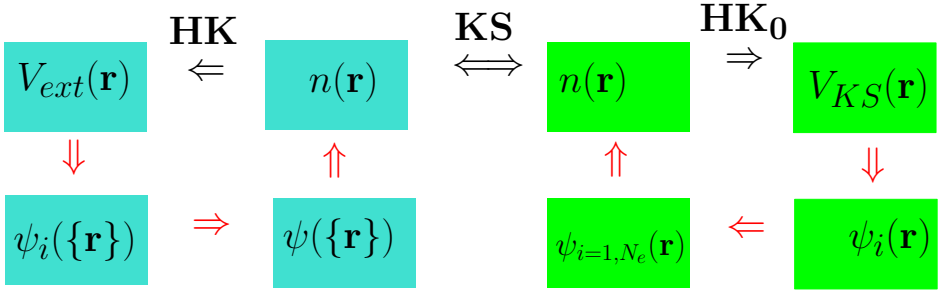

Figure 2.3: Visualization of Kohn-Sham ansatz. The notation HK_0 denotes the HK formalism applied for non-interacting system and the black arrow labelled KS shows the connection in both directions of many-body interacting system to non-interacting system. Thus, Kohn and Sham ansatz determines all the properties of the many-body systems (Adapted from Ref. [66]).

2.3 Practical considerations for DFT implementation

DFT provides us the possibility to access different physical quantities from first-principles in an accurate way even though we have to consider some approximations to simplify and solve the Kohn-Sham equations while keeping the accuracy and reducing computation cost.

2.3.1 Exchange-correlation functionals

Although Kohn and Sham demonstrated the existence of a universal density functional, in practice the calculations rely on approximations of E_{xc}. The major problem with DFT is that the exact functionals for exchange and correlation are not known except for the free electron gas. The most widely used approximation is the local-density approximation (LDA), where the functional depends only on the density at the coordinate where the functional is evaluated. This exchange-correlation energy is assumed to be the same than the homogeneous electron gas with that density:

$$E_{xc}^{LDA}[n] = \int \epsilon_{xc}^{\text{hom}}[n\ (\boldsymbol{r})]n(\boldsymbol{r})d\boldsymbol{r} \tag{2.3.1}$$

The exchange part of the homogeneous gas can be obtained from Hartree-Fock method, which gives a simple analytic form:

$$\epsilon_{x}^{\text{hom}}[n] = -\frac{3}{4\pi}(3\pi^2 n)^{1/3}. \tag{2.3.2}$$

The correlation part $\epsilon_{c}^{\text{hom}}$ [n] was calculated with Monte-Carlo simulation of the homogeneous electron gas [67]. There are various formulations (Wigner, Perdew-Zunger, Perdew-Wang, Teter etc.) that are referred to as local density approximations. Even if the LDA approximation is strong, it works remarkably well in many cases, which makes this approximation the most widely used in solid state simulations [68]. The typical errors of LDA approximation with respect to the experimental data, are within 1% on atomic positions and lattice constants and within 5% on the phonon frequencies. The exception is on the estimation of the band-gap which is systematically underestimated (often by 40-50%) with respect to the experiments. Although small in comparison even 1% error on the lattice constants can have direct consequences in perovskite compounds, where the ferroelectric

instability is very sensitive even to the smaller strains.

$$E_{xc}^{GGA}\left[n(\boldsymbol{r})\right] = \int \epsilon_{xc}\left[n(\boldsymbol{r}), |\nabla n(\boldsymbol{r})|\right] n(\boldsymbol{r}) d\boldsymbol{r}. \tag{2.3.3}$$

The alternative available approximations such as Generalized Gradient Approximation (GGA) [69, 70] or GGA-WC (Wu-Cohen) where the exchange-correlation functional depends not only on the local density at $\boldsymbol{r}$, but also on its gradient or higher order derivatives (see Eq. 2.3.3); the weighted density approximation (WDA) [71] or the so-called hybrid functionals were also developed to improve the accuracy beyond the LDA and avoid its deficiencies. We have reported all our calculations using LDA and GGA-WC functionals in this thesis.

2.3.2 Plane-wave basis set

For an infinite solid with the Born-Von Karman periodic boundary conditions, the wave function can be written in the Bloch form as a product between a plane wave and a lattice periodic function $\mathrm{u}_n(\boldsymbol{k}, \boldsymbol{r})$:

$$\psi_{n,\boldsymbol{k}}(\boldsymbol{r}) = \frac{1}{\sqrt{\Omega}} u_n(\boldsymbol{k}, \boldsymbol{r}) e^{i\boldsymbol{k}\cdot\boldsymbol{r}}, \tag{2.3.4}$$

where Ω is the volume of the cell, $\boldsymbol{k}$ a wave-vector of the reciprocal space and n the energy band index

$$\psi_{n,\boldsymbol{k}}(\boldsymbol{r}) = \frac{1}{\sqrt{\Omega}} \sum_{G} C_{n,\boldsymbol{k}}(\boldsymbol{G}) e^{i(\boldsymbol{k}+\boldsymbol{G})\cdot\boldsymbol{r}}. \tag{2.3.5}$$

In practical calculations, Bloch functions are expanded in a Fourier expansions as shown in 2.3.5, and the Fourier transformation of the Bloch functions involves infinite number of plane wave terms. In practice, the plane wave expansion is truncated to plane waves with kinetic energy lower than a cut-off energy E_{cut} such as:

$$\frac{\hbar^2}{2m} |\boldsymbol{k} + \boldsymbol{G}|^2 \leq E_{cut}, \tag{2.3.6}$$

where $\boldsymbol{G}$ is the a vector of the reciprocal space. This kind of truncation introduces an error that can be controlled by increasing the value of E_{cut}, so a convergence procedure is needed in practical calculations.

2.3.3 The pseudopotential approximation

The pseudopotential approximation is based on the observation that the core electrons are relatively unaffected by the chemical environment of an atom, so the behavior of the core electrons may be approximated. Since the wave functions of these particular electrons evolve strongly in the central region around the nuclei, a large number of plane waves must be used to describe correctly these electrons, which increases strongly the computer time [72]. The plane-wave basis set has also some difficulties in describing the core electrons and the valence electrons in the core region. So, the pseudopotential technique was developed and this technique requires the following approximations:

- The electronic properties of the molecules and the solids are mainly governed by the valence electrons while the core electrons can be considered as frozen.
- The central region of the valence electronic wave functions is tiny involved in the chemical properties of the atoms and so, the nucleus potential can be replaced by a smooth pseudopotential.

The first approximation is so-called frozen-core approximation. It describes that the physical and chemical properties of solids are essentially dependent on the valence electrons. It is also expected that the core electrons that do not directly participate to the chemical bonding are only slightly affected by modifications of the atomic environment. It may therefore reasonably be expected that the configuration of the core electrons within the solid is equivalent to that of the isolated atoms and it can be treated as in an isolated atom.

In the second approximation, the pseudopotential approximation is used in which the ionic potential screened by the core electrons is replaced by another fictitious potential such that the valence wavefunctions remain unchanged beyond a given cut-of radius and are replaced by smoothly varying function inside the core region. In practice, a reference calculation is performed on a isolated atom, and then an analytical pseudopotential is fitted to reproduce the all electron calculation.

These two approximations allow to decrease strongly the number of plane waves involved in the Bloch expansion as well as the number of electrons to be considered in the Kohn-Sham equation and so to decrease the computer time required for the calculation.

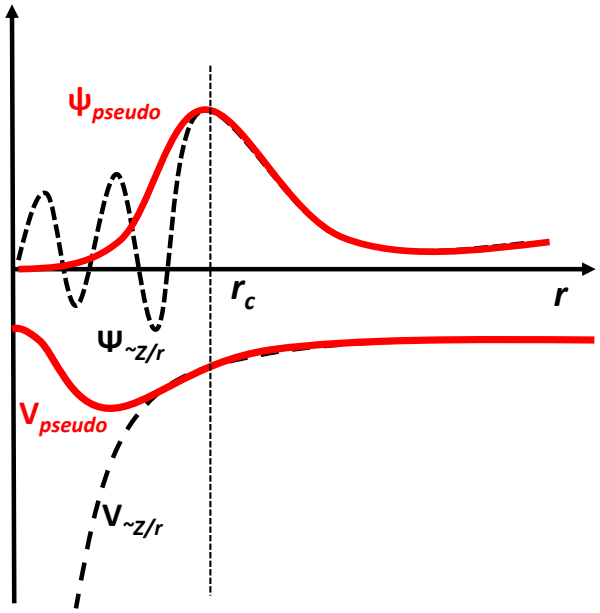

Figure 2.4: Wavefunction in the coulomb potential of the nucleus (black) to the one in the pseudopotential (red). The real and the pseudo wavefunction and the potentials match above a certain cutoff radius r_c (Adapted from Ref. [73]).

2.3.4 Brillouin zone grid

The electronic density is calculated from the integration of the square modulus of the Bloch functions on all occupied energy bands n and over the whole Brillouin zone. The integration over the reciprocal space involve a prior knowledge of the Bloch functions over an infinite number of $\boldsymbol{k}$ points. In practice it is done over a set of selected $\boldsymbol{k}$ points. One of the techniques developed to sample the reciprocal space is the one of H. J. Monkhorst and J. D. Pack [74], which allows to define a finite mesh of $\boldsymbol{k}$ points in each direction. This set of $\boldsymbol{k}$ points depends on the symmetry of the system so it must be converged in each case by increasing its size to reduce the numerical error. In this thesis, we have used the techniques developed by Monkhorst and Pack.

2.4 Technical details

Our first-principles calculations have been performed in the framework of density functional theory (DFT) as implemented in the ABINIT package [1, 75, 76]. We did calculations using

both (i) the local density approximation (LDA) [77] and extended norm-conserving Teter pseudopotentials [78] and (ii) the generalized gradient approximation with the functional proposed by Wu and Cohen (GGA-WC) [79] and optimized pseudopotentials [80] generated with OPIUM code [81]. In both cases, semi-core states were treated as valence electrons, considering explicitly the following levels in the calculation: $5s$, $5p$ and $6s$ for the Pb atom, $4s$, $4p$ and $5s$ for the Sr atom, $3s$, $3p$, $3d$ and $4s$ for the Ti atom and $2s$ and $2p$ for the O atom. The wavefunction was expanded on a plane-wave basis set. Convergency was reached using a plane-wave energy cutoff of 45 hartrees.

In the five-atom perovskite ABO_3 unit cell, a Monkorsh-Pack mesh of $6\times6\times6$ k points was used to sample the Brillouin zone. When condensing the AFD instabilities, we considered either a 20-atom supercell corresponding to $\sqrt{2}a_0$= a=b, and c= $2a_0$, and a sampling of $6\times6\times4$ k points or, for the *Cmcm* phase, a 40-atom supercell corresponding to $2a_0$, $2a_0$, and $2a_0$ and a sampling of $4\times4\times4$ k points. We explicitly checked that the relative energy of the different phases is well converged and independent of the choice of the supercell. Structural relaxations were performed until the forces were smaller than 10^{-7} hartrees/bohr and stresses are smaller than 10^{-8} hartrees/bohr^3. The vibrational properties, Born effective charges and dielectric tensors were calculated using the density functional perturbation theory (DFPT) [82]. The spontaneous polarization were computed making use of the Berry phase formalism [20].

2.5 Landau-Ginzburg-Devonshire theory (LGD)

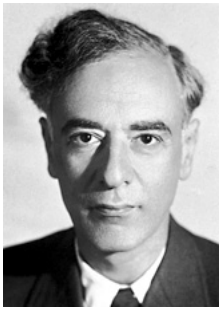

Figure 2.5: Lev Landau was awarded Nobel prize in 1962 for the first to identify the role of the order parameter and to develop a general theory of phase transitions (Adapted from Ref. [63]).

2.5.1 Introduction

Landau theory in physics was introduced by Lev Landau in an attempt to formulate a general theory of second-order phase transitions. This is an important and most popular approach to describe the temperature behavior of the ferroelectrics at the phenomenological level [83]. The basic idea of Landau theory is that the phase transition is described by an order parameter, i.e., a quantity that switches from zero to non-zero at the phase transition and modify the symmetry of the system. In ferroelectrics, the order parameter can be the spontaneous polarization (P), (or the amplitude of the atomic distortions giving rise to it). The free energy, F above and below the transition can be generally expressed as a polynomial expression in terms of the order parameter.

2.5.2 General Formalism

When the pressure is neglected, at a given temperature, the stable phase is the one minimizing the free energy:

$$F = U - TS, \tag{2.5.1}$$

where T is the temperature, S is the entropy and U the internal energy. In case of the FE phase transitions, the order parameter is the polarization P. Following a simplified Landau-Devonshire description where the strain is neglected, the free energy of a ferroelectric material can be then described as a Taylor expansion in terms of the polarization only as follows:

$$F(P) = \frac{1}{2}A(T - T_0)P^2 + \frac{1}{4}BP^4 + \frac{1}{6}CP^6, \tag{2.5.2}$$

where the expansion is truncated to the sixth term, A, B and C are the independent coefficients, T is the temperature and T_0 is the Curie temperature.

By applying the value of internal energy, F from the Eq. 2.5.1, we get the following expression:

$$U(P) = -\frac{1}{2}AT_0P^2 + \frac{1}{4}BP^4 + \frac{1}{6}CP^6. \tag{2.5.3}$$

The entropic term TS gives the temperature dependence with the entropy as:

$$S = -\frac{1}{2}AP^2. \tag{2.5.4}$$

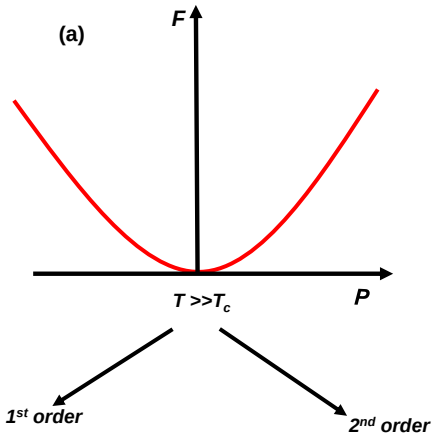

Figure 2.6: Landau free energy as a function of polarization for the paraelectric phase.

In the description of landau theory:

- A and C coefficients are positive in all the ferroelectrics
- the sign of the B coefficient determines the nature of the phase transition between the ferroelectric and paraelectric phases.
- When $T >> T_0$, the system is paraelectric with a single-well shape of the free energy as shown in Fig. 2.6.
- When $T << T_0$, the system is in its ferroelectric phase with a double-well shape of the free energy with respect to the polarization as shown in Fig. 2.7.

2.5.3 Second order transition

If $B > 0$, then no sixth order term is needed (we assume C=0) and the paraelectric-ferroelectric transition takes place at $T = T_0$, and the free energy evolves continuously from the single-well to the double well as shown in the Fig. 2.7 (b) so, this is related to the second-order phase transition.

In the ferroelectric phase, the spontaneous polarization (P_0) of the material is given at the two minima of the double well ($\pm P_0$) and this can be estimated at E=0 by applying the

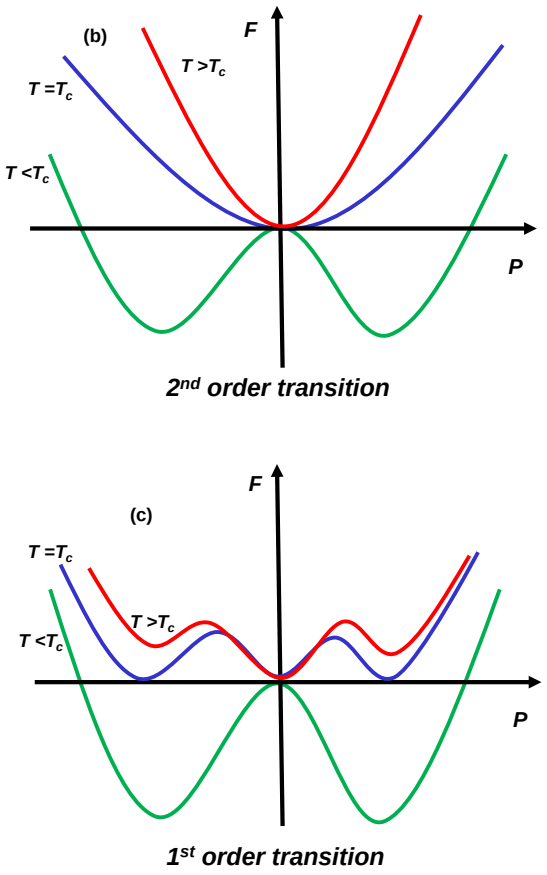

Figure 2.7: (b) Landau free energy as a function of polarization for the ferroelectric material for the second-order phase transition at $T > T_0$, $T = T_0$ and $T < T_0$ and (c) Free energy as a function of the polarization, for a ferroelectric material in a first-order transition at $T > T_0$, $T = T_0$ and $T < T_0$.

conditions:

$$\frac{\partial F}{\partial P} = 0 \tag{2.5.5}$$

and

$$\frac{\partial^2 F}{\partial P^2} > 0 \tag{2.5.6}$$

which give rise to the following solutions where the sixth order term is neglected. The solution is:

$$P_0 = \pm\sqrt{\left(\frac{a}{b}\right)(T_0 - T)}. \tag{2.5.7}$$

The spontaneous polarization increases with decreasing temperature and vanishes for $T \geq T_0$ which is shown in Fig. 2.8 (d) and the dielectric susceptibility

$$\chi = \partial P/\partial E|_{P_0} \tag{2.5.8}$$

$$\chi = [a(T - T_0)]^{-1} \qquad \text{for} \qquad T > T_0 \tag{2.5.9}$$

$$\chi = [2a(T_0 - T)]^{-1} \qquad \text{for} \qquad T < T_0 \tag{2.5.10}$$

follows the Curie-Weiss evolution. Hence, the dielectric susceptibility diverges at $T = T_0$ which can be seen in Fig. 2.8 (f).

2.5.4 First order transition

If $B < 0$, then the order parameter jumps discontinuously and the phase transition is called as the first-order transition. It results that, even when $T > T_0$, the free energy may have two local minima at non-zero polarization P as seen in Fig. 2.7 (c).

When the temperature is reduced, the polar phase becomes the most favorable at the Curie temperature T_c which is different and larger than the T_0 and is defined in Eq. (2.5.2). The paraelectric phase corresponds to a local minimum of the free energy between T_c and T_0. When we see the evolution of temperature versus the polarization in Fig. 2.8 (e), we see that it displays a discontinuous jump to zero at $T = T_c$ and the evolution of dielectric susceptibility with respect to the temperature displays a finite jump at T_c that is shown in Fig. 2.8 (g).

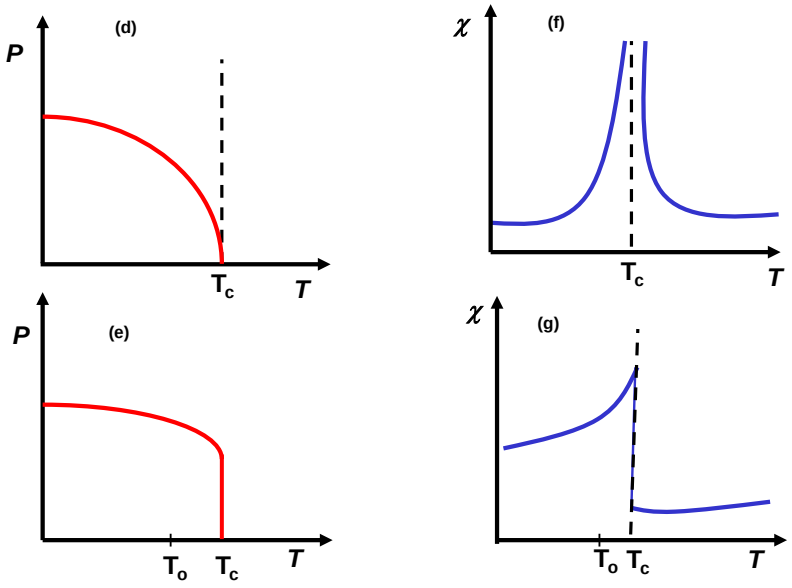

Figure 2.8: (d) Evolution of the spontaneous polarization P with respect to the temperature for the second-order phase transition; (e) Evolution of the spontaneous polarization P with respect to the temperature for the first-order phase transition; (f) Evolution of the susceptibility (χ) with respect to the temperature for the second-order phase transition; (g) Evolution of the susceptibility (χ) with respect to the temperature for the first-order phase transition.

2.6 Practical study of real perovskites

In general there are 3 complexifications in dealing with real perovskites while studying the Landau theory for complex calculations. They are:

- Polarizations (P) is not a scalar but a vector quantity including P_x, P_y and P_z polarization components. The appearance of P produces a small relaxation of the unit cell. The energy expansion in terms polarization requires much more terms with all the possible combinations or the cross products of P_x, P_y and P_z.

- Strain (η) is a key ingredient for the strain engineering and is an important secondary Landau parameter that needs to be included explicitly. When dealing with strain, the internal energy depends on both P and η degrees of freedom so the elastic energy term and the coupling between polarization and strain should be included. The strain components are denoted in Voigt's notation. Similarly, free energy can be also expressed in terms of stress (σ), components and Legendre transformation is used to switch from strain to stress. A fundamental postulate of thermodynamics applied to a ferroelectric is that its free energy, F can be generally expressed as a function of ten variables (three components of polarization, six components of stress tensor and finally one of the temperature). So, the formulation becomes much more complicated.

- Competing structural instabilities like AFD oxygen motions can be important and sometimes needed to be treated explicitly. Now the double well energy rotations (ϕ), also plays a major role so both the FE and AFD energy wells should be included. For the free energy expansion the coupling between ϕ and η, ϕ and P should be considered. Such case has been already reported in the literature for instance by Pertsev *et.al* [51].

2.7 Technical details

For the study of $PbTiO_3$ in Chapter 3, we have used the Landau model developed by Qiu *et al.* [84]. They have used a non-linear LGD thermodynamic theory to study the misfit strain-film thickness phase diagrams for epitaxial PZT ferroelectric thin films. The

expression is:

$$\begin{aligned} G_{bulk} = \; & a_1(P_1^2+P_2^2+P_3^2)+a_{11}(P_1^4+P_2^4+P_3^4)+a_{12}(P_1^2P_2^2+P_2^2P_3^2+P_3^2P_1^2) \\ & +a_{111}(P_1^6+P_2^6+P_3^6)+a_{112}(P_1^4(P_2^2+P_3^2)+P_2^4(P_1^2+P_3^2)+(P_3^4)(P_1^2+P_2^2)) \\ & +a_{123}((P_1P_2P_3)^2)-(0.5)(s_{11})(\sigma_1^2+\sigma_2^2+\sigma_3^2)-s_{12}(\sigma_1\sigma_2+\sigma_1\sigma_3+\sigma_2\sigma_3) \\ & -(0.5)s_{44}(\sigma_4^2+\sigma_5^2+\sigma_6^2)-Q_{11}(\sigma_1P_1^2 \\ & +\sigma_2P_2^2+\sigma_3P_3^2)-Q_{12}(\sigma_1(P_2^2+P_3^2)+\sigma_2(P_1^2+P_3^2)+\sigma_3(P_1^2+P_2^2)) \\ & -Q_{44}(\sigma_4P_2P_3+\sigma_5P_1P_3+\sigma_6P_1P_2). \end{aligned} \tag{2.7.1}$$

Here, P_i are the components of the total polarization vector in Eq. (2.7.1); a_i, a_{ij} and a_{ijk} are the dielectric stiffness coefficients, σ_i are the components of the external stress tensor and Q_{ij} are the electrostrictive coefficients. We have considered P and σ terms in the Landau expression of free energy.

For the study of $SrTiO_3$ in Chapter 4, we have used the Landau model by Pertsev *et al.* [51] and in this work they have used a LGD-type theory to describe the mechanical substrate effect on equilibrium states and phase transitions in $SrTiO_3$ epitaxial thin films. The misfit strain-temperature phase diagram of $SrTiO_3$ films is developed taking into account the existence of two coupled instabilities (AFD and FE). The full model is provided in Chapter 4. We have considered P, η and ϕ terms in the Landau expression of free energy.

Chapter 2: Theoretical Approach: Methods and Models

Chapter 3

Study of $PbTiO_3$ under uniaxial strains and stresses

The aim of this Chapter is to discuss in detail the effect of mechanical constraints on $PbTiO_3$ with uniaxial mechanical strains and stresses. Then we present results based on a Landau-Ginzburg-Devonshire (LGD) model which has been developed to study the uniaxial mechanical constraint effect on $PbTiO_3$.

3.1 Introduction

ABO_3 perovskites form a very important class of functional materials that can exhibit a broad range of properties (e.g., superconductivity, magnetism, ferroelectricity, multiferroism, and metal-insulator transitions) within small distortions of the prototype cubic structure. Among them, $PbTiO_3$ is a prototypical ferroelectric compound and also one of the parent components of the $Pb(Zr,Ti)O_3$ solid solution (PZT), which is the most widely used piezoelectric [85].

Bulk $PbTiO_3$ crystallizes at high temperature in the paraelectric $Pm\bar{3}m$ cubic structure. Under cooling, it then undergoes, at 760 K, a structural phase transition to a ferroelectric (FE) phase of $P4mm$ symmetry. At room temperature, it possesses a large spontaneous polarization $P_s \approx 80\ \mu C/cm^2$. In contrast to $BaTiO_3$ and $KNbO_3$, which exhibit additional ferroelectric transitions to phases of orthorhombic and rhombohedral symmetries, $PbTiO_3$

remains tetragonal down to 0 K, a feature that was attributed to its large c/a ratio [23]. As revealed by the inspection of the phonon dispersion curves of its cubic phase [86], on top of its ferroelectric instability, $PbTiO_3$ also develops strong antiferrodistortive (AFD) instabilities, which are associated with rotations (tilts) of the oxygen octahedra. Although these AFD instabilities are suppressed by the appearance of the dominant FE motions, they nevertheless constitute important hidden instabilities that can significantly affect its physical and structural properties. For instance, it was recently highlighted theoretically that AFD motions shift down the ferroelectric phase-transition temperature of $PbTiO_3$ by a few hundred Kelvin [87]. Also, although they do not naturally appear in bulk, AFD motions can condense at the $PbTiO_3$ surface [88] where the FE-AFD competition is modified.

In ABO_3 compounds, FE and AFD instabilities are highly sensitive to mechanical constraints such as strains and stresses, which can thus be used in practice to tune the phase-transition temperatures and the multifunctional properties [85]. Under increasing *isotropic* pressure, the ferroelectric instability is well known for disappearing quickly, an intrinsic feature that has to be properly handled when doing first-principles calculations within the local-density approximation, which tends to underestimate systematically bond lengths and unit-cell volumes [89]. Unexpectedly, in $PbTiO_3$, Kornev *et al.* [41] showed that, although ferroelectricity is indeed progressively suppressed at low isotropic pressure, it reappears at ultrahigh pressure, a feature also predicted in $BaTiO_3$ [42]. Following this work the phase diagram of $PbTiO_3$ under isotropic pressure has recently been reinvestigated by Janolin *et al.* [90]: they highlighted a complex sequence of phases accommodating pressure through mechanisms involving not only the reentrance of ferroelectricity but also oxygen octahedra tilting, which are known to be favored at smaller volumes.

Engineering ferroelectricity through *biaxial* epitaxial strain in ABO_3 thin films has also attracted much attention over the last decade [91–93]. Thanks to the advances in the deposition of coherent epitaxial films of complex oxides [94], it has become possible to impose epitaxial strains of the order of 4% or even larger to thin-film perovskites. It is now well understood that the substrate-induced biaxial strain has a strong bearing on the ultimate behavior of ferroelectric thin films [50, 95, 97]. Prototypical demonstrations of this include the strong amplification of ferroelectricity in strained $BaTiO_3$ [48] and the possibility to achieve room-temperature ferroelectricity in strained $SrTiO_3$ [49, 96]. Such behaviors were predicted by Landau theory [95, 97] and were further analyzed from first-

principles investigations [50]. Strain engineering of ferroelectricity was also considered to be a promising route to convert paraelectric magnets into multiferroics [98], for instance, in $CaMnO_3$ [99, 100] and is not restricted to perovskites [101]. Beyond acting simply on the ferroelectric mode as initially targeted, strain engineering also proved to be useful for tuning the competition with other instabilities and getting novel unexpected phases such as in $BiFeO_3$ under either in-plane compressive [102, 103] or tensile [104] strains or in $EuTiO_3$ [105] and $SrMnO_3$ [106] in combination with magnetism. In $PbTiO_3$ it was predicted from first-principles that, while moderate compressive strain will favor the $P4mm$ ferroelectric phase and amplify the spontaneous polarization, tensile epitaxial strain should favor an $Ima2_1$ phase [107–109] combining in-plane FE polarization (along the [110] direction) and in-plane AFD oxygen rotations ($a^-a^-c^0$ in Glazer's notations [11, 110]). Additional $I4cm$ and $Pmc2_1$ phases have also been predicted at larger compressive and tensile strains, respectively [108].

While the effect of isotropic and biaxial mechanical constraints on the ferroelectric properties has been widely investigated, our study is motivated by the little-understood effect of *uniaxial* strain and stress. Emelyanov *et al.* discussed, using a thermodynamical theory, the additional effect of uniaxial stress produced by uniform loading of epitaxial thin films of $BaTiO_3$ and $PbTiO_3$ under biaxial strain [111]. Also, the role of uniaxial strain on $PbTiO_3$ ultrathin slabs has been studied by Umeno *et al.* from first principles [112]; they reported the possibility to observe a combination of FE and AFD distortions, although the appearance of the latter might result from a surface, rather than a purely strain, effect. More recently, Duan *et al.* [61] investigated the role of uniaxial stress on bulk $PbTiO_3$, but they did not consider the possible interplay between ferroelectricity and AFD motions; moreover, as will become more clear below, their conclusions are biased by the fact that they restricted themselves to a particular phase.

In this Chapter, we want to study more systematically the role of uniaxial mechanical constraints in monodomain $PbTiO_3$, clarifying if it leads to a suppression of FE in favor of AFD distortions or if FE structures are favored at any uniaxial strain or stress state. We wish to explore if uniaxial strain or stress can lead to new structures in $PbTiO_3$; we are motivated by the fact that perovskites with competing FE and AFD instabilities can show a multitude of structures under deformation, as observed not only under biaxial or isotropic constraints for in $PbTiO_3$ but also under biaxial strain for $BiFeO_3$ [103] and

under hydrostatic pressure for $BiFeO_3$ [10] and $BiMnO_3$ [113]. To do so, we perform first-principles calculations within density functional theory in order to determine the ground state of $PbTiO_3$ under uniaxial strains and stresses.

3.2 Technical Details

The calculations details for FP and LGD are described in Chapter 2, in the technical details section. In what follows, we consider that the x, y and z cartesian axis are aligned respectively with the cell vectors a, b and c of the reference cubic structure. Then, the uniaxial constraint is always applied along the z direction as illustrated in Fig. 3.1. Both fixed uniaxial strain and fixed uniaxial stress conditions are considered.

To label the ferroelectric and antiferrodistortive motions compatible with a given space group, we use "extended" Glazer's notations in which the superscripts refer as usual to the rotation pattern and a subscript P is added to identify the direction(s) along which a polarization can develop. When reporting phonon labels, we consider that the Ti atom is at the origin.

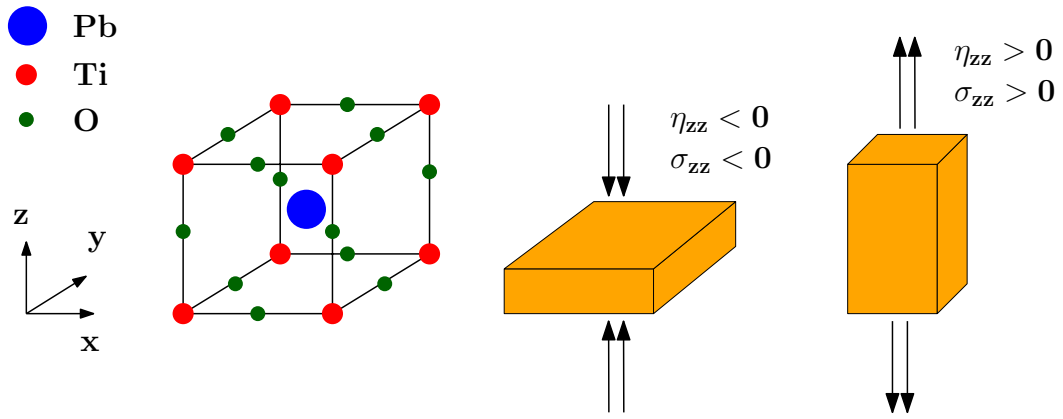

Figure 3.1: Cubic perovskite structure of $PbTiO_3$, with the Ti atom at the origin. Pb atoms are located at the center (in blue), Ti atoms at the corners (in red), and O atoms at the middle of the edges (in green). The uniaxial mechanical constraint (fixed strain η_{zz} or fixed stress σ_{zz}) is applied along the z-axis .

3.3 Bulk structure

First, we reinvestigate the highly symmetric cubic perovskite structure of $PbTiO_3$. In this cubic phase, the atomic positions are fixed by symmetry, and the only structural parameter to be relaxed is the lattice constant a_0. Our relaxed lattice constants $a_0^{LDA} = 3.880$ Å and $a_0^{GGA} = 3.933$ Å are comparable to previous calculations ($a_0^{LDA} = 3.874$ Å [61]) and are in satisfactory agreement with experimental data ($a_0^{EXP} = 3.93$ Å [114]). As expected, the LDA tends to underestimate the experimental lattice constant, which is better reproduced at the GGA-WC level.

The calculated phonon dispersion curves of cubic $PbTiO_3$ shown in Fig. 3.3, are also in agreement with previous studies [86]. They show two main phonon instabilities: (i) a zone-center FE unstable mode Γ^{4-} (F_{1u}) at 109i (151i) cm^{-1} in LDA (GGA-WC) corresponding to a polar displacement of cations against the oxygen and (ii) a zone-boundary AFD unstable mode R^{4+} at 98i (79i) cm^{-1} in LDA (GGA-WC) corresponding to rotations of the oxygen octahedra, with consecutive octahedra along the rotation axis moving antiphase (a^- in Glazer's notations). As usual in perovskites, we notice that the AFD instability at the R point propagates to the M point through a M^{3+} mode at 73i (53i) cm^{-1} in LDA (GGA-WC), where consecutive octahedra move in phase (a^+ in Glazer's notations). The main difference between LDA and GGA-WC results comes from the smaller LDA volume, which favors the AFD instabilities and reduces the FE instability.

From this discussion, it appears that, at the harmonic level, the FE instability is stronger than the AFD instabilities. However, this does not necessarily imply a FE ground state. In Table 3.1, we report the energy and structural parameters of different metastable phases resulting from the condensation of the FE mode at Γ and AFD modes at R and M points. Both LDA and GGA-WC correctly reproduce the $P4mm$ ferroelectric ground state. We see that in the absence of FE instability, $PbTiO_3$ would prefer to develop a^- rotation patterns and would adopt either the $Imma$ ($a^-a^-c^0$) phase or the $R\bar{3}c$ ($a^-a^-a^-$) phase, which both appear to be nearly degenerated in energy in our calculations (i.e., with a difference of energy smaller than 1 meV/f.u.). The $I4/mcm$ ($a^0a^0c^-$) phase is also very close in energy. In comparison, the a^+ rotation pattern never produces a substantial gain in energy; in line with this, we notice that atomic relaxations in the $Cmcm$ ($a^0b^+c^-$) and $Pbnm$ ($a^-a^-c^+$) symmetries relax back to the $I4/mcm$ and $Imma$ phases, respectively, proving that the

appearance of the a^- rotation suppresses the instability associated to a^+ motions.

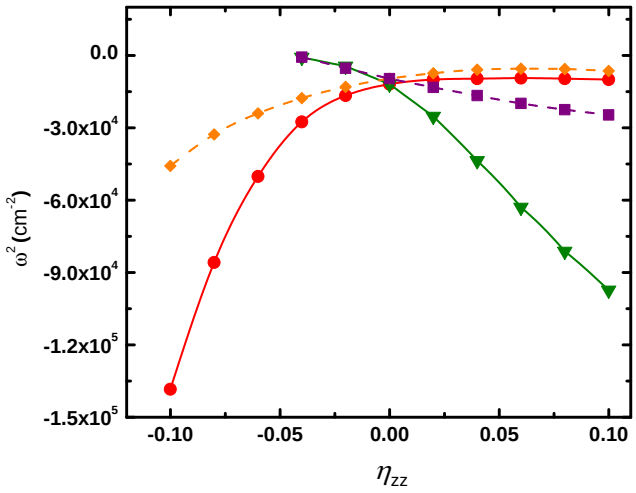

Figure 3.2: Evolution of the square of the frequency of the FE modes Γ^{3-} (green triangles) and Γ^{5-} (red circles) and of the AFD modes A_3^+ (purple squares) and A_5^+ (orange diamonds) with uniaxial strains in the paraelectric $P4/mmm$ phase of $PbTiO_3$, as obtained within the LDA. Similar results have been obtained within the GGA-WC.

Applying uniaxial strain along the z direction and relaxing the lattice constant along the two other directions while keeping the atoms at their high-symmetry position makes the paraelectric reference unit cell tetragonal, bringing the system from $Pm\bar{3}m$ to $P4/mmm$ symmetry. This splits the triply degenerated Γ^{4-} (F_{1u}) FE mode into a single Γ^{3-} (A_1) mode and a doubly degenerated Γ^{5-} (E) mode, polarized along the c axis and perpendicular to it, respectively. Similarly, the triply degenerated R^{4+} AFD mode is split into a single A_3^+ mode and a doubly degenerated A_5^+ mode, corresponding to oxygen rotations around the z axis and around the x and y axes, respectively. The evolution of the frequencies of these modes with uniaxial strain is reported in Fig. 3.2. It appears that while the FE instability is only marginally more unstable than the AFD instability at the bulk level, both tensile and compressive uniaxial strains destabilize one of the FE modes (Γ^{3-} under tension and Γ^{5-} under compression) more strongly than any of the AFD ones. Although limited to the harmonic level, this observation already suggests that the behavior of $PbTiO_3$ under uniaxial mechanical constraints is strongly dominated by the FE instability.

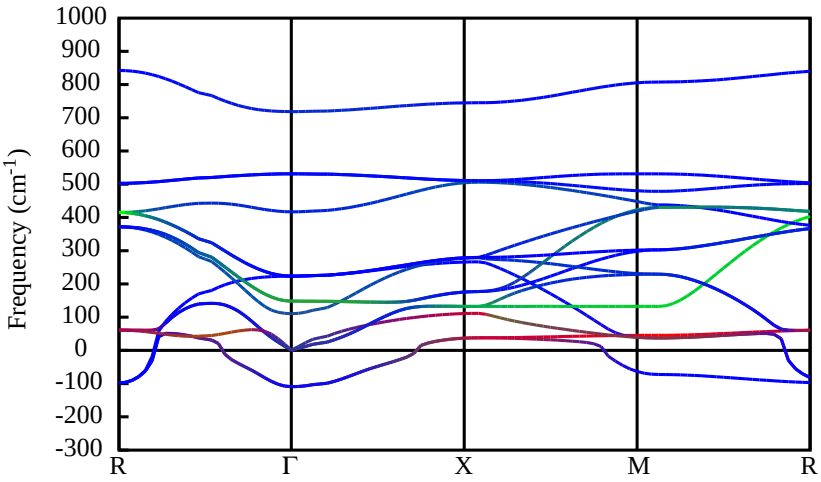

Figure 3.3: Calculated phonon dispersion curve of cubic $PbTiO_3$, at the LDA volume along the path R–Γ–X–M–R of the Brillouin zone.

3.4 Uniaxial strain

Let us now focus on the behavior of $PbTiO_3$ under uniaxial strain. The mechanical constraint is applied along the z axis by fixing the c lattice parameter. Then, structural relaxations are performed under different symmetry constraints in order to compare the stability of different metastable phases for different amplitudes of the strain η_{zz}. The most stable phase at a given η_{zz} is that which minimizes the internal energy U. The results obtained in LDA are summarized in Fig. 3.4(a), and GGA-WC results are given in Fig. 3.4(b). In the following, we mostly refer to LDA results, unless a further consideration of GGA-WC is pertinent.

The relaxed $Pm\bar{3}m$ cubic phase of $PbTiO_3$ has a lattice constant $a^{LDA} = 3.880$ Å ($a^{GGA} = 3.935$ Å) and is chosen to be the common reference for both the internal energy ($U = 0$) and the strain [$\eta_{zz} = (c - c_0)/c_0$ with $c_0 = a^{LDA}$ or a^{GGA}].

Applying a strain η_{zz} to the paraelectric $Pm\bar{3}m$ phase while keeping the atoms at their high-symmetry positions brings the system into the $P4/mmm$ symmetry (black squares in Fig. 3.4). As highlighted in the previous section, this paraelectric (PE) phase is not the ground state: it exhibits different FE and AFD instabilities, the condensation of which will necessarily lower the internal energy.

Distinct polar phases, with their polar axes aligned along different directions, have been

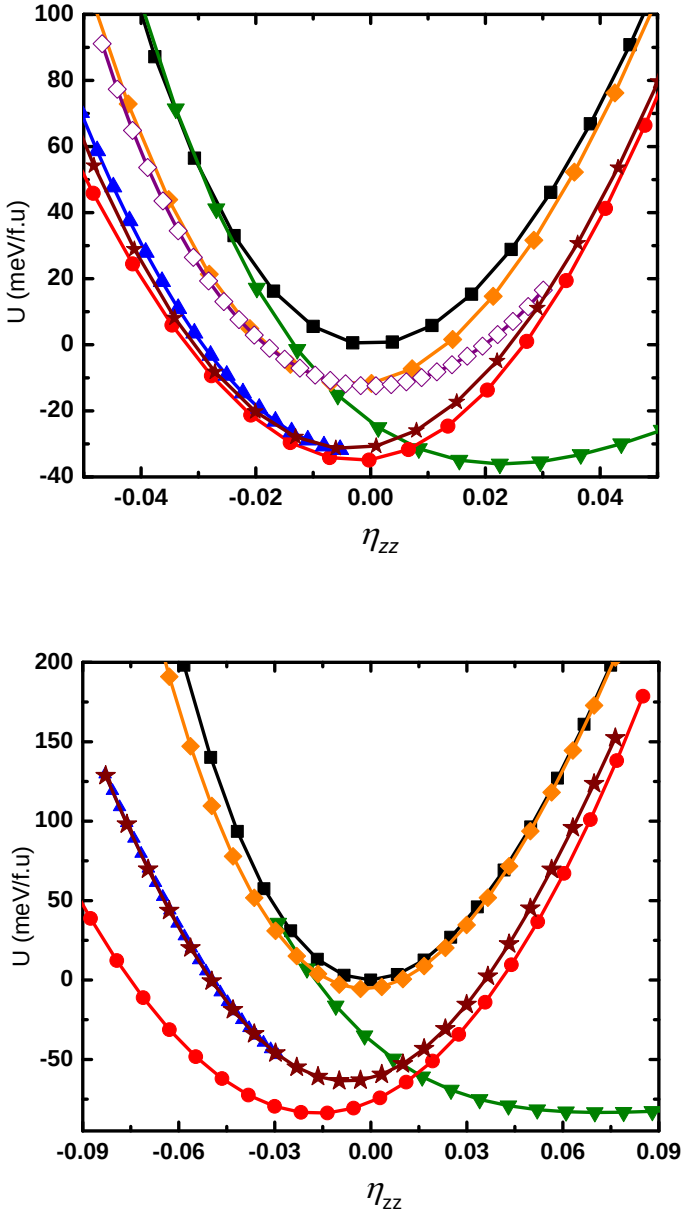

Figure 3.4: Internal energy U (meV/f.u.) of different metastable phases of $PbTiO_3$ under uniaxial strain as computed within (a) the LDA and (b) the GGA-WC. The phases are as follows: PE ($P4/mmm$, black squares), FE_z ($P4mm$, green downward triangles), FE_{xy} ($Amm2$, blue triangles), FE_x ($Pmm2$, red circles), AFD_{xy} (orange diamonds), AFD_{xyz} (open purple diamonds), and AFD_{xy}+FE_{xy} (brown stars).

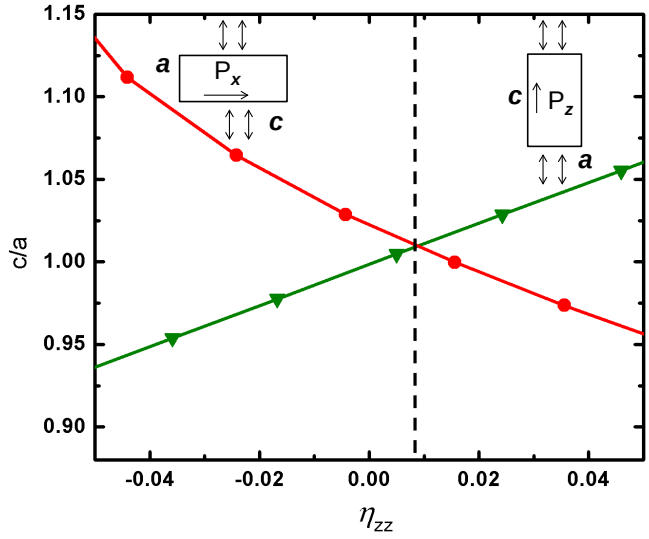

Figure 3.5: Evolution of the c/a ratio of the relaxed FE_x ($Pmm2$) and FE_z ($P4mm$) phases of $PbTiO_3$ with the uniaxial strain as obtained in LDA.

relaxed. They are labeled FE_z ($P4mm$), FE_x ($Pmm2$), or FE_{xy} ($Amm2$) depending on whether the polar axis is along the [001], [100], or [110] direction, respectively [115]. We see in Fig. 3.4 that the FE_z and FE_x curves have their minima at the same internal energy for a value of strain associated in LDA (GGA-WC) to $c = 3.975$ Å (4.243 Å) and $a = 3.863$ Å (3.880 Å), which correspond to the c and a relaxed lattice constants of the bulk $P4mm$ ground state. The relative position of these two curves is such that the FE_x phase appears to be the most stable for $\eta_{zz} < +0.8\%$, while the FE_z phase is favored under tensile strains $\eta_{zz} > 0.8\%$. In Fig. 3.5 we have plotted the c/a ratio of the FE_z and FE_x phases: we see that the crossing of the two curves coincides with the change in stability of the two phases, emphasizing that $PbTiO_3$ prefers, at each strain, the phase that maximizes its c/a ratio.

We notice also in Fig. 3.4 that, contrary to what was proposed in Ref. [61], the paraelectric configuration is never the most stable. In agreement with that work, we see in Fig. 3.6 that $PbTiO_3$ cannot sustain a spontaneous polarization along z under large compressive strain $\eta_{zz} < -2.5\%$ (i.e., the $P4mm$ curve coincides with the $P4/mmm$ curve for $\eta_{zz} < -2.5\%$), but the system does not become paraelectric: instead, it prefers to stay ferroelectric and to develop a polarization in the perpendicular direction ($Pmm2$ phase). Under both tensile and compressive strains, the polarization is typically enhanced compared to the bulk value

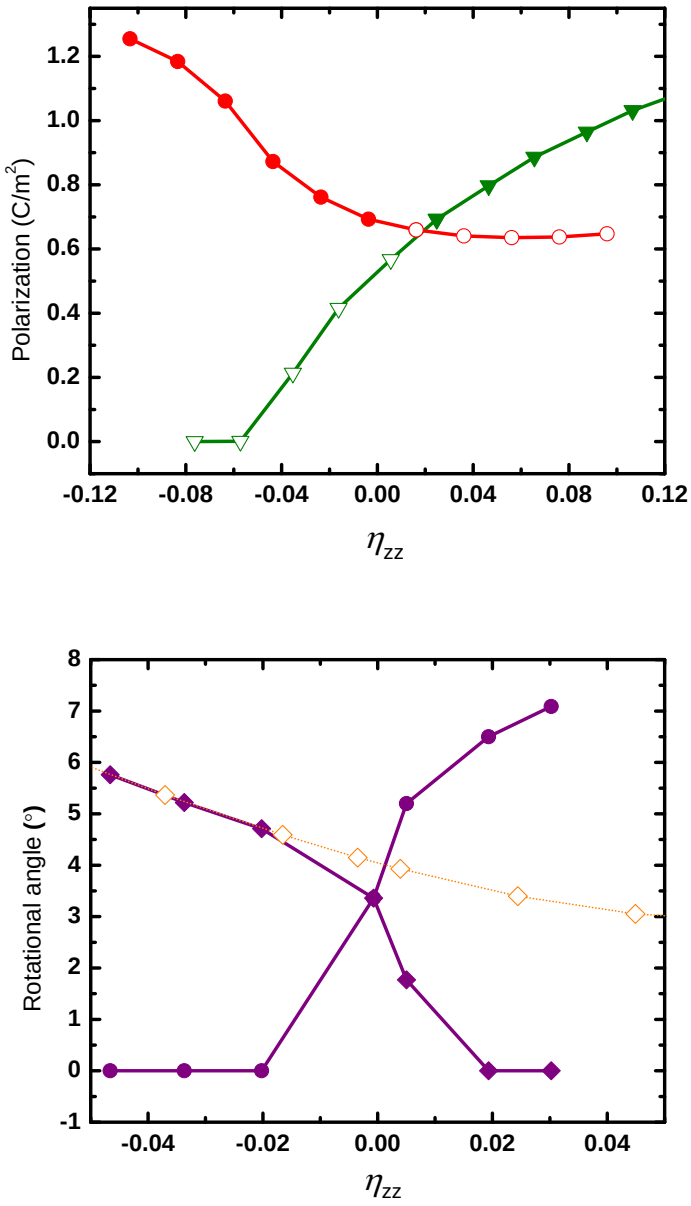

Figure 3.6: (Top) Evolution of the polarization of the FE_x (red circles) and FE_z (green triangles) phases of $PbTiO_3$ with the uniaxial strain, as predicted within the LDA. Solid symbols correspond to the region where the phase is the ground state [116]. (bottom) Evolution of the rotational angles of the AFD_{xy} and AFD_{xyz} phases of $PbTiO_3$ with the uniaxial strain, as predicted within the LDA. Purple solid circles and diamonds indicate c^- and a^- rotation angles of the AFD_{xyz} phases, respectively, and orange open diamonds indicate a^- rotation angles of the AFD_{xy} phases.

(Fig. 3.6).

Independently, we also considered different possible phases including AFD motions. According to what was discussed for the bulk, we only considered the most favorable a^- AFD motions. The AFD_{xy} ($Imma$) and AFD_{xyz} ($C2/c$) phases are compatible with the rotation patterns $a^-a^-c^0$ and $a^-a^-c^-$, respectively. The strain evolution of the relaxed rotation angles of both phases are shown in Fig. 3.6. We observe that the relaxed AFD_{xyz} phase only combines rotations along the three Cartesian directions in a small region of strain, around $\eta = 0$: under tensile strain, it prefers a purely $a^0a^0c^-$ rotation pattern, while under compressive strain, it prefers a purely $a^-a^-c^0$ rotation pattern (i.e., it reduces to the AFD_{xy} phase). In all cases, the gain of energy produced by the AFD motions is much smaller than what can be obtained from the polar distortion.

It is also worth noticing in Fig. 3.4 that, like at the bulk level, the polarization always prefers to stay aligned with one of the pseudocubic axes (z or x) and that the FE_{xy} phase is never the most stable. Nevertheless, its energy is very close to that of the FE_x phase. In contrast, under compressive uniaxial strain, for which lattice constants perpendicular to the constrained direction are elongated, the FE_{xy} phase develops an AFD instability. This instability is associated with the $a^-a^-c^0$ AFD motions of the AFD_{xy} phase, which appears to be the most favorable AFD configuration under compressive strain. Condensing these additional AFD motions in the FE_{xy} phase brings the system into a FE_{xy}+AFD_{xy} phase ($a^-_Pa^-_Pc^0$ in generalized Glazer's notation) of $Ima2_1$ symmetry that is lower in energy than the purely FE_{xy} phase but is never more stable than the FE_x phase. This result is in contrast to the prediction of an $Ima2_1$ ground state for $PbTiO_3$ under tensile epitaxial biaxial strain [109]. The difference in behavior can be explained by the fact that the biaxial tensile strain forces two elongated lattice constants to be equal, favoring a FE_{xy}+AFD_{xy} distortion, while under uniaxial compressive strain, the lattice constants in the two directions perpendicular to the constraint are similarly elongated but the system keeps the freedom to break the symmetry between them.

We see in Fig. 3.4(b) that the gains in energy associated with the FE distortions are amplified and those associated with AFD motions are significantly reduced with the GGA-WC in comparison to the LDA. Still, the system switches from a FE_x ground state to a FE_z ground state at a relatively similar critical strain, $\eta_{zz} = 1.5\%$.

In summary, under uniaxial strain, $PbTiO_3$ adopts a purely ferroelectric ground state independent of the strain amplitude, with the polarization aligned either along the constrained direction (FE_z phase) for $\eta_{zz} >\sim +1\%$ or perpendicular to it, along one of the pseudocubic directions (FE_x phase), for $\eta_{zz} <\sim +1\%$. This prediction concerns bulklike $PbTiO_3$ under uniaxial strain. The conclusions might be different in the vicinity of surfaces that favor the appearance of AFD motions and therefore in ultrathin slabs, as previously discussed by Umeno *et al.* [112].

3.5 Uniaxial stress

Since it is more easily accessible experimentally, let us now consider the behavior of $PbTiO_3$ under uniaxial stress σ_{zz}. In this case, the stable phase is the one which minimizes the mechanical enthalpy $F = U - \sigma_{zz}\eta_{zz}$ (in our conventions, a positive σ_{zz} is tensile). The evolution of σ_{zz} with η_{zz} is reported in Fig. 3.7(a) for a few selected phases. At $\sigma_{zz} = 0$, the FE_z phase shows the lowest elastic constant, which can be explained from the polarization-strain coupling.

The evolution of the mechanical enthalpy of the different phases with σ_{zz} is summarized in Fig. 3.7(b). We see that, like for fixed uniaxial strain, the ground state of $PbTiO_3$ under fixed uniaxial stress is always purely ferroelectric. The transition stress between the FE_x and FE_z phases is $\sigma_{zz} = 0$, in agreement with the fact that the common tangent between FE_x and FE_z curves is horizontal in the energy versus strain graph (Fig. 3.4). This transition stress that, at $\sigma_{zz} = 0$, the system has degenerated ground states, which corresponds to having the polarization either along z (FE_z phase) or perpendicular to it (FE_x phase) [117]. As expected, the presence of uniaxial tensile stresses always favors the FE_z phase, while uniaxial compressive stresses always stabilizes the FE_x phase. Again, under compression, the AFD_{xy}+FE_{xy} phase appears to be very low in energy and below the FE_{xy} phase, but is never more stable than the FE_x phase.

Since the AFD motions does not appear to be directly involved in the ground state, the behavior of $PbTiO_3$ under uniaxial strain can be further explored using a simple Landau-Ginzburg-Devonshire (LGD) theory while including the order parameter P and neglecting the AFD degrees of freedom. The phase diagram of $PbTiO_3$ under uniaxial stress predicted

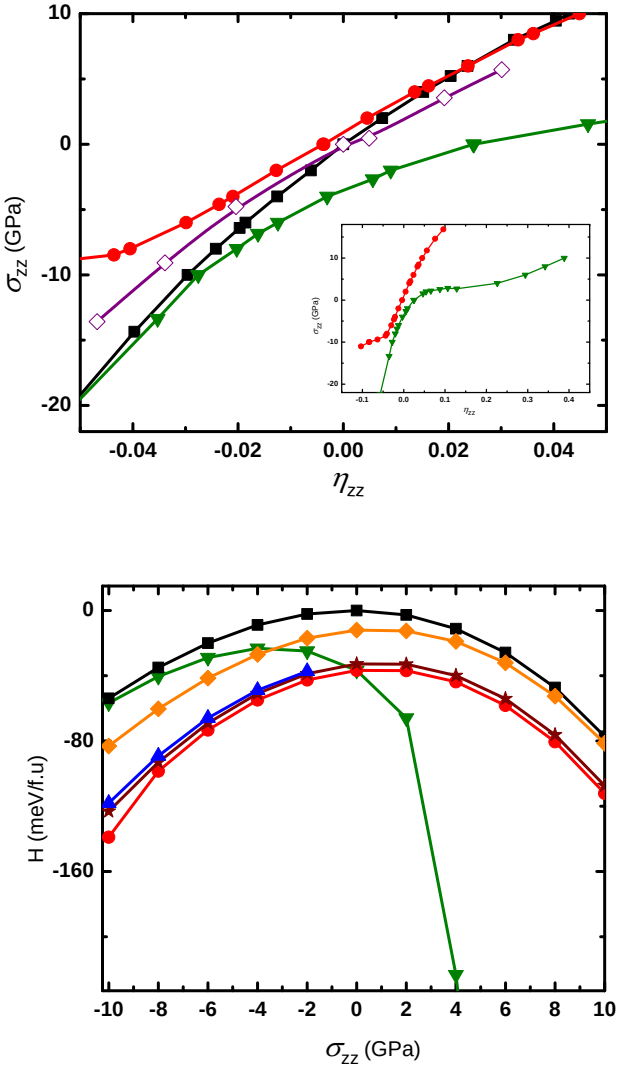

Figure 3.7: (Top) Evolution of the stress (GPa) with the uniaxial strain for a few selected phases as computed within the LDA. (bottom) Mechanical enthalpy H (meV/f.u.) of different metastable phases of $PbTiO_3$ under uniaxial stress as computed within the LDA. The considered phases are as follows: PE (black squares), FE_z (green downward triangles), FE_{xy} (blue triangles), FE_x (red circles), AFD_{xy} (orange diamonds), and AFD_{xy}+FE_{xy} (brown stars).

from the LGD model is reported in Fig. 3.8. We used the parameters proposed by [118] for $PbTiO_3$, which are the same as those previously used by Qiu *et al.* [84] and similar to those of Pertsev et al. [95]. The phase diagram was built by minimizing the LGD potential for fixed values of σ_{33}. The LGD results are in agreement with our first-principles calculations, reproducing a FE_x ground state under compressive stress and a FE_z ground state under tensile stress. The phase diagram of $PbTiO_3$ under uniaxial stress is qualitatively distinct from the one reported in thin films under biaxial strain [95, 111]. It nevertheless highlights the possibility of a stress engineering of the ferroelectric properties similar to that achieved by strain [48, 49]. The uniaxial stress both increases the saturated polarization and linearly shifts the phase-transition temperature T_c to higher temperatures. The effect is particularly strong under tensile stress in the FE_z phase where a stress of 1 GPa produces a T_c shift of $\sim$ 300 K. We notice also that the ferroelectric phase transition tends to acquire a second-order character under tensile strain; this result is reminiscent of the observation that hydrostatic pressure also enhances the second-order character of phase transitions in ferroelectrics [38].

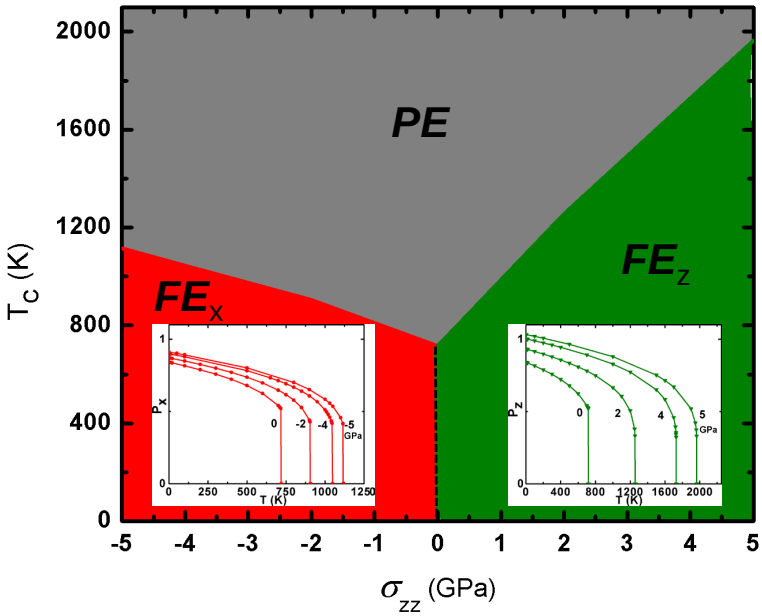

Figure 3.8: Phase diagram of $PbTiO_3$ under uniaxial stress σ_{zz}, as predicted from LGD theory.

In Fig. 3.9, we report the evolution of the spontaneous polarization P_s of $PbTiO_3$ as a function of the applied uniaxial stress. Although first-principles and LGD calculations

nicely agree over a wide range of compressive stress, they only coincide in the limit of small tensile stress. The first-principles calculations reveal an abrupt jump in P_s at a critical tensile stress $\sigma^c_{zz} \approx 2$ GPa that is not captured in the LGD model. This jump in the polarization of the FE_z phase under tensile stress was previously highlighted by Duan *et al.* [61]. We see that a similar behavior also appears in the FE_x phase under compression, but at a much larger critical stress ($\sigma^c_{zz} \approx -8$ GPa). These jumps in polarization are also accompanied by a change in the elastic constant, as observed in the stress versus strain curve (inset of Fig. 3.7).

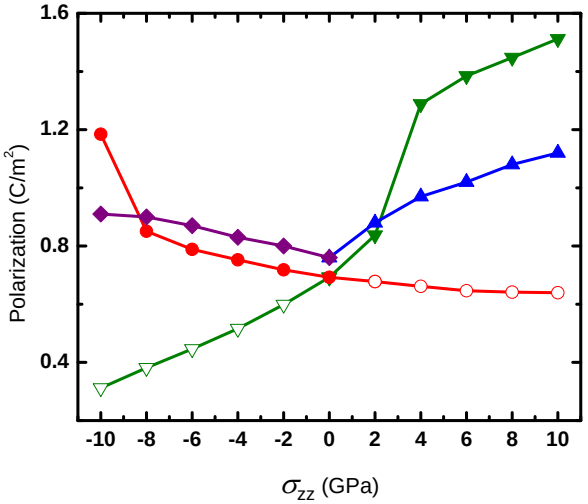

Figure 3.9: (Color Online) Evolution of the polarization of the FE_x (red circles) and FE_z (green downward triangles) phases of $PbTiO_3$ with the uniaxial stress, as predicted within the LDA. Solid symbols correspond to the region where the phase is the ground state. Purple diamonds and blue upward triangles correspond to the prediction from LGD theory at 300 K [120] for the FE_x phase and FE_z phases, respectively.

As illustrated in Fig. 3.10, the sudden increase in P_s is linked to a dramatic jump in the c parameter and is accompanied by a strong increase in the ionic distortions. This is only partly compensated by a small decrease in the Born effective charges. This behavior (including the evolution of the atomic distortions) is totally comparable to what was previously reported for $PbTiO_3$ under isotropic negative pressure by Tinte *et al.* [119]. They explained that behavior by the proximity of a phase transition, the microscopic origin of which could be the breaking of one of the Ti–O bonds along the polar axis.

Here, this behavior appears, however, at a smaller critical tensile stress. Moreover, it is also predicted under compressive stress. While negative isotropic pressure is something not practically accessible experimentally, uniaxial stresses (both tensile or compressive) were recently made accessible to laboratory-on-a-chip experiments [121–123]. This experiment could offer the possibility to confirm our prediction experimentally. Moreover, it could also reveal to be of concrete practical interest: as highlighted by Duan *et al.* [61], in the vicinity of the critical stress, $PbTiO_3$ will exhibit a large piezoelectric response , i.e., $d_{zzz} = \partial P_z/\partial\sigma_{zz}$ ($d_{xzz} = \partial P_x/\partial\sigma_{zz}$), that is proportional to the slope of P in Fig. 3.9 that might be directly exploited to enlarge the piezoelectric sensitivity of nanodevices.

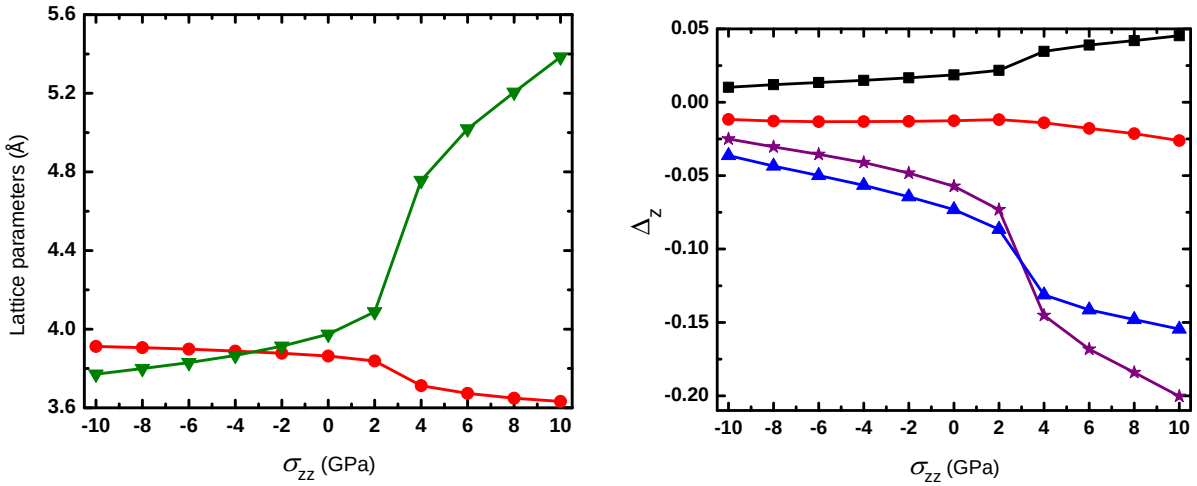

(a)

(b)

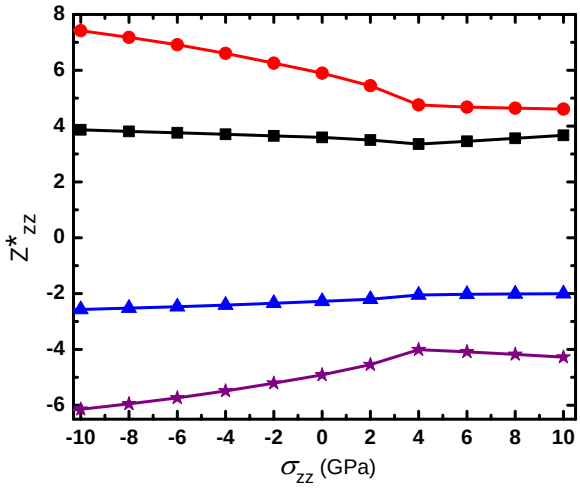

(c)

Figure 3.10: Evolution of (a) the c (green triangles) and a (red circles) lattice parameters (Å), (b) atomic displacements, and (c) Born effective charges as a function of uniaxial stress in the FE_z phase of $PbTiO_3$ as calculated within the LDA. In (b) and (c) black squares are for Pb, red circles are for Ti, purple stars for O_1, and blue triangles are for $O_{2,3}$.

Phase	Unit cell			Energy	Distortion
	a	b	c	ΔE	angle (deg) or P_s
	(Å)	(Å)	(Å)	(meV/f.u.)	($\mu C/cm^2$)
$Pm\bar{3}m$	3.880	3.880	3.880	0	–
($a^0a^0a^0$)	(3.935)	(3.935)	(3.935)	(0)	–
Exp.[114]	3.93	3.93	3.93	–	–
$P4mm$	3.863	3.863	3.975	-36.70	$P_s = 70$
($a^0a^0c^0_P$)	(3.880)	(3.880)	(4.243)	(-83.27)	($P_s = 97$)
Exp.[124]	3.880	3.880	4.155	–	$P_s = 75$
$Amm2$	3.912	3.912	3.865	-31.60	$P_s = 63$
($a^0_Pa^0_Pc^0$)	(3.999)	(3.999)	(3.901)	(-62.90)	($P_s = 75$)
$R3m$	3.895	3.895	3.895	-30.02	$P_s = 62$
($a^0_Pa^0_Pa^0_P$)	(3.962)	(3.962)	(3.962)	(-58.25)	($P_s = 71$)
$P4/mbm$	5.477	5.477	7.783	-3.20	$\phi^+ = 4.13$
($a^0a^0c^+$)	(5.558)	(5.558)	(7.880)	(-1.06)	($\phi^+ = 3.09$)
$I4/mcm$	5.470	5.470	7.797	-10.80	$\phi^- = 5.62$
($a^0a^0c^-$)	(5.552)	(5.552)	(7.891)	(-5.00)	($\phi^- = 4.60$)
$Imma$	5.480	5.505	7.732	-12.01	$\phi^- = 4.15$
($a^-a^-c^0$)	(5.559)	(5.576)	(7.850)	(-5.59)	($\phi^- = 3.43$)
$R\bar{3}c$	7.756	7.756	7.756	-12.00	$\phi^- = 3.36$
($a^-a^-a^-$)	(7.866)	(7.866)	(7.866)	(-5.29)	($\phi^- = 2.7$)

Table 3.1: Cell parameters, internal energies, and distortion amplitudes of different metastable phases of $PbTiO_3$ fully relaxed within the LDA and the GGA-WC (values in parentheses). For each phase, we specify the space group and, in parentheses, the compatible FE and AFD structural distortion using generalized Glazer's notation (see Technical details section). The amplitudes of the spontaneous polarization (P_s) and of the oxygen octahedra rotation angle (ϕ) are reported when appropriate. For the $Pm\bar{3}m$ and $P4mm$ phases, the experimental parameters (Exp.) are reported for comparison.

3.6 Chapter summary

In this chapter, the behavior of $PbTiO_3$ under uniaxial strains and stresses has been explored from first-principles calculations and LGD theory. Under uniaxial strain, $PbTiO_3$ adopts a purely ferroelectric FE_x ground state under compressive strain and switches to a purely ferroelectric FE_z ground state under tensile strain larger than $\eta^c_{zz} \approx 1\%$. This behavior is in contrast to the emergence of phases combining FE and AFD distortion under biaxial strain and isotropic pressure. The situation might be different in the vicinity of surfaces that promote AFD distortions and therefore in ultrathin films [112]. Under uniaxial stress, $PbTiO_3$ exhibits either a FE_x ground state under compression or a FE_z ground state under tension. Moreover, our calculations highlight an abrupt jump in the structural parameters under both compressive and tensile stresses at the critical values $\sigma_{zz} \approx +2$ GPa and -8 GPa. While LGD theory reproduces nicely the first-principles data, it does not capture this strong relaxation and so remains only valid in a region between the critical stresses. The jump in the structural parameters is linked to a strong increase in the piezoelectric response, which might potentially be exploited.

Chapter 3: Study of $PbTiO_3$ under uniaxial strains and stresses

Chapter 4

Theoretical study of $SrTiO_3$ under uniaxial, biaxial and isotropic mechanical strains

The aim of this Chapter is to study the mechanical constraint effect on $SrTiO_3$. In the first section, we study the effect of uniaxial strain on the FE and AFD instabilities of $SrTiO_3$, which is compared to the case of isotropic and biaxial strains. The phase diagram in terms of uniaxial, biaxial and isotropic amplitude and temperature has been studied by LGD phenomenological theory and compared with the first-principles calculations.

4.1 Introduction

Amongst ABO_3 compounds, $SrTiO_3$ has likely attracted the most attention, being simultaneously a prototypical quantum paraelectric [125] and a superconductor under doping at low temperature [126]. At a more applied level, $SrTiO_3$ is a component of $Ba_xSr_{1-x}TiO_3$ solid solutions, which are widely used for tunable dielectric applications [127] and a promising n-type thermoelectric oxide compound [128]. Nowadays, it is also the most common substrate for epitaxial growth of various type of oxide nanostructures [129–132] and a key ingredient of the $LaAlO_3/SrTiO_3$ interface [56] developing a 2-dimensional electron gas, the properties of which are intimately linked to those of $SrTiO_3$.

Stable at high temperature in the ideal $Pm\bar{3}m$ cubic perovskite structure (see Fig. 4.1), $SrTiO_3$ combines ferroelectric (FE) and antiferrodistortive (AFD) structural instabilities. Under cooling, mechanically free bulk $SrTiO_3$ undergoes a unique cubic-to-tetragonal AFD phase transition at 105 K [13, 134] to a non-polar phase of $I4/mcm$ symmetry. This appears as a typical displacive phase transition resulting from the softening of a phonon mode at the R-point of the cubic Brillouin zone (BZ), associated to the rotation of the oxygen octahedra [28]. At the same time, $SrTiO_3$ exhibits a progressive softening of a zone-center polar phonon mode, yielding a progressive divergence of its dielectric properties when temperature is lowered and that should produce a ferroelectric phase transition at very low-temperature. The latter is nevertheless suppressed by quantum fluctuations [135], making of $SrTiO_3$ a prototypical "quantum paraelectric" [125].

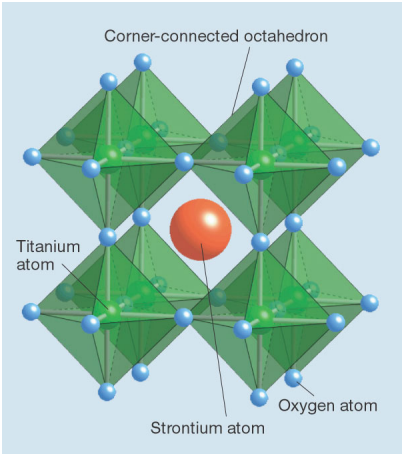

Figure 4.1: The crystal structure of $SrTiO_3$ [133]. Each titanium atom is bonded to six oxygen atoms, forming an octahedral structure.

Previous studies provided insight into the evolution of the structural properties of epitaxial $SrTiO_3$ thin films with temperature and epitaxial strain amplitude. It was demonstrated experimentally that $SrTiO_3$ can be made ferroelectric at room temperature under appropriate biaxial strain [49, 136], in agreement with Landau-Ginzburg-Devonshire theory [49] and first-principles calculations [50, 137, 138] restricted to the consideration of FE degrees of freedom. The tunability of the dielectric constant under epitaxial strain was also studied theoretically [139]. Using a more complete LGD model including explicitly AFD motions, Pertsev *et al.* [51] then predicted a rich temperature–biaxial strain phase diagram, highlighting phases combining FE and AFD distortions, a result further confirmed

at the first-principles level [140]. The behavior of $SrTiO_3$ under hydrostatic pressure has also been explored, highlighting a linear increase of the cubic to tetragonal AFD phase transition temperature up to room temperature or even above at high pressure [141]. Pressure dependence of the elastic constants of $SrTiO_3$ under hydrostatic pressure was also explored in the past [142]. Recently, high-pressure phase transition studies has also been performed in $SrTiO_3$ [143].

Although, there have been various investigations of the behavior of $SrTiO_3$ under biaxial and isotropic strains, we are not aware of much previous studies regarding the effect of uniaxial mechanical constraints. However in the past some work have been done under uniaxial stresses [144, 145] and uniaxial strain [146]. In this work, we have extended our previous investigations on $PbTiO_3$ by exploring theoretically the effect of uniaxial strains on the properties of perovskite $SrTiO_3$, by combining first-principles calculations and phenomenological Landau-Ginzburg-Devonshire (LGD) model. For comparison, we also report results concerning the role of isotropic and biaxial strains. At first, we study the cubic phase of $SrTiO_3$, identify the most relevant phonon instabilities and discuss their evolution with strain using first-principles DFT calculations. Then, we determine the phase diagram of $SrTiO_3$ in terms of temperature and strain using LGD theory and discuss how these results compare with first-principles calculations and available experimental data.

4.2 Technical Details

The calculations details for FP and LGD are described in Chapter 2, in the technical details section. The Landau-Ginzburg-Devonshire (LGD) calculations have been performed following the scheme and using parameters provided in Ref. [51].

In what follows, we consider that the x, y and z cartesian axis are aligned respectively with the cell vectors a, b and c of the reference cubic structure. Then, the uniaxial constraint is always applied along the z-direction. To label the ferroelectric and antiferrodistortive motions compatible with a given space group, we use "generalized" Glazer's notations in which the superscripts refer as usual to the rotation pattern and a subscript P is added to identify the direction(s) along which a polarization can develop.

4.3 Bulk structure

First, we reinvestigate the highly-symmetric cubic perovskite structure of $SrTiO_3$. In this cubic phase, the atomic positions are fixed by symmetry and the only structural parameter to be relaxed is the lattice constant a_0. Our relaxed lattice constants $a_0^{LDA} = 3.846$ Å and $a_0^{GGA} = 3.906$ Å are comparable to previous calculations ($a_0^{LDA} = 3.84$ Å [109]) and in satisfactory agreement with experimental data ($a_0^{EXP} = 3.905$ Å [147]). As expected, the LDA tends to underestimate the experimental lattice constant that is nearly exactly reproduced at the GGA-WC level.

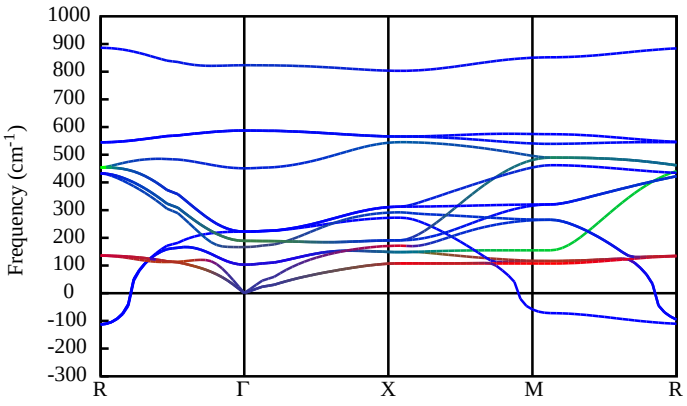

(a)

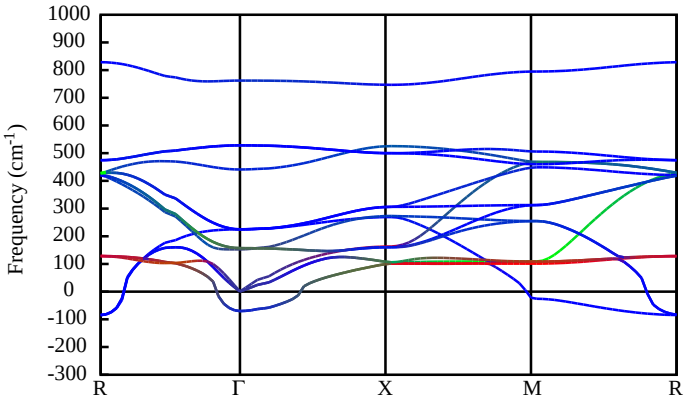

(b)

Figure 4.2: Calculated phonon dispersion curves of cubic $SrTiO_3$, at the LDA volume (panel a) and at the GGA-WC volume (panel b) along the path R–Γ–X–M–R of the Brillouin zone.

The phonon dispersion curves of cubic $SrTiO_3$ calculated within the LDA and GGA-WC (at the optimized volume corresponding to each functional) are shown in Fig. 4.2. They significantly differ from each other, although agreeing each with the previous literature [109]. At the LDA level, we observe a single unstable phonon branch dominated by a R^{4+} instability at a frequency of 125i cm^{-1}. This mode corresponds to antiferrodistortive (AFD) motions associated to rotations of the oxygen octahedra, with consecutive octahedra along the rotation axis moving anti-phase (a^- in Glazer's notations). This instability then propagates all the way from R to M, connecting to an unstable M^{3+} mode at a frequency of 71i cm^{-1} which is associate to rotation of the oxygen octahedra with consecutive octahedra moving in-phase (a^+ in Glazer's notations). At the GGA-WC level, we still observe a similar branch of AFD unstable modes, although with a reduced amplitude of the instabilities, (R^{4+} mode at 84i cm^{-1} and M^{3+} mode at 25i cm^{-1}). Additionally, we now observe the appearance of a ferroelectric (FE) instability associated to a Γ^{4-} (F_{1u}) mode at a frequency of 70i cm^{-1} (stable at 102 cm^{-1} in LDA) and corresponding to a polar displacement of cations against the oxygen. This instability remains confined in a small volume of the Brillouin zone around the Γ point.

The difference between LDA and GGA-WC results can be assigned to their distinct relaxed volumes: contrary to the GGA-WC, the LDA underestimates the experimental lattice constant. This volume contraction, as usual in perovskites, suppresses the FE instability and amplifies the AFD instability. Our GGA-WC results closely resemble those obtained in the early calculation of LaSota *et al.* [148] within the LDA but at the experimental volume and highlight the incipient character of ferroelectricity in $SrTiO_3$.

Since they predict distinct structural instabilities at the cubic level, we now investigate to which extent LDA and GGA-WC functionals both reproduce the correct ground state. In Table 4.1, we report the energy and structural parameters of different metastable phases resulting from the condensation of (i) different combinations of AFD modes at R and M points and, at the GGA-WC level, (ii) the additional FE instability at the Γ point. Within the LDA, the largest gain of energy is obtained for the $I4/mcm$ symmetry compatible with the ($a^0a^0c^-$) oxygen tilt pattern, consistently with the experimental ground state. We observe that the a^+ rotation pattern always produces a much lower gain of energy. In line with this, we notice that atomic relaxations in the $Cmcm$ ($a^0b^+c^-$) and $Pbnm$ ($a^-a^-c^+$) symmetries relax back to the $I4/mcm$ and $Imma$ phases respectively, attesting

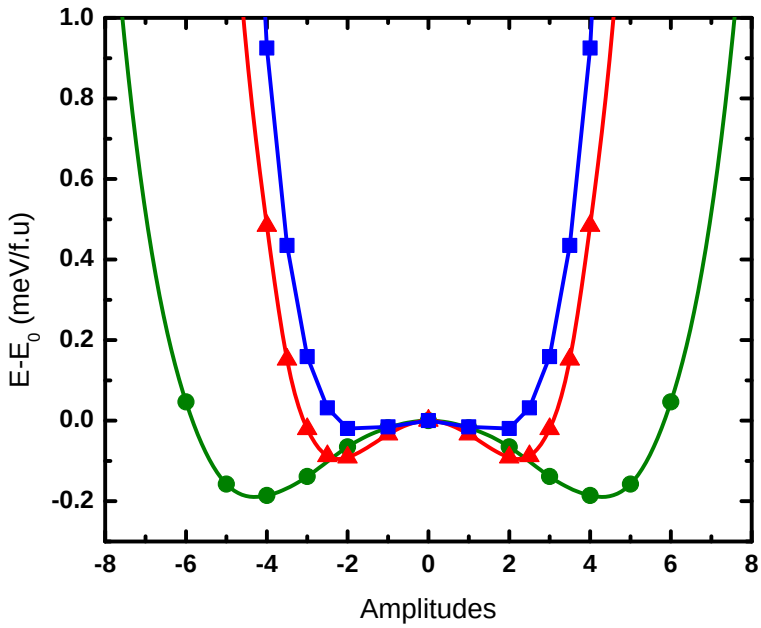

Figure 4.3: Double-wells of (I4/mcm) phase of $SrTiO_3$ at GGA volume. The green solid circles indicates $Ima2$ phase, red solid triangles indicates $Fmm2$ phase and blue solid squares indicates $I4cm$ phase.

Phase		Unit cell		Energy	Distortion
	a	b	c	ΔE	angle (deg) or P_s
	(Å)	(Å)	(Å)	(meV/f.u.)	(μC/cm^2)
$a^0a^0a^0$	3.846	3.846	3.846	0	–
$Pm\bar{3}m$	(3.906)	(3.906)	(3.906)	(0)	–
Exp.[147]	3.905	3.905	3.905	–	–
$a^0a^0c^0_P$	–	–	–	–	–
$P4mm$	(3.903)	(3.903)	(3.917)	(-0.57)	($P_s = 17.46$)
$a^0_Pa^0_Pc^0$	–	–	–	–	–
$Amm2$	(3.911)	(3.911)	(3.902)	(-0.59)	($P_s = 19.55$)
$a^0_Pa^0_Pa^0_P$	–	–	–	–	–
$R3m$	(3.908)	(3.908)	(3.908)	(-0.55)	($P_s = 20.08$)
$a^0a^0c^+$	5.423	5.423	7.719	-4.48	$c^+ = 4.91$
$P4/mbm$	(5.522)	(5.522)	(7.812)	(0.18)	($c^+ = 1.08$)
$a^0a^0c^-$	5.409	5.409	7.739	-23.02	$c^- = 7.17$
I4 $/mcm$	(5.507)	(5.507)	(7.840)	(-8.13)	($c^- = 5.65$)
Exp.[149]	5.507	5.507	7.796	–	($c^- = 2.01$)
$a^-a^-c^0$	5.426	5.455	7.657	-21.15	$a^- = 4.81$
$Imma$	(5.516)	(5.533)	(7.790)	(-7.41)	($a^- = 3.78$)
$R\bar{3}c$	7.681	7.681	7.681	-20.32	a^- =3.82
($a^-a^-a^-$)	(7.806)	(7.806)	(7.806)	(-7.18)	(a^- =3.01)
$a^0_Pa^0_Pc^-$	–	–	–	–	–
$Ima2$	(5.511)	(5.515)	(7.833)	(-8.48)	($P_s = 17$)
					($c^- = 5.49$)
$a^-_Pa^-_Pc^-$	–	–	–	–	–
Cc	(5.510)	(5.513)	(7.839)	(-8.51)	($P_s = 16$)
					($a^- = 0.65$)
					($c^- = 4.77$)

Table 4.1: Cell parameters, internal energies, and distortion amplitudes of different metastable phases of $SrTiO_3$ fully relaxed within the LDA and the GGA-WC (values in parentheses). For each phase, we specify the space group and, in parentheses, the compatible FE and AFD structural distortion using generalized Glazer's notations (see Technical details section). The amplitudes of the spontaneous polarization (P_s) and of the oxygen octahedra rotation angle (ϕ) are reported when appropriate.

that the appearance of the a^- rotation suppresses the instability associated to a^+ motions. Within the GGA-WC we observe the same trend as for the LDA, although with typically lower gains of energy. In this case, the FE distortion is unstable but, in comparison to the AFD motions, it produces significantly lower energy gains. This ferroelectric instability is nevertheless not suppressed by the AFD motions and the $I4/mcm$ phase presents phonon zone-center instabilities associated to FE distortions polarized along x, y and z at frequencies of 70i cm^{-1}, 70i cm^{-1} 66i cm^{-1}. Condensing into the $I4/mcm$ phase the unstable FE motion polarized along x, xy and z lowers the symmetry of the system to $Fmm2$, $Ima2$ and $I4cm$ respectively and yield the double wells shown in Fig. 4.3. The largest gain of energy is associated to a polar distortion along the xy direction. Fully relaxing the associated $Ima2$ phase ($a^0_P a^0_P c^-$), the gain of energy is of -8.48 meV/f.u, with a polarization $P_s = -0.17$ C/m^2. Recomputing the phonons in this $Ima2$ phase, we found again one unstable mode at a frequency of 29i cm^{-1}, including a complex interplay between oxygen motions and polar motions of Ti along z and anti-polar motions of Sr along xy. Condensing this mode, the symmetry is lowered to Cc. Fully relaxing within the Cc space group, the final gain of energy is of -8.51 meV/f.u. Within this relaxed Cc phase, we did not identified any phonon instability. At the GGA-WC level, the ground state is therefore no more the $I4/mcm$ phase but an unexpected Cc phase. The difference of energy between the $I4/mcm$ and Cc phases is however very tiny and beyond the expected accuracy of our calculations. This result highlights the incipient ferroelectric character of $SrTiO_3$ and is compatible with its quantum paraelectric character.

In order to anticipate how the ground state of $SrTiO_3$ can be affected by mechanical constraints, we now analyze how the amplitude of the most relevant FE instabilities at Γ and AFD instabilities at R of the reference paraelectric structure are evolving under uniaxial strains. For comparison, we did the same investigation for biaxial and isotropic strains.

Under isotropic strain, the paraelectric reference remains cubic and we can directly follow the strain evolution of the Γ^{4-} and R^{4+} modes. Applying a uniaxial strain along the z axis or a biaxial strain along the x and y axis, the $Pm\bar{3}m$ structure becomes tetragonal ($P4/mmm$ symmetry). This splits the triply degenerated Γ^{4-} (F_{1u}) FE mode into a single Γ^{3-} (A_1) mode and a doubly degenerated Γ^{5-} (E) mode, polarized respectively along c-axis and perpendicularly to it. Similarly the triply degenerated R^{4+} AFD mode is split into a

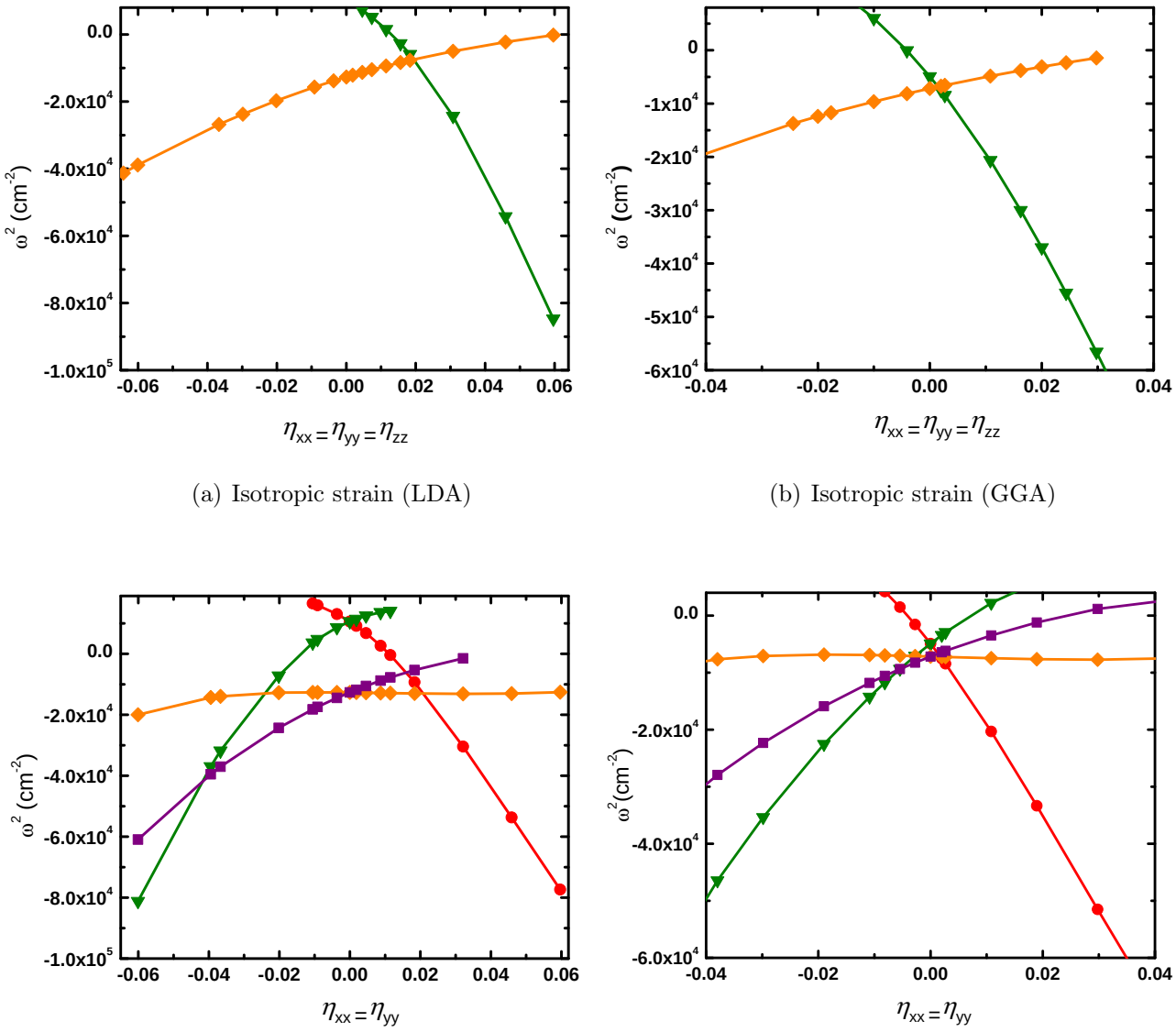

(a) Isotropic strain (LDA)

(b) Isotropic strain (GGA)

(c) Biaxial strain (LDA)

(d) Biaxial strain (GGA)

Figure 4.4: Evolution of the square of the frequency of the FE and AFD modes under isotropic and biaxial in the paraelectric $P4/mmm$ phase of $SrTiO_3$, as obtained within the LDA and GGA-WC volume. Here, Γ^{3-} (green triangles) and Γ^{5-} (red circles) and of the AFD modes A_3^+ (purple squares) and A_5^+ (orange diamonds) for (panel c and d). For triply degenerate FE modes, Γ^{5-} or Γ^{3-} is indicated in (green triangles) and triply degenerate AFD modes A_3^+ or A_5^+, in (orange diamonds) (panel a and b).

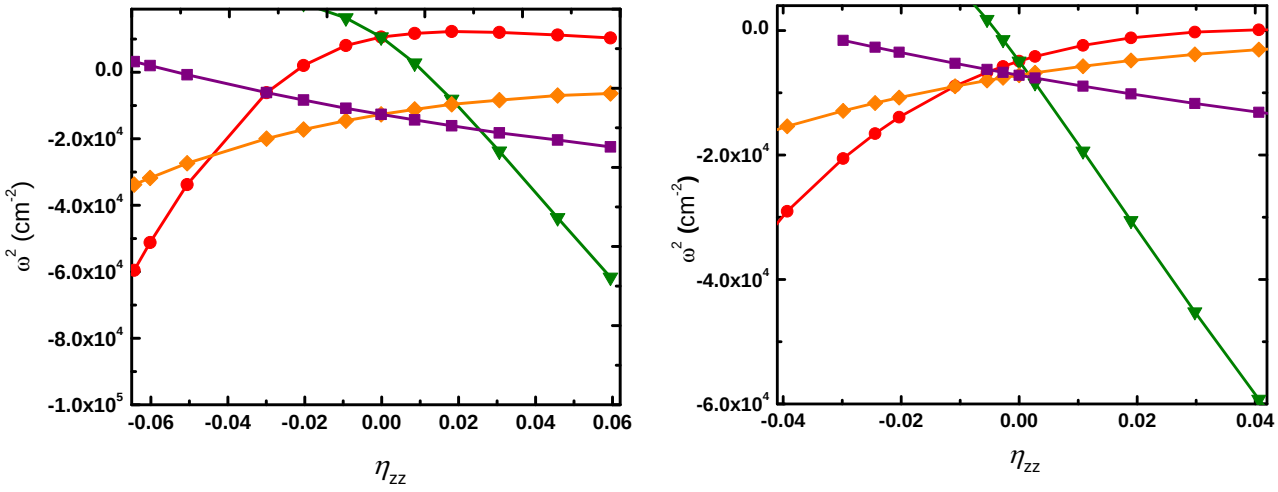

(e) Uniaxial strain (LDA) (f) Uniaxial strain (GGA)

Figure 4.4: Evolution of the square of the frequency of the FE and AFD modes under uniaxial strains in the paraelectric $P4/mmm$ phase of $SrTiO_3$, as obtained within the LDA and GGA-WC volume. Here, Γ^{3-} (green triangles) and Γ^{5-} (red circles) and of the AFD modes A_3^+ (purple squares) and A_5^+ (orange diamonds) for (panel e and f).

single A_z mode and a doubly degenerated A mode, corresponding respectively to oxygen rotations about the z-axis or about the x or y axis for the uniaxial strain and the vice-versa for the biaxial strain. The evolution of the frequencies of these modes with isotropic, biaxial and uniaxial strains are reported in Fig. 4.4 at both LDA and GGA volume.

Although the AFD instability dominates at the bulk level, the situation can strongly evolve with strain. As general rules, (i) FE and AFD instabilities are oppositely affected by strain and (ii) the FE instability is more affected than the AFD one. For the isotropic case, the FE mode (triply degenerate) is strongly destabilized under tensile strains and AFD mode (triply degenerate) under compression. Under biaxial strain, the Γ^{5-} (resp. Γ^{3-}) mode is strongly destabilized under tension (resp. compression), becoming the dominant instability at large strains. Under uniaxial strain, the situation is very similar except that Γ^{5-} (resp. Γ^{3-}) mode is now destabilized under compression (resp. tension). LDA and GGA-WC reproduce globally the same trends. These results highlight that, similarly to what has been made under biaxial strain, uniaxial strain can switch the hierarchy between AFD and FE instabilities and likely make $SrTiO_3$ ferroelectric.

4.4 Uniaxial strain

In this section, we discuss the behavior of $SrTiO_3$ under uniaxial strains, investigated combining first-principles calculations within density functional theory and Landau-Ginzburg-Devonshire phenomenological theory. We also discuss about the phase diagram of $SrTiO_3$ under isotropic and biaxial strain effect within LGD theory.

4.4.1 LGD theory

In order to access the phase diagrams of $SrTiO_3$ in terms of different types of strain and temperature, we switch now to a phenomenological description within LGD theory. In view of the previous discussion, we adopted a model including explicitly FE (polarization amplitudes P_i), AFD (a^- rotation amplitudes q_i) and strain (S_i) degrees of freedom, as previously proposed by Pertsev *et al.* [51]. In this framework, the Helmholtz free energy

density F in terms of P_i, q_i and S_i is written as:

$$\begin{aligned}
F &= \alpha_1 (P_1^2 + P_2^2 + P_3^2) + \alpha_{11} (P_1^4 + P_2^4 + P_3^4) + \alpha_{12} (P_1^2 P_2^2 + P_2^2 P_3^2 + P_1^2 P_3^2) \\
&+ \beta_1 (q_1^2 + q_2^2 + q_3^2) + \beta_{11} (q_1^4 + q_2^4 + q_3^4) + \beta_{12} (q_1^2 q_2^2 + q_2^2 q_3^2 + q_1^2 q_3^2) \\
&+ \tfrac{1}{2} c_{11} (S_1^2 + S_2^2 + S_3^2) + c_{12} (S_1 S_2 + S_2 S_3 + S_1 S_3) + \tfrac{1}{2} c_{44} (S_4^2 + S_5^2 + S_6^2) \\
&- g_{11} (S_1 P_1^2 + S_2 P_2^2 + S_3 P_3^2) - g_{12} (S_1 (P_2^2 + P_3^2) + S_2 (P_1^2 + P_3^2) + S_3 (P_1^2 + P_2^2)) \\
&- g_{44} (S_4 P_2 P_3 + S_5 P_1 P_3 + S_6 P_1 P_2) - \lambda_{11} (S_1 q_1^2 + S_2 q_2^2 + S_3 q_3^2) \\
&- \lambda_{12} (S_1 (q_2^2 + q_3^2) + S_2 (q_1^2 + q_3^2) + S_3 (q_1^2 + q_2^2)) - \lambda_{44} (S_4 q_2 q_3 + S_5 q_1 q_3 + S_6 q_1 q_2) \\
&- t_{11} (P_1 q_1^2 + P_2 q_2^2 + P_3 q_3^2) - t_{12} (P_1 (q_2^2 + q_3^2) + P_2 (q_1^2 + q_3^2) + P_3 (q_1^2 + q_2^2)) \\
&- t_{44} (P_1 P_2 q_1 q_2 + P_2 P_3 q_2 q_3 + P_1 P_3 q_1 q_3),
\end{aligned} \tag{4.4.1}$$

where α_i and β_i are the coefficients of the FE and AFD energy wells, c_{nl} are the elastic stiffnesses, g_{nl} are the electrostrictive constants, λ_{nl} describe the coupling between the strain and AFD oxygen motions and t_{nl} define the interaction between the polarization and AFD oxygen motions. As usual in such phenomenological approach, all these parameters are considered as constant except for α_1 and β_1 given by:

$$\begin{aligned}
\alpha_1 &= 4.5 \left[\coth(54/T) - \coth(54/30)\right] 10^{-3} \\
\beta_1 &= 1.32 \left[\coth(145/T) - \coth(145/105)\right] 10^{26}
\end{aligned}$$

The phase diagrams are then built by identifying the configuration of parameters that minimizes F at each temperature under some fixed mechanical constraints.

In case of fixed *isotropic* strains, we assume that $S_1 = S_2 = S_3$. Then shear strains were also fixed to zero, although we explicitly checked that relaxing them is not playing any significant role. This corresponds to

$$\begin{aligned}
S_1 = S_2 = S_3 = S_m = \frac{a^* - a_0}{a_0} \\
S_4 = S_5 = S_6 = 0.
\end{aligned}$$

The phase diagram is reported and in Fig. 4.5 (a). It is consistent with the evolution of the phonon frequencies previously discussed, highlighting a purely FE ground state under tension and a purely AFD ground state under compression.

In the case of fixed *biaxial* strains imposed in the x and y directions, mimicking the epitaxial strain imposed to thin films by a cubic substrate (fixing S_1, S_2 and S_6), we have mixed

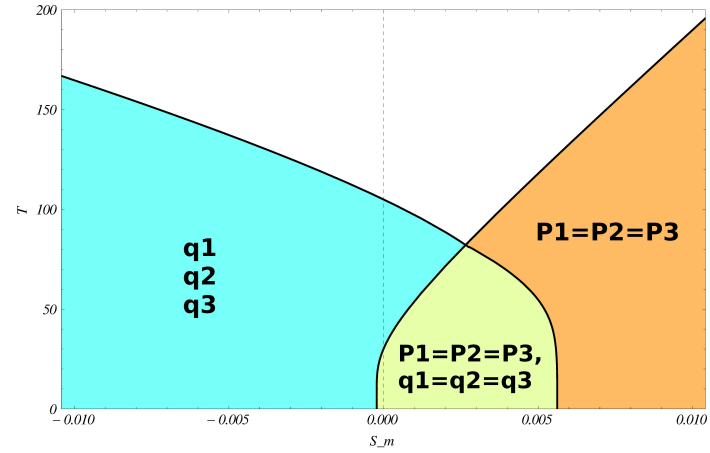

(a)

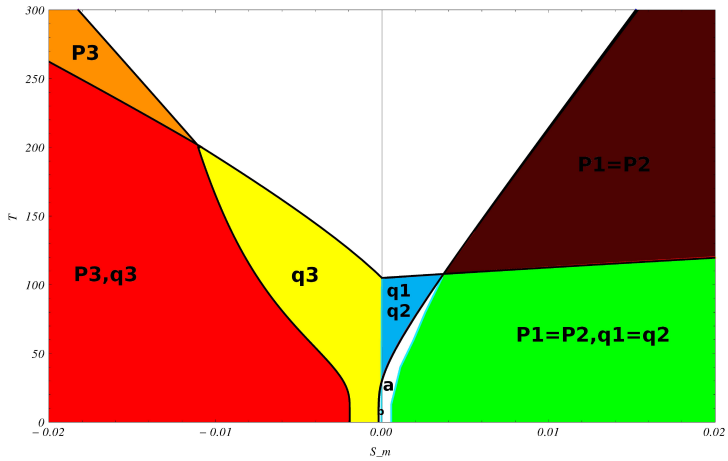

(b)

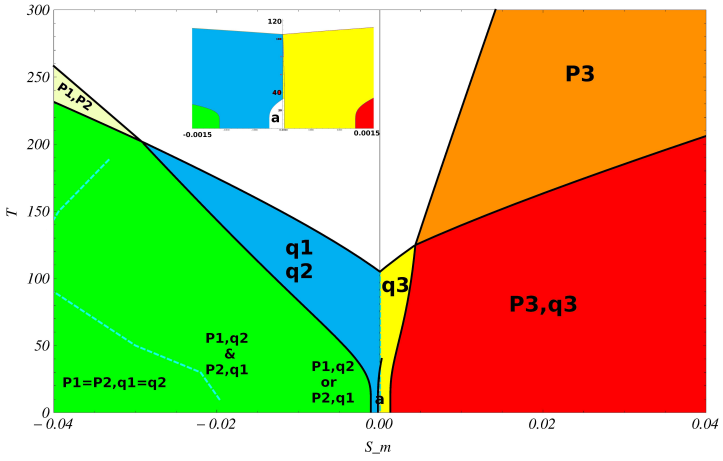

(c)

Figure 4.5: Phase diagram of $SrTiO_3$ under isotropic (panel a), biaxial (panel b) and uniaxial strains (panel c) using LGD theory.

mechanical boundary conditions corresponding to:

$$S_1 = S_2 = S_m = \frac{a^* - a_0}{a_0}, S_6 = 0$$
$$\frac{\delta F}{\delta S_3} = \frac{\delta F}{\delta S_4} = \frac{\delta F}{\delta S_5} = 0.$$

In our calculations, we neglect the possible appearance of a depolarizing field along z, which corresponds to the case a relatively thick film between metallic electrodes in short-circuit. The phase diagram reported in Fig. 4.5 (b) corresponds to that previously reported by Pertsev *et al.* [51]. At small strains, different AFD tilt patterns can be observed while FE distortion appears at increasing strains. It confirms that $SrTiO_3$ can be made FE at room temperature under both moderate tensile and compressive epitaxial strains. This is again consistent with the fact that FE phonon instabilities become dominant as strain increases. As highlighted in the previous section, large biaxial strains do however not suppress all AFD instabilities so that phases combining FE and AFD distortions are observed at lower temperature.

In case of fixed *uniaxial* strain applied along one axis, only one component of strain is fixed while all other strain components are free to relax:

$$S_1 = S_m = \frac{a^* - a_0}{a_0}$$
$$\frac{\delta F}{\delta S_2} = \frac{\delta F}{\delta S_3} = \frac{\delta F}{\delta S_4} = \frac{\delta F}{\delta S_5} = \frac{\delta F}{\delta S_6} = 0.$$

The phase diagram obtained under uniaxial strain is reported in Fig. 4.5 (c). It present close similarities with that observed under biaxial strains, the phases stabilized under compression being now observed under tension and *vice versa*. We observe that a very moderate tensile uniaxial strain can make $SrTiO_3$ ferroelectric at room temperature, while doing so under compression would require a much larger strain. At low temperatures, the system is expected to go through a sequence of many different phase transitions when the strain evolves from +4 to -4%, as also summarized in Fig. 4.6. Under tension, $SrTiO_3$ combines FE and AFD motions along z axis. When the strain is reduced, the FE distortion first disappears. Then under compression, the AFD motion switches from rotations around the z to the x (or y) axis and later, a polarization additionally appears along x. Progressively when compressive strains continue to increase, FE and AFD motions rotates from x to xy direction. Some of these phases are stable in a very narrow range of strains.

4.4.2 First-principles calculations

LGD theory predicts a rich and complex phase diagram for $SrTiO_3$ under uniaxial strain. It is interesting to check how the sequence of phase transition expected at low temperature is validated by first-principles calculations at the LDA and GGA-WC levels. To that end, we have compared the energetics of various different phases at selected strains. The results are summarized in Fig. 4.6. For each strain, we report the ground state identified with each functional. In cases where different phases are very close in energy (difference of energy of the order of 1 meV or lower), all of them are mentioned.

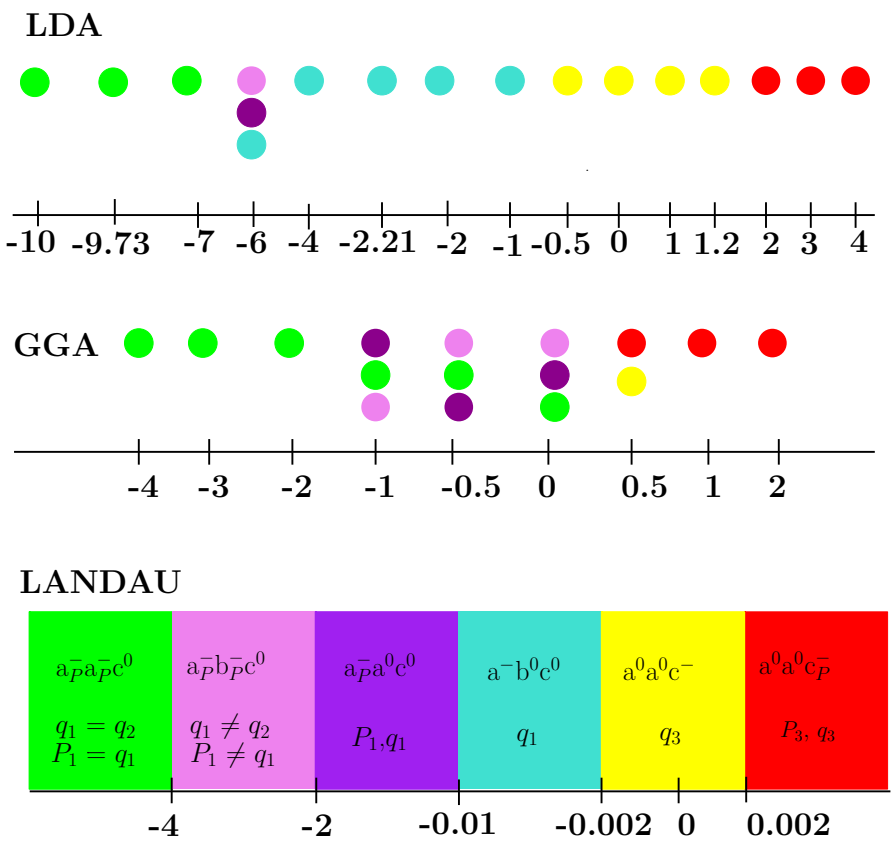

Figure 4.6: Phase diagram of $SrTiO_3$ under uniaxial strain with LDA (panel a), GGA (panel b) and LGD theory (panel c). See Appendix A for the uniaxial and compressive strains values under LDA and GGA volume.

The LDA reproduces qualitatively the phase predicted at the Landau level. However, it significantly broadens the range of stability of the $a^-b^0c^0$ and $a^0a^0c^-$ phases. Still, the $a^-_Pa^-_Pc^0$ and $a^0a^0c^-_P$ phases appears under compression and tension respectively but at much larger strains than predicted from Landau theory. This is a direct consequence of the lower volume obtained in LDA that, as previously discussed, tends to suppress the ferroelectric instability.

At the opposite, the GGA-WC calculations tends to broaden the range of stability of the $a^-_Pa^-_Pc^0$ and $a^0a^0c^-_P$ phases. Between the range of stability of these two phases, there is a narrow region in which many phases are in close competition. The difference of energy between those phases is however so small (lower than 1 meV) that it is not possible to unambiguously determine the sequence of phase transition and limits between the different phases. As illustrated in Fig. 4.7, in the strain range of about -1%, a phase with different amplitude of oxygen AFD rotations around the x and y axis can be stabilized, confirming what is predicted at the LGD level. The same is obtained at the LDA level but at much larger strains. Overall, the GGA-WC calculation is therefore in close agreement with the LGD calculations and confirms the main features of the phase diagram obtained at that phenomenological level.

4.5 Chapter summary

In this chapter, we have investigated the role of uniaxial strain on the FE and AFD instabilities of $SrTiO_3$, making explicit comparison with the cases of isotropic and biaxial strains. The phase diagram in terms of uniaxial strain amplitude and temperature has been obtained in the context of LGD phenomenological theory, and confirmed from first-principles calculations. We predict a rich phase diagram, including phases combining FE and AFD motions and presenting some close similarities with that obtained under biaxial strains. In particular, we predict that $SrTiO_3$ could easily be made ferroelectric under moderate uniaxial tensile strains, a feature that we hope, can be further confirmed experimentally.

The LGD calculations have been done in collaboration with Denis Fontaine (University of Liège).

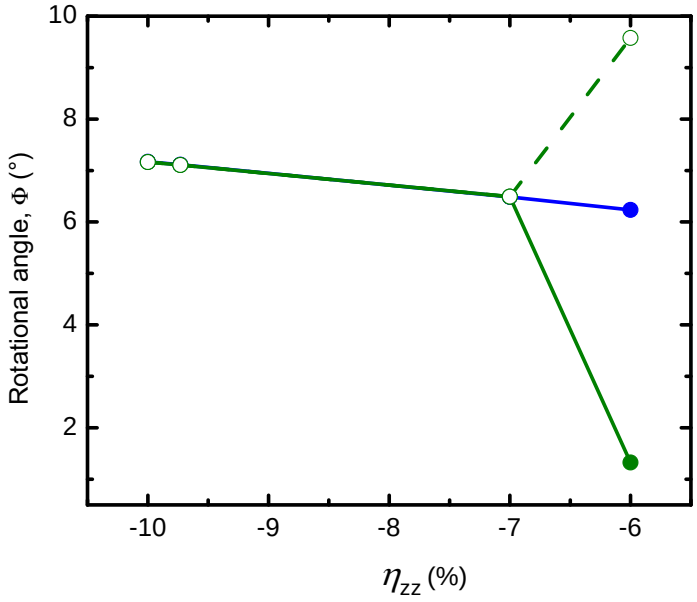

(a)

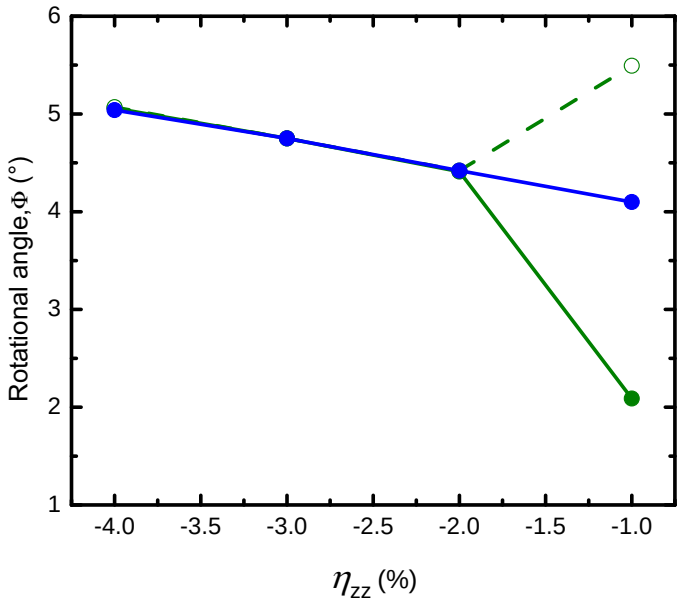

(b)

Figure 4.7: Evolution of rotational angles of $Ima2$ and Cm phase of $SrTiO_3$ with LDA (panel a) and GGA (panel b) under compressive strains. Green solid circles and open circles indicates a^- and b^- rotational angles of Cm phase and blue solid circles indicates a^- angles of $Ima2$ phase.

Chapter 4: Theoretical study of $SrTiO_3$ under uniaxial, biaxial and isotropic mechanical strains

Chapter 5

Conclusion and Perspectives

The goal of this PhD thesis is to study the effect of uniaxial mechanical constraint on $PbTiO_3$ and $SrTiO_3$ from first-principles DFT calculations and phenomenological LGD theory. First-principles electronic structure calculations play an important role in understanding the conceptual framework in constrained geometries. They offer a vital tool for the materials design, characterization and theoretical understanding. Phenomenological LGD theory has gained remarkable success due to its ability to describe the first and second order phase transitions in bulk ferroelectrics, thin films and superlattices. The rapid development in the field of ferroelectrics in the last few years has been exciting and has revealed fascinating physics in condensed matter field. In the past, much progress in understanding ferroelectrics has been achieved in the field of strain engineering under biaxial and hydrostatic pressures, few investigations are known under uniaxial pressure, which has motivated this thesis. Our main results and future perspectives are summarized as follows:

We have studied the behavior of $PbTiO_3$ under uniaxial strains and stresses from first-principles calculations and LGD theory. Under uniaxial strain, we have shown that $PbTiO_3$ adopts a purely ferroelectric FE_x ground state under compressive strain and switches to a purely ferroelectric FE_z ground state under tensile strain larger than $\eta^c_{zz} \approx 1\%$. This contrasts with the emergence of phases combining FE and AFD distortion under biaxial strain [109] and isotropic pressure [90]. Under uniaxial stress, $PbTiO_3$ exhibits either a FE_x ground state under compression or a FE_z ground state under tension. Moreover, our calculations highlight an abrupt jump of the structural parameters under both compressive

and tensile stresses at critical values $\sigma_{zz} \approx +2$ GPa and -8 GPa and this jump of the structural parameters will be linked to a strong increase of the piezoelectric response. The evolution of FE and AFD instabilities with uniaxial strains shows the dominating behavior of FE instability of purely ferroelectric $PbTiO_3$. The evolution of polarization with strain and stress clearly shows that at bulk level the polarization always prefers to stay aligned with one of the pseudocubic axis (z or x) and that the FE_{xy} phase is never the most stable configuration. The phase diagram obtained by the LGD theory is interesting as it can predict the first-principles data, however it does not capture this strong relaxation and so remains only valid in a region between the critical stresses. We have performed all the first-principles calculations with both LDA and GGA-WC approach and our results are consistent with each other. We hope that our work will motivate further experimental characterization of $PbTiO_3$ under uniaxial tensile and compressive stresses.

We have then extended our investigations on $PbTiO_3$ by exploring theoretically the pressure effects on the perovskite $SrTiO_3$ by combining first-principles calculations and the phenomenological Landau model. We have investigated the role of uniaxial strain on the FE and AFD instabilities of $SrTiO_3$, making explicit comparison with the cases of isotropic and biaxial strains. We have performed the calculations using both LDA and GGA-WC approach. Both results are consistent with each other. The phase diagram in terms of uniaxial strain amplitude and temperature has been obtained in the context of LGD phenomenological theory, and confirmed from first-principles calculations. We predict a rich phase diagram, including phases combining FE and AFD motions and presenting some close similarities with that obtained under biaxial strains. We have also calculated the phase diagram of $SrTiO_3$ under uniaxial strain, as obtained from Landau theory as well as first-principles calculations. At the bulk level, we observe that uniaxial strain has a much larger effect on the ferroelectric instability than on the antiferrodistortive oxygen motions, suggesting a progressive evolution from an antiferrodistorted to a ferroelectric ground-state under increasing strains. The evolvement of different phases under uniaxial compressive strains within LDA or GGA-WC and also LGD theory are consistent.

Many of the interesting results shown on $PbTiO_3$ and $SrTiO_3$ are still waiting for experimental verification. Recently a lot of attention has been devoted to multiferroic materials that exhibit both electric and magnetic properties embedded together in the same crystal, and this is motivated by the strong desire of controlling the magnetization by an electric

field (magnetoelectric response) and vice versa. Materials having this property would be of very high potential for technological applications such as spintronics or computer information. However, multiferroic materials are rare in nature and the known multiferroic crystals present a weak magnetoelectric coupling which is often well below room temperature. The challenge is thus to find a multiferroic material that would work at room temperature and with a sizeable magnetoelectric coupling. The understanding of the microscopic mechanism of multiferroicity is thus a key ingredient to propose design rules for technologically relevant magnetoelectric materials and atomistic simulations such as first-principles calculations are extremely valuable for this understanding. Based on this, we suggest to study with first-principles techniques and experimental verifications, the effect of uniaxial strains and pressures on multiferroic materials such as $BiFeO_3$. To study the effect of uniaxial strain on $BiFeO_3$ is thus a primer and it will be of high interest for understanding more in details how the electric polarization and the magnetism are linked in such peculiar constraint. Going beyond, the uniaxial constraint on other systems of interests such as $CaMnO_3$ or EuO is also desirable. For $PbTiO_3$, under uniaxial stresses at a critical value of $+2$ GPa and -8 GPa, a structural distortion with a jump of polarization appears. Such behavior may correspond to breaking of Ti–O bonds. This needs to be better analyzed to understand the physics behind it. $Pma2_1$ which has been proposed in case of $PbTiO_3$ and $BiFeO_3$ thin films under tensile strain has not been considered in both $PbTiO_3$ and $SrTiO_3$, so it might be interesting to see whether such group might be possible in case of uniaxial constraints. $Pmc2_1$ phase appeared under large biaxial tension [104] so, it will be also interesting to see whether this phase will appear under compression (beyond the moderate temperature considered here). Clearly more effort from both theory and experiment is required to explore the uniaxial pressure phenomenon.

Chapter 5: Conclusion and Perspectives

References

[1] X. Gonze, J.-M. Beuken, R. Caracas, F. Detraux, M. Fuchs, G.-M. Rignanese, L. Sindic, M. Verstraete, G. Zerah, F. Jollet, M. Torrent, A. Roy, M. Mikami, Ph. Ghosez, J.-Y. Raty, and D. C. Allan, Comput. Mater. Sci. **25**, 478 (2002). 1, 29

[2] K. M. Rabe, M. Dawber, C. Lichtensteiger, C. H. Ahn, and J.-M. Triscone, Top. Appl. Phys. **105**, (2007). 3

[3] J. Valasek (1920), Phys. Rev. **15**: 537 and J. Valasek (1921) , Phys. Rev. **17**, (4): 475. 3

[4] A. Von Hippel, R. G. Breckenridge, F.G. Chesley, and L. Tisza, Ind. Eng. Chem. **38**, 1097 (1946). 3

[5] B. Wul and J. M. Goldman, C.R. Acad. Sci. URSS **51**, 21 (1946). 3

[6] P. Zubko, S. Gariglio, M. Gabay, Ph. Ghosez, and J.-M. Triscone, Annu. Rev. Condensed Matter Phys., **24**, (2011). xv, 4, 6

[7] R. H. Mitchell, Perovskites: Modern and ancient, Almaz Press, Ontario, Canada, (2002). 4

[8] V. M. Goldschmidt. Shrifter Nofke Videnskaps-Akad. Oslo I: mat-Naturv. Kl. No. **2**, 8 (1926). 5

[9] G. Catalan and J. F. Scott, Adv. Mater. **21**, 2463 (2009). 6, 8

[10] M. Guennou, P. Bouvier, G. S. Chen, B. Dkhil, R. Haumont, G. Garbarino, and J. Kreisel, Phys. Rev. B **84**, 174107 (2011). xv, 6, 42

[11] A. M. Glazer, Acta Crystallogr., Sect. B **28**, 3384 (1972). 7, 8, 41

[12] P. M. Woodward, Acta Cryst. B **53**, 44 (1997). 7

[13] G. Shirane and Y. Yamada, Phys. Rev. **177**, 858 (1969). 8, 60

[14] C. J. Howard and H. T. Stokes, Acta Crystallogr., B **54**, 782 (1998). xv, 9

[15] W. Känzig (1957) "Ferroelectrics and Antiferroelectrics", In Frederick Seitz, T. P. Das, D. Turnbull, and E. L. Hahn, Solid State Physics **4**, Academic Press. 10

[16] M. E. Lines and A. M. Glass, Clarendon Press edition, Oxford, (1977). 10, 14

[17] F. Jona and G. Shirane, New York (1993). 10

[18] E. Cockayne and B. P. Burton, Phys. Rev. B **69**, 144116 (2004). 12

[19] R. Resta, Rev. Mod. Phys. **66**, 899 (1994). 13

[20] D. King-Smith and D. Vanderbilt, Phys. Rev. B **47**, 1651(R) (1993). 13, 30

[21] W. Cochran, Adv. Phys. **9**, 387 (1960). 13

[22] P. W. Anderson, Akad. Nauk, Moscow (1960). 13

[23] R. E. Cohen, Nature (London) **358**, 136 (1992). 13, 14, 40

[24] K. M. Rabe, Computer Simulation Studies in Condensed Matter Physics XVI, Springer Proceedings in Physics (Springer, New York 2003). 13

[25] J. F. Scott, Phys. Rev. **183**, 823 (1969). 15

[26] G. Burns and B. A. Scott, Phys. Rev. B **7**, 3088 (1973).

[27] J. F. Scott, Rev. Mod. Phys. **46**, 83 (1974)

[28] P. A. Fleury, J. F. Scott, and J. M. Worlock, Phys. Rev. Lett. **21**, 16 (1968). 15, 60

[29] G. A. Samara, T. Sakudo, and K. Yoshimitsu, Phys. Rev. Lett. **35**, 1767 (1975). 15, 16

[30] P. Bouvier and J. Kreisel, J. Phys.: Condens. Matter **14**, 3981 (2002). 15

[31] R. J. Angel, J. Zhao, and N. L. Ross, Phys. Rev. Lett. **95**, 025503 (2005). 16

[32] J. Zhao, N. L. Ross, and R. J. Angel, Acta Crystallographica Section B **62**, 431 (2006). 16

[33] J. Zhao, N. L. Ross, and R. J. Angel, Acta Crystallographica Section B **60**, 263 (2004).

[34] T. Tohei, A. Kuwabara, T. Yamamoto, F. Oba, and I. Tanaka, Phys. Rev. Lett. **94**, 035502 (2005). 16

[35] U. D. Venkateswaran, V. M. Naik, and R. Naik, Phys. Rev. B **58**, 14256 (1998). 16

[36] A. K. Sood, N. Chandrabhas, D. V. S. Muthu, and A. Jayaraman, Phys. Rev. B **51**, 8892 (1995). 16

[37] D. Gourdain, Ph. Pruzan, J. M. Besson, S. Klotz, J. C. Chervin, B. Canny, W. G. Marshall, J. S. Loveday, and M. Hanfland, Phys. Rev. B **65**, 054104 (2002). 16

[38] P. Pruzan, D. Gourdain, and J. C. Chervin, Phase Transitions **80**, 1103 (2007). 16, 52

[39] J. A. Sanjurjo, E. López-Cruz, and G. Burns, Phys. Rev. B **28**, 7260 (1983). 16

[40] F. Cerdeira, W. B. Holzapfel, and D. Bäuerle, Phys. Rev. B **11**, 1188 (1975). 16

[41] I. A. Kornev, L. Bellaiche, P. Bouvier, P.-E. Janolin, B. Dkhil, and J. Kreisel, Phys. Rev. Lett. **95**, 196804 (2005). 16, 40

[42] E. Bousquet and Ph. Ghosez, Phys. Rev. B **74**, 180101 (2006). 16, 40

[43] Z. Wu and R. E. Cohen, Phys. Rev. Lett. **95** (2005). 16

[44] L. B. Freund and S. Suresh, Cambridge, UK: Cambridge Univ. Press. (2003). 16

[45] J. S. Speck, A. C. Daykin, A. Seifert, A. E. Romanov, and W. Pompe, J. Appl. Phys. (1995).

[46] W. D. Nix and B. M. Clemens, J. Mater. Res. (1999).

[47] T. R. Taylor, P. J. Hansen, B. Acikel, N. Pervez, and R. A. York, Appl. Phys. Lett. (2002). 16

[48] K. J. Choi, M. Biegalski, Y. L. Li, A. Sharan, J. Schubert, R. Uecker, P. Reiche, Y. B. Chen, X. Q. Pan, V. Gopalan, L.-Q. Chen, D. G. Schlom, and C. B. Eom, Science **306** 1005 (2004). 16, 40, 52

[49] J. H. Haeni, P. Irvin, W. Chang, R. Uecker, P. Reiche, Y. L. Li, S. Choudhury, W. Tian, M. E. Hawley, B. Craigo, A. K. Tagantsev, X. Q. Pan, S. K. Streiffer, L. Q. Chen, S. W. Kirchoefer, J. Levy, and D. G. Schlom, Nature **430**, 758-761 (2004). 16, 40, 52, 60

[50] O. Diéguez, K. M. Rabe, and D. Vanderbilt, Phys. Rev. B **72**, 144101 (2005). 16, 40, 41, 60

[51] N. A. Pertsev, A. K. Tagantsev, and N. Setter, Phys. Rev. B **61**, R825 (2000); N. A. Pertsev, A. K. Tagantsev, and N. Setter, Phys. Rev. B **65**, 219901 (E) (2002). 16, 36, 37, 60, 61, 69, 72

[52] Y. Gu, K. Rabe, E. Bousquet, V. Gopalan, and L-Q. Chen, Phys. Rev. B **85**, p. 064117 (2012). 16

[53] C.-J. Eklund, C. J. Fennie, and K. M. Rabe. Phys. Rev. B **79**, (2009). 16

[54] H. Tabata, H. Tanaka, and T. Kawai, Appl. Phys. Lett. **65** 1970 (1994). 16

[55] J. C. Jiang, X. Q. Pan, W. Tian, C. D. Theis, and D. G. Scholm, Appl. Phys. Lett. **74** 2851 (1999). 16

[56] A. Ohtomo and H. Y. Hwang, Nature **427**, 423 (2004). 16, 59

[57] I. V. Stasyuk and I. N. Biletskii, Izvestiya Akademii Nauk Sssr Seriya Fizicheskaya **47** (1983). 17

[58] A. E. Hamed, Phase Transitions, **38** (1992).

[59] M. Koralewski, B. Noheda, G. Lifante, and J. A. Gonzalo, Solid State Commun. **85** (1993). 17

[60] A. Y. Emelyanov, N. A. Pertsev, and A. L. Kholkin, Phys. Rev. B **66**, 214108 (2002). 17

[61] Y. Duan, H. Shi, and L. Qin, J. Phys: Condens. Matter **20** 175210 (2008). 17, 41, 43, 47, 53, 54

[62] N. Argaman and G. Makov, Am. J. Phys. (1999). 20

[63] www.nobelprize.org xvi, 22, 30

[64] P. Hohenberg and W. Kohn, Phys. Rev. **136**, B864 (1964). 21

[65] W. Kohn and L. J. Sham, Phys. Rev. **140**, A1133 (1965). 21, 23, 24

[66] R. M. Martin, (Cambridge University Press, 2004). xvi, 22, 23, 25

[67] D. M. Ceperley and B. J. Alder, Phys. Rev. Lett. **45**, 566 (1980). 26

[68] R. O. Jones and O. Gunnarsson, Rev. Mod. Phys. **61**, 689 (1989). 26

[69] J. P. Perdew, K. Burke, and Y. Wang, Phys. Rev. B **54**, 16533 (1996). 27

[70] Z. Wu and R. E. Cohen, Phys. Rev. B **73**, 235116 (2006). 27

[71] O. Gunnarsson, M. Jonson, and B. I. Lundqvist, Phys. Rev. B **20**, 3136 (1979). 27

[72] D. R. Hamann, M. Schlüter, and C. Chiang. Phys. Rev. Lett. **43**, 1494 (1979). 28

[73] M. Payne, M. Teter, D. Allan, T. Arias, and J. Joannopoulos, Rev. Mod. Phys. **64**, 1045 (1992). xvi, 29

[74] H. J. Monkhorst and J. D. Pack, Phys. Rev. B **13**, 5188 (1976). 29

[75] X. Gonze, G.-M. Rignanese, M. Verstraete, J.-M. Beuken, Y. Pouillon, R. Caracas, F. Jollet, M. Torrent, G. Zerah, M. Mikami, Ph. Ghosez, M. Veithen, V. Olevano, L. Reining, R. Godby, G. Onida, D. Hamann, and D. C. Allan, Zeitschrift fuer Kristallographie **220**, 558 (2005). 29

[76] X. Gonze, B. Amadon, P.-M. Anglade, J.-M. Beuken, F. Bottin, P. Boulanger, F. Bruneval, D. Caliste, R. Caracas, M. Cote, T. Deutsch, L. Genovese, Ph. Ghosez, M. Giantomassi, S. Goedecker, D. R. Hamann, P. Hermet, F. Jollet, G. Jomard, S. Leroux, M. Mancini, S. Mazevet, M. J. T. Oliveira, G. Onida, Y. Pouillon, T. Rangel, G.-M. Rignanese, D. Sangalli, R. Shaltaf, M. Torrent, M. J. Verstraete, G. Zerah, and J. W. Zwanziger, Comput. Phys. Commun. **180**, 2582 (2009). 29

[77] S. Goedecker, M. Teter, and J. Huetter, Phys. Rev. B **54**, 1703 (1996) 30

[78] M. Teter, Phys. Rev. B **48**, 5031 (1993). 30

[79] Z. Wu and R. E. Cohen, Phys. Rev. B **73**, 235116 (2006). 30

[80] A. M. Rappe, K. M. Rabe, E. Kaxiras, and J. D. Joannopoulos, Phys. Rev. B **41**, 1227 (1990). 30

[81] See OPIUM website at http://opium.sourceforge.net/. 30

[82] X. Gonze and C. Lee, Phys. Rev. B **55**, 10355 (1997). 30

[83] L. D. Landau and E. M. Lifshitz, Statistical Physics (Mir, 1968). 31

[84] Q. Y. Qiu, R. Mahjoub, S. P. Alpay, and V. Nagarajan, Acta Materialia **58** 823 (2010). 36, 52

[85] M. E. Lines and A. M. Glass, *Principles and Applications of Ferroelectrics and Related Materials* (Clarendon, Oxford, 1977). 39, 40

[86] Ph. Ghosez, E. Cockayne, U. V. Waghmare, and K. M. Rabe, Phys. Rev. B **60**, 836 (1999). 40, 43

[87] J. C. Wojdel, P. Hermet, M. P. Ljungberg, Ph. Ghosez, and J. Iniguez, J. Phys. Condens. Matter **25**, 305401 (2013). 40

[88] C. Bungaro and K. M. Rabe, Phys. Rev. B **71**, 035420 (2005). 40

[89] K. M. Rabe and Ph. Ghosez, Top. Appl. Phys. **105**, 111 (2007). 40

[90] P.-E. Janolin, P. Bouvier, J. Kreisel, P. A. Thomas, I. A. Kornev, L. Bellaiche, W. Crichton, M. Hanfland, and B. Dkhil, Phys. Rev. Lett. **101**, 237601 (2008). 40, 77

[91] M. Dawber, K. M. Rabe, and J. F. Scott, Rev. Mod. Phys. **77**, 1083 (2005). 40

[92] K. M. Rabe, Curr. Opin. Solid State Mater. Sci. **9**, 122 (2005).

[93] J. Junquera and Ph. Ghosez, J. Comput. Theor. Nanosci. **5**, 2071 (2008). 40

[94] D. G. Schlom, L. Q. Chen, C. B. Eom, K. M. Rabe, S. K. Streiffer, and J. M. Triscone, Annu. Rev. Mater. Res. **37**, 589 (2007). 40

[95] N. A. Pertsev, A. G. Zembilgotov, and A. K. Tagantsev, Phys. Rev. Lett. **80**, (1998). 40, 52

[96] A. Vasudevarao, A. Kumar, L. Tian, J. H. Haeni, Y. L. Li, C.-J. Eklund, Q. X. Jia, R. Uecker, P. Reiche, K. M. Rabe, L. Q. Chen, D. G. Schlom, and V. Gopalan, Phys. Rev. Lett. **97**, 257602 (2006). 40

[97] N. A. Pertsev, A. K. Tagantsev, and N. Setter, Phys. Rev. B **61**, R825 (2000). 40

[98] T. Birol, N. A. Benedek, H. Das, A. Wysocki, A. T. Mulder, B. M. Abbett, E. H. Smith, S. Ghosh, and C. J. Fennie, Curr. Op. in Sol. State Mat. Sci. **16**, 227 (2012). 41

[99] S. Bhattacharjee, E. Bousquet, and Ph. Ghosez, Phys. Rev. Lett. **102**, 117602 (2009). 41

[100] T. Günter, E. Bousquet, A. David, Ph. Boullay, Ph. Ghosez, W. Prellier, and M. Fiebig, Phys. Rev. B **85**, 214120 (2012). 41

[101] E. Bousquet, N. A. Spaldin, and Ph. Ghosez, Phys. Rev. Lett. **104**, 037601 (2010). 41

[102] C. Escorihuela-Sayalero, O. Diéguez, and J. Íñiguez, Phys. Rev. Lett. **109**, 247202 (2012). 41

[103] O. Diéguez, O. E. González-Vázquez, J. C. Wojdel, and J. Íñiguez, Phys. Rev. B **83**, 094105 (2011). 41

[104] Y. Yang, W. Ren, M. Stengel, X. H. Yan, and L. Bellaiche, Phys. Rev. Lett. **109** 057602 (2012). 41, 79

[105] C. J. Fennie and K. M. Rabe, Phys. Rev. Lett. **97**, 267602 (2006). 41

[106] J. H. Lee and K. M. Rabe, Phys. Rev. Lett. **104**, (2010) 207204. 41

[107] J. L. Blok, D. H. A. Blank, G. Rijnders, K. M. Rabe, and D. Vanderbilt, Phys. Rev. B **84**, 205413 (2011). 41

[108] Y. Yang, M. Stengel, W. Ren, X. H. Yan, and L. Bellaiche, Phys. Rev. B **86**, 144114 (2012). 41

[109] E. Bousquet, PhD thesis, Université de Liège, 2008. 41, 49, 62, 63, 77

[110] C. J. Howard and H. T. Stokes, Acta Crystallogr., Sect. B **54**, 782 (1998); **58**, 565 (2002). 41

[111] A. Yu. Emelyanov, N. A. Pertsev, and A. L. Kholkin, Phys. Rev. B **66**, 214108 (2002). 41, 52

[112] Y. Umeno, T. Shimada, T. Kitamura, and Ch. Elsässer, Phys. Rev. B **74**, 174111 (2006). 41, 50, 57

[113] M. Guennou, P. Bouvier, P. Toulemonde, C. Darie, C. Goujon, P. Bordet, M. Hanfland, and J. Kreisel, Phys. Rev. Lett. **112**, 075501 (2014). 42

[114] G. Shirane, H. Danner, and P. Pepinsky, Phys. Rev. **105**, 856 (1957). 43, 56

[115] Relaxations with a polarization developing along the three directions of space have also been performed but relaxed back to FE_x or FE_z phases, except in the vicinity of $\eta_{zz} = 0$, and in that case, they always produce a lower gain in energy than the FE_x or FE_z configurations. 47

[116] The spontaneous polarization was also estimated multiplying the atomic displacements by the Born effective charges of either the reference cubic phase or of the relaxed FE phase at each stress. The Berry phase calculation is much closer to the estimate. xvii, 48

[117] This degeneracy manifests itself in Fig. 3.4 as an horizontal common tangent between FE_x and FE_z curves. 50

[118] M. J. Haun, Z. Q. Zhuang, E. Furman, S. J. Jang, and L. E. Cross, Ferroelectrics 99, 45 (1989). 52

[119] S. Tinte, K. M. Rabe, and D. Vanderbilt, Phys. Rev. B **68**, 144105 (2003). 53

[120] The LGD model predicts a very similar evolution at low temperatures but with a slightly larger amplitude. Since LDA tends to slightly underestimate the polarization, we have made the comparison with LGD theory at 300 K. xviii, 53

[121] D. Fabrègue, M. Coulombier, N. Andrè, J.-P. Raskin, and T. Pardoen, Micro and Nano Letters, Vol. **2**, No. 1, pp. 13-16, March (2007). 54

[122] S. Gravier, M. Coulombier, A. Safi, N. Andrè, J.-P. Raskin, and T. Pardoen, "New on-chip nanomechanical testing laboratory - Applications to aluminum and polysilicon thin films", IEEE J. Microelectromech. Syst., Vol. **18**, No. 3, pp. 555-569, March (2009).

[123] U. K. Bhaskar, T. Pardoen, V. Passi, and J.-P. Raskin, Appl. Phys. Lett. **102**, 031911, (2013). 54

[124] Tetragonal lattice constants of $PbTiO_3$ extrapolated to 0 K are from S. A. Mabud and A. M. Glazer, J. Appl. Cryst. **12**, 49 (1979). Spontaneous polarization is from V. G. Gavrilyachenko, R. I. Spinko, M. A. Martynen, and R. G. Fesenko, Sov. Phys. Solid State **12**, 1203 (1970). 56

[125] K. A. Müller and H. Burkard, Phys. Rev. B **19**, 3593 (1979). 59, 60

[126] J. F. Schooley, W. R. Hosler, and M. L. Cohen, Phys. Rev. Lett. **12**, 474 (1964). 59

[127] M. W. Cole, P. C. Joshi, M. H. Ervin, M. C. Wood, and R. L. Pfeffer, The influence of Mg doping on the materials properties of $Ba_xSr_{1-x}TiO_3$ thin films for tunable device applications. Thin Solid Films 374, 34-41 (2000). 59

[128] H. Ohta, Mat. Today. 10 44-49 (2007). 59

[129] J. Slutsker, I. Levin, J. Li, A. Artemev, and A. L. Roytburd, Phys. Rev. B **73**, 184127 (2006). 59

[130] E. Bousquet, M. Dawber, N. Stucki, C. Lichtensteiger, P. Hermet, S. Gariglio, J.-M. Triscone, and Ph. Ghosez, Nature Vol **452**, (2008).

[131] M. Dawber, C. Lichtensteiger, M. Cantoni, M. Veithen, Ph. Ghosez, K. Johnston, K. M. Rabe, and J.-M. Triscone, Phys. Rev. Lett. **95**, 177601 (2005).

[132] A.-B. Posadas, M. Lippmaa, F. J. Walker, M. Dawber, C. H. Ahn, and J.-M. Triscone, Top. Appl. Phys **105**, 291-304 (2007). 59

[133] M. O'Keeffe, Nature **419**, 28-29 (2002). xviii, 60

[134] H. Thomas and K. A. Müller, Phys. Rev. Lett. **21**, 1256 (1968). 60

[135] W. Zhong and D. Vanderbilt, Phys. Rev. B **53**, (1996). 60

[136] M. P. Warusawithana, C. Cen, Ch. R. Sleasman, J. C. Woicik, Y. Li, L. F. Kourkoutis, J. A. Klug, H. Li, Ph. Ryan, L.-P. Wang, M. Bedzyk, D. A. Muller, L.-Q. Chen, J. Levy, and D. G. Schlom, Science **17** 367 (2009). 60

[137] O. Diéguez and D. Vanderbilt, Cond-mat.mtrl-sci (2008). 60

[138] T. Hashimoto, T. Nishimatsu, H. Mizuseki, Y. Kawazoe, A. Sasaki, and Y. Ikeda, Jpn. J. Appl. Phys, Part 1 **44**, 7134 (2005). 60

[139] A. Antons, J. B. Neaton, K. M. Rabe, and D. Vanderbilt, Phys. Rev. B **71**, 024102 (2005). 60

[140] C.-H. Lin, C.-M. Huang, and G. Y. Guo, J. Appl. Phys. **100**, 084104 (2006). 61

[141] M. Guennou, P. Bouvier, and J. Kreisel, Phys. Rev. B. **81**, 054115 (2010). 61

[142] A. G. Beattie and G. A. Samara, J. Appl. Phys, Vol. **42**, No. 6, May (1971). 61

[143] A. Tröster, W. Schranz, F. Karsai, and P. Blaha, Phys. Rev. X **4**, 031010 (2014). 61

[144] T. S. Chang, J. Appl. Phys, Vol. **43**, No. 8, (1972). 61

[145] Y. Tsujimi, T. Yanagisawa, and T. Mogami, J. Korean Phys. Soc, Vol. **62**, No. 7, (2013). 61

[146] Y. J. Chang, G. Khalsa, L. Moreschini, A. L. Walter, A. Bostwick, K. Horn, A. H. MacDonald, and E. Rotenberg, Phys. Rev. B **87**, 115212 (2013). 61

References

[147] F. W. Lytle, J. Appl. Phys, Vol. **35**, No. 7, (1964). 62, 65

[148] C. LaSota, C.-Z. Wang, R. Yu, and H. Krakauer, Ferroelectrics **194**, 109 (1997). 63

[149] W. Jauch and A. Palmer, Phys. Rev. B **60**, 2961 (1999). 65

References

Appendix A

Theoretical study of $SrTiO_3$ under uniaxial, biaxial and isotropic mechanical strains

Here we report the values of different phases of $SrTiO_3$ under tensile and compressive strains. Table A.1 and Table A.2 are the input for the uniaxial compressive strains and tensile strains of $SrTiO_3$ in LDA volume. Table A.3 and Table A.4 are the input for the uniaxial compressive strains and tensile strains of $SrTiO_3$ in GGA volume.

Appendix A: Theoretical study of $SrTiO_3$ under uniaxial, biaxial and isotropic mechanical strains

Strain	Space group	Glazer's notation	ΔE (meV/f.u.)	R_x	R_y	R_z
-0.5%	I4/*mcm*	$a^0a^0c^-$	-21.96	0	0	6.89
-1%	*Ima*2	$a^-_+a^-_+c^0$	-21.15	4.80	4.80	0
	Fmmm	$a^-b^0c^0$	-23.04	7.08	0	0
	I4/*mcm*	$a^0a^0c^-$	-17.22	0	0	6.50
-2%	*Ima*2	$a^-_+a^-_+c^0$	-15.76	5.1	5.1	0
	Fmmm	$a^-b^0c^0$	-18.91	7.6	0	0
	I4/*mcm*	$a^0a^0c^-$	0.89	0	0	5.80
-2.21%	*Ima*2	$a^-_+a^-_+c^0$	-13.05	5.17	5.17	0
	Fmmm	$a^-b^0c^0$	-16.75	7.71	0	0
	I4/*mcm*	$a^0a^0c^-$	6.42	0	0	5.65
-4%	Ima2	$a^-_+a^-_+c^0$	33.50	5.73	5.73	0
	Fmmm	$a^-b^0c^0$	26.64	8.75	0	0
	I4/*mcm*	$a^0a^0c^-$	79.55	0	0	4.05
-6%	Ima2	$a^-_+a^-_+c^0$	127.81	6.23	6.23	0
	Fmmm	$a^-b^0c^0$	126.66	9.98	0	0
	Cm	$a^-_+b^-_+c^0$	126.03	0.45	9.82	0
	Fmm2	$a^-_+a^0c^0$	126.20	9.91	0	0
	I4/*mcm*	$a^0a^0c^-$	224.48	0	0	0
-7%	Ima2	$a^-_+a^-_+c^0$	191.05	6.49	6.49	0
	Fmmm	$a^-b^0c^0$	201.53	10.67	0	0
	Cm	$a^-_+b^-_+c^0$	190.95	6.50	6.50	0
	Fmm2	$a^-_+a^0c^0$	198.41	10.43	0	0
	I4/*mcm*	$a^0a^0c^-$	331.62	0	0	0

-9.73%	Ima2	$a^-_+a^-_+c^0$	402.64	7.11	7.11	0
	Fmmm	$a^-b^0c^0$	484.31	12.50	0	0
	Cm	$a^-_+b^-_+c^0$	402.44	7.10	7.10	0
	Fmm2	$a^-_+a^0c^0$	455.17	11.41	0	0
	I4/mcm	$a^0a^0c^-$	754.03	0	0	0
-10%	Ima2	$a^-_+a^-_+c^0$	426.37	7.17	7.17	0
	Fmmm	$a^-b^0c^0$	518.53	12.68	0	0
	Cm	$a^-_+b^-_+c^0$	426.17	7.17	7.17	0
	Fmm2	$a^-_+a^0c^0$	493.48	0.000019	0	0
	I4/mcm	$a^0a^0c^-$	807.35	0	0	0

Table A.1: Uniaxial compressive strain, Space group, gain in energy (meV/f.u) and rotational angles (°) for the phases of $SrTiO_3$ at LDA level.

Appendix A: Theoretical study of $SrTiO_3$ under uniaxial, biaxial and isotropic mechanical strains

Strain	Space group	Glazer's notation	ΔE (meV/f.u.)	R_x	R_y	R_z
0%	I4/*mcm*	$a^0a^0c^-$	-23.02	0	0	7.17
+1%	I4/*mcm*	$a^0a^0c^-$	-16.83	0	0	7.77
+1.20%	I4/*mcm*	$a^0a^0c^-$	-15.17	0	0	7.85
+2%	I4/*mcm*	$a^0a^0c^-$	-1.91	0	0	8.28
	*I*4*cm*	$a^0a^0c^-_+$	-2.03	0	0	8.22
+3%	I4/*mcm*	$a^0a^0c^-$	24.38	0	0	8.80
	*I*4*cm*	$a^0a^0c^-_+$	20.99	0	0	8.55
+4%	I4/*mcm*	$a^0a^0c^-$	53.72	0	0	9.21
	*I*4*cm*	$a^0a^0c^-_+$	44.05	0	0	8.80

Table A.2: Uniaxial tensile strain, Space group, gain in energy (meV/f.u) and rotational angles (°) for the phases of $SrTiO_3$ at LDA level.

Appendix A: Theoretical study of $SrTiO_3$ under uniaxial, biaxial and isotropic mechanical strains

Strain	Space group	Glazer's notation	ΔE (meV/f.u.)	R_x	R_y	R_z
0%	$Ima2$	$a^-_+a^-_+c^0$	-8.26	3.77	3.77	0
	$Fmmm$	$a^-b^0c^0$	-8.10	5.57	0	0
	Cm	$a^-_+b^-_+c^0$	-8.44	2.25	4.77	0
	$Fmm2$	$a^-_+a^0c^0$	-8.26	5.51	0	0
	$I4/mcm$	$a^0a^0c^-$	-5.77	0	0	5.10
-0.5%	$Ima2$	$a^-_+a^-_+c^0$	-7.25	3.95	3.95	0
	$Fmmm$	$a^-b^0c^0$	-6.72	5.90	0	0
	Cm	$a^-_+b^-_+c^0$	-7.41	2.07	5.21	0
	$Fmm2$	$a^-_+a^0c^0$	-7.13	5.83	0	0
	$I4/mcm$	$a^0a^0c^-$	-0.79	0	0	4.69
-1%	$Ima2$	$a^-_+a^-_+c^0$	-4.06	4.10	4.10	0
	$Fmmm$	$a^-b^0c^0$	-2.96	6.18	0	0
	Cm	$a^-_+b^-_+c^0$	-3.69	2.09	5.5	0
	$Fmm2$	$a^-_+a^0c^0$	-4.18	6.11	0	0
-2%	$Ima2$	$a^-_+a^-_+c^0$	10.15	4.42	4.42	0
	$Fmmm$	$a^-b^0c^0$	13.78	6.70	0	0
	Cm	$a^-_+b^-_+c^0$	10.07	4.41	4.42	0
	$Fmm2$	$a^-_+a^0c^0$	11.77	6.33	0	0
-3%	$Ima2$	$a^-_+a^-_+c^0$	34.20	4.75	4.75	0
	$Fmmm$	$a^-b^0c^0$	43.09	7.32	0	0
	Cm	$a^-_+b^-_+c^0$	34.17	4.75	4.75	0
	$Fmm2$	$a^-_+a^0c^0$	38.63	7.15	0	0
-4%	Ima2	$a^-_+a^-_+c^0$	65.18	5.05	5.05	0
	Fmmm	$a^-b^0c^0$	82.42	8	0	0

Cm	$a^-_+b^-_+c^0$	65.23	5.06	5.07	0
Fmm2	$a^-_+a^0c^0$	74.22	7.67	0	0

Table A.3: Uniaxial compressive strain, Space group, gain in energy (meV/f.u) and rotational angles (°) for the phases of $SrTiO_3$ at GGA level.

Appendix A: Theoretical study of $SrTiO_3$ under uniaxial, biaxial and isotropic mechanical strains

Strain	Space group	Glazer's notation	ΔE (meV/f.u.)	R_x	R_y	R_z
+0.5%	$Cmcm$	$a^0b^+c^-$	-6.88	0	5.25	0
	$I4cm$	$a^0a^0c^-_+$	-7.96	0	0	5.50
	$I4/mcm$	$a^0a^0c^-$	-7.96	0	0	5.50
+1%	$Cmcm$	$a^0b^+c^-$	-3.23	0	4.91	0
	$I4cm$	$a^0a^0c^-_+$	-8.14	0	0	5.62
	$I4/mcm$	$a^0a^0c^-$	-7.64	0	0	5.82
+2%	$Cmcm$	$a^0b^+c^-$	11.01	0	4.48	0
	$I4cm$	$a^0a^0c^-_+$	-4.26	0	0	5.93
	$I4/mcm$	$a^0a^0c^-$	0.26	0	0	6.30

Table A.4: Uniaxial tensile strain, Space group, gain in energy (meV/f.u) and rotational angles (°) for the phases of $SrTiO_3$ at GGA level.

Appendix A: Theoretical study of $SrTiO_3$ under uniaxial, biaxial and isotropic mechanical strains

Appendix B

List of scientific contributions

Publications in international journals

1. *First-principles study of $PbTiO_3$ under uniaxial strains and stresses.*
   Henu Sharma, Jens Kreisel and Philippe Ghosez
   Published in the Journal of Physics Review B **90**, 214102 (2014)

2. *Theoretical study of $SrTiO_3$ under uniaxial, biaxial and isotropic mechanical strains*
   Henu Sharma, Denis Fontaine, Jens Kreisel and Philippe Ghosez
   In progress

Oral presentations

1. *Computational study of pressure effects on $SrTiO_3$*
   Henu Sharma, Denis Fontaine, Jens Kreisel and Philippe Ghosez
   PhD Day, University of Liège, Belgium, April 2014

2. *Phase diagram of lead titanate under uniaxial strains and stresses*
   Henu Sharma, Jens Kreisel and Philippe Ghosez
   PhD Day, University of Liège, Belgium, March 2013

3. *Phase diagram of lead titanate under uniaxial strain*
   Henu Sharma, Jens Kreisel and Philippe Ghosez
   OxIDes Conference, Santander, Spain, May 2012

4. *Uniaxial strain engineering of ferroelectricity in oxides: Combined experimental and theoretical studies*
   Henu Sharma, Jens Kreisel and Philippe Ghosez
   PhD Day, University of Liège, Belgium, March 2012

5. *Strained induced ferroelectricity in simple binary oxides: Combined theory and experiment*
   Henu Sharma, Jens Kreisel, Pierre Bouvier and Philippe Ghosez
   Sesimbra near Lisbon, Portugal, March 2011

Poster presentations

1. *Uniaxial strain and stress engineering of lead titanate*
   Henu Sharma, Jens Kreisel and Philippe Ghosez
   Fundamental Physics of Ferroelectrics and Related Materials, Ames IA USA, January 2013

2. *Phase diagram of lead titanate under uniaxial strain*
   Henu Sharma, Jens Kreisel and Philippe Ghosez
   IDS-FunMat Third Training School, Annecy, France, March 2013

3. *Phase diagram of lead titanate under uniaxial strain*
   Henu Sharma, Jens Kreisel and Philippe Ghosez
   INPG PhD Day, Grenoble, France, June 2012

4. *Uniaxial strain engineering of ferroelectricity in oxides: Combined experimental and theoretical studies*
   Henu Sharma, Jens Kreisel, Pierre Bouvier and Philippe Ghosez
   IDS-FunMat Second Training School, Anglet, France, March 2012

Research Visits

1. Internship at the PHASIS group, Geneva, Switzerland in September 2012 under the guidance of Dr. Jorge Cors on oxygen sensors.

2. Research visit to the group of Prof. Jens Kreisel at the Centre de Recherche Public Gabriel Lippmann, Luxembourg from December 2013 to May 2014.